Cell

TEX264 drives selective autophagy of DNA lesions to promote DNA repair and cell survival

Graphical abstract

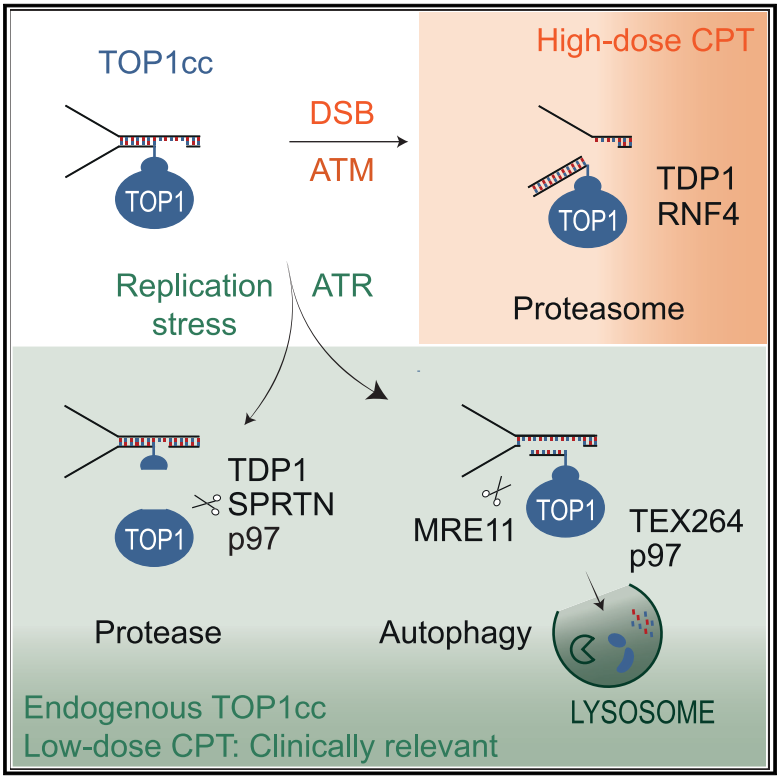

Highlights

- Selective autophagy (nucleophagy) repairs nuclear TOP1cc to maintain genome stability
- TEX264 is the nucleophagy receptor for TOP1cc delivery to the lysosomes
- TEX264-orchestrated nucleophagy is ATR- and MRE11-dependent but proteasome independent
- TEX264-TOP1cc axis is evolutionarily conserved and clinically relevant

Authors

Pauline Lascaux, Gwendoline Hoslett, Sara Tribble, ..., Marta Popović, Ira Milošević, Kristijan Ramadan

Correspondence

kristijan.ramadan@ntu.edu.sg

In brief

TEX264, a conserved and cancer-relevant autophagy receptor, orchestrates selective autophagy of DNA lesions induced by topoisomerase 1 cleavage complexes to ensure genome stability and cell survival.

Lascaux et al., 2024, Cell *187*, 5698–5718
October 3, 2024
https://doi.org/10.1016/j.cell.2024.08.020

CellPress

CellPress
OPEN ACCESS

Cell

Article

TEX264 drives selective autophagy of DNA lesions to promote DNA repair and cell survival

Pauline Lascaux,[1] Gwendoline Hoslett,[1] Sara Tribble,[1] Camilla Trugenberger,[1] Ivan Antičević,[2] Cecile Otten,[2] Ignacio Torrecilla,[1] Stelios Koukouravas,[1] Yichen Zhao,[1] Hongbin Yang,[1] Ftoon Aljarbou,[1] Annamaria Ruggiano,[1] Wei Song,[1] Cristiano Peron,[1] Giulio Deangeli,[3] Enric Domingo,[4] James Bancroft,[5] Loïc Carrique,[6] Errin Johnson,[7] Iolanda Vendrell,[8,9] Roman Fischer,[8,9] Alvin Wei Tian Ng,[10] Joanne Ngeow,[10,11] Vincenzo D'Angiolella,[1,12] Nuno Raimundo,[13,14] Tim Maughan,[15] Marta Popović,[2] Ira Milošević,[5,14] and Kristijan Ramadan[1,10,16,*]

[1]The MRC Weatherall Institute of Molecular Medicine, Department of Oncology, John Radcliffe Hospital, University of Oxford, Oxford OX3 9DS, UK
[2]DNA Damage Group, Laboratory for Molecular Ecotoxicology, Department for Marine and Environmental Research, Institute Ruđer Bošković, 10000 Zagreb, Croatia
[3]Department of Clinical Neurosciences, University of Cambridge, Cambridge CB2 2PY, UK
[4]Department of Oncology, Medical Sciences Division, Old Road Campus Research Building, University of Oxford, Oxford OX3 7DQ, UK
[5]Centre for Human Genetics, Nuffield Department of Medicine (NDM), University of Oxford, Oxford OX3 7BN, UK
[6]Division of Structural Biology, Centre for Human Genetics, Nuffield Department of Medicine (NDM), University of Oxford, Oxford OX3 7BN, UK
[7]Dunn School Bioimaging Facility, Sir William Dunn School of Pathology, University of Oxford, Oxford OX1 3RE, UK
[8]Target Discovery Institute, Nuffield Department of Medicine (NDM), University of Oxford, Oxford OX3 7FZ, UK
[9]Chinese Academy for Medical Sciences Oxford Institute, Nuffield Department of Medicine (NDM), University of Oxford, Oxford OX3 7FZ, UK
[10]Lee Kong Chian School of Medicine (LKCMedicine), Nanyang Technological University, Singapore 636921, Singapore
[11]Cancer Genetics Service, Division of Medical Oncology, National Cancer Centre Singapore, Singapore 169610, Singapore
[12]Edinburgh Cancer Research, CRUK Scotland Centre, Institute of Genetics and Cancer, University of Edinburgh, EH4 2XU Edinburgh, UK
[13]Penn State College of Medicine, Department of Cellular and Molecular Physiology, Hershey, PA 17033, USA
[14]Multidisciplinary Institute for Aging, Center for Innovation in Biomedicine and Biotechnology, University of Coimbra, Coimbra 3000-370, Portugal
[15]Institute of Systems, Molecular and Integrative Biology, University of Liverpool, Liverpool L69 7BE, UK
[16]Lead contact
*Correspondence: kristijan.ramadan@ntu.edu.sg
https://doi.org/10.1016/j.cell.2024.08.020

SUMMARY

DNA repair and autophagy are distinct biological processes vital for cell survival. Although autophagy helps maintain genome stability, there is no evidence of its direct role in the repair of DNA lesions. We discovered that lysosomes process topoisomerase 1 cleavage complexes (TOP1cc) DNA lesions in vertebrates. Selective degradation of TOP1cc by autophagy directs DNA damage repair and cell survival at clinically relevant doses of topoisomerase 1 inhibitors. TOP1cc are exported from the nucleus to lysosomes through a transient alteration of the nuclear envelope and independent of the proteasome. Mechanistically, the autophagy receptor TEX264 acts as a TOP1cc sensor at DNA replication forks, triggering TOP1cc processing by the p97 ATPase and mediating the delivery of TOP1cc to lysosomes in an MRE11-nuclease- and ATR-kinase-dependent manner. We found an evolutionarily conserved role for selective autophagy in DNA repair that enables cell survival, protects genome stability, and is clinically relevant for colorectal cancer patients.

INTRODUCTION

Excessive torsional stress in nuclear DNA must be resolved to ensure unperturbed progression of DNA replication and transcription, genome stability, and cell survival.[1–3] Topoisomerase 1 (TOP1) is crucial for resolving torsional DNA stress.[4,5] TOP1 cleaves one strand of supercoiled DNA structures ahead of DNA replication or transcription to release torsional stress on the DNA, facilitating uninterrupted DNA synthesis and transcription. As part of its enzymatic cycle, TOP1 forms a transient phosphotyrosine covalent link between the 3′-broken DNA ends and a tyrosine in its active DNA-binding domain.[6] This linkage represents a typical 3'-DNA-protein crosslink, a deleterious DNA lesion commonly known as a TOP1 cleavage complex (TOP1cc).[7]

Typically, TOP1cc is transient and reversible. Various types of endogenous DNA damage, such as abasic sites, oxidized nucleotides, ribonucleotides, or alkylated bases, prevent the release of TOP1.[6,8] Stabilized TOP1cc hinders the progression of

replication forks, making this DNA damage a primary endogenous source of genomic instability and cell lethality.[9]

The cytotoxicity of TOP1cc is exploited in cancer therapy by the widely used class of TOP1 poisons such as camptothecin (CPT) and its analogs.[4,10–12] Irinotecan, topotecan, belotecan, and trastuzumab deruxtecan are CPT analogs approved for treating colorectal, small-cell lung, ovarian, and breast cancer. However, the development of resistance to TOP1 poisons, particularly in colorectal cancer patients, poses a significant clinical challenge.[13,14] Thus, understanding the molecular mechanisms of TOP1cc repair is essential for understanding genome stability and critical for improving clinical outcomes and stratification for patients treated with TOP1 poisons.

TOP1cc repair involves restoration of DNA integrity and clearance of damaged TOP1. DNA repair mainly relies on either tyrosyl DNA phosphodiesterase 1 (TDP1) excision or nucleases such as MRE11.[1,4] The TDP1 pathway relies on hydrolysis of the phosphotyrosine bond that covalently links TOP1 to the 3′ end of a single-stranded DNA break.[15–18] The remaining 3′ phosphoryl-nicked DNA is repaired by base excision repair (BER).[19] Alternatively, nucleases such as MRE11 cleave and resect DNA in a 3′ to 5′ direction on one strand.[18,20]

Efficient TOP1cc repair tightly correlates with the upstream degradation of the proteinaceous part of TOP1cc, making the enzyme-DNA bond accessible for repair machinery. Early studies indicate that the proteasome degrades TOP1 covalently attached to DNA.[21–25] However, this process is predominantly described with doses above a certain threshold, corresponding to micromolar (μM) CPT doses. Because these are unachievable in clinical settings,[26–28] the physiological relevance of this model is called into question. Recently, the debulking of TOP1cc at clinically relevant doses of CPT (low-dose CPT, nanomolar [nM]) has been shown to depend on TOP1 unfolding by the ATPase p97, and its cofactor TEX264.[29] The p97-TEX264 complex cooperates with the metalloprotease SPRTN to fragment TOP1 before TDP1-mediated repair.[30–32] Strikingly, TEX264 has also recently been identified as a main receptor for autophagy.[33,34]

Autophagy ensures the maintenance of cellular homeostasis by degrading redundant, damaged, misfolded, or aggregated proteins and organelles in lysosomes.[35–38] Lysosomes are highly acidic vesicles, rich in proteases, hydrolases, nucleases, and lipases, ensuring the fragmentation of their contents into single amino acids, nucleotides, carbohydrates, and lipid structures.[39,40] Selective removal of organelles or substrates by autophagy is achieved through the action of receptors, commonly characterized by an ATG8/LC3 (LC3)-interacting region (LIR).[41,42] LC3 links the receptors to the growing autophagic membranes to sequester substrates. The E1-like activating enzyme ATG7 governs selective autophagy by mediating the lipidation of LC3, which is essential for anchoring to the autophagic membranes.[43] Under starvation, TEX264 is responsible for 50% of autophagy-dependent endoplasmic reticulum turnover (ER-phagy).[33,34] Specifically, TEX264 is a single transmembrane protein embedded in the ER and nuclear envelope.[29,33,34] It has a LIR domain and mediates the remodeling and processing of the ER through autophagy in response to starvation.[44,45]

Loss of autophagy impairs DNA damage repair and increases cell death in response to genotoxic stress,[46–50] highlighting its importance in maintaining genomic stability. It has been shown that autophagy maintains cellular energy levels, provides nucleotides, and controls the level of DNA repair proteins required for accurate DNA replication and repair.[51,52] In yeast, direct clearance of nuclear content by autophagy promotes cell survival under stress conditions.[48,53–55] In mammals, the degradation of nuclear material such as nuclear lamina and RNA-DNA hybrids has recently been described.[56–59] In response to oncogenic stress, Lamin B1 binds to LC3 and is delivered from the nucleus to lysosomes. The process of lysosomal degradation of nuclear Lamin B1 induces cell senescence.[56,57] Further, the survival of mammalian cells suffering from laminopathies depends on the clearance of aberrant cytosolic DNA by autophagy.[60] Moreover, defects in the lysosomal nucleases lead to improper clearance of nuclear DNA found in the cytoplasm and, thus, to numerous human diseases.[61] Therefore, mammalian cells rely on autophagy to clear cytosolic DNA fragments under various chronic stress conditions. However, whether autophagy directly processes nuclear DNA lesions and how this process is orchestrated is unknown. So far, no evidence exists that selective autophagy directly processes DNA lesions to regulate DNA repair for genome stability and cell survival.

Given that TEX264 is involved in two separate cellular processes, DNA damage repair[29] and ER-phagy,[33,34] in the nucleus and in the ER, respectively,[62] we investigated whether TEX264 orchestrates TOP1cc repair via autophagy. We employed biochemical and cell biological methods coupled with mass spectrometry, next-generation DNA sequencing (NGS), live imaging, and electron microscopy to investigate the role of autophagy in TOP1cc repair in human cells. We used zebrafish and colorectal cancer patient data to examine the relevance of selective autophagy of DNA lesions at the organismal level and in response to chemotherapy. Our data demonstrate TEX264-orchestrated selective autophagy of nuclear TOP1cc DNA lesions in vertebrates.

RESULTS

Crosstalk between autophagy and DNA replication in response to CPT treatment

Based on the recently discovered separate roles of TEX264 in ER-phagy and TOP1cc repair,[29,33,34] we hypothesized that TEX264 might be an autophagy receptor that directly processes DNA lesions induced by stabilization of TOP1 covalently bound to nuclear DNA. Immunoprecipitation of TEX264-WT-V5 demonstrated that TEX264 forms a complex with DNA replication, such as the proliferating cell nuclear antigen (PCNA), and autophagy proteins in unsynchronized and S-phase-synchronized cells (Figure 1A). Similar results were obtained by co-immunoprecipitating endogenous TEX264. Interestingly, ATG7 regulated the interaction of endogenous TEX264 with TOP1, the autophagy protein LC3, and the DNA replication component MCM7 (Figure S1A). These results confirmed that TEX264 is indeed involved in autophagy and DNA replication.

To investigate whether other autophagy factors are present at/around the replication fork, we mined available mass spectrometry data from proteomes surrounding nascent DNA (DNA replication forks) in response to various doses of replication-stress-inducing agents: CPT, hydroxyurea (HU), or UV.[63–66] The data were

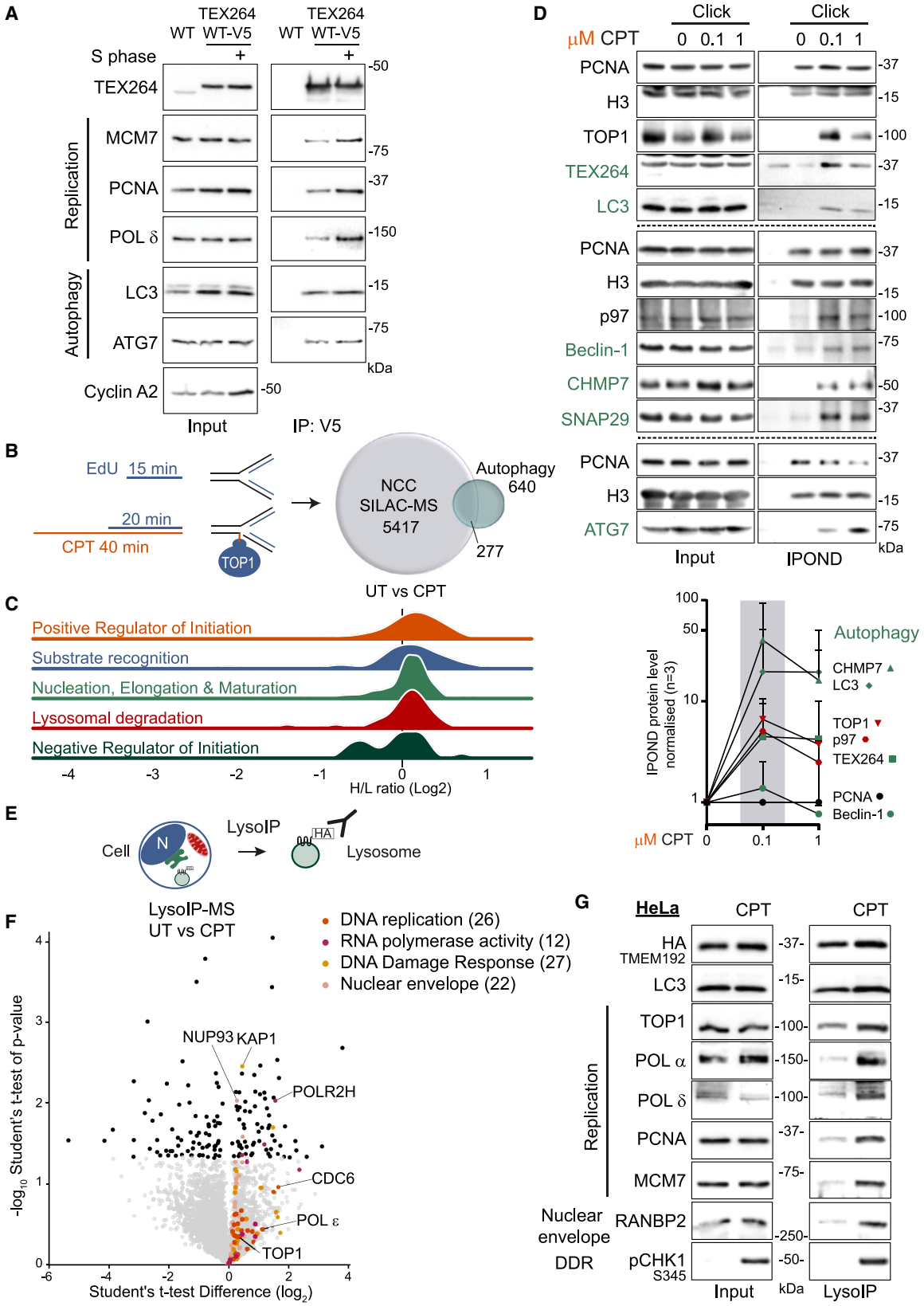

(legend on next page)

collected from 5 independent studies and analyzed for 640 characterized autophagy factors (Figures 1B and S1B; Table S1). Interestingly, autophagy factors represented around 5% of all identified proteins on or around DNA replication sites. Proteins involved in every stage of the autophagy pathway were found at/around sites of DNA replication forks (Figure 1C). Upon CPT treatment, key autophagy proteins were significantly enriched, including factors regulating the initiation of autophagy, such as USP13, a regulator of Beclin-1; receptors, including TEX264; and proteins involved in vesicle maturation, such as CHMP7 and SNAP29. Also, several resident proteins of lysosomes were enriched at the replication fork, including 10 V-ATPases, 8 chaperones, the cathepsin D protease, and RAB39A (Table S1). For validation, we performed isolation of proteins on nascent DNA (iPOND) at both low-dose and high-dose CPT (Figure 1D). Autophagy proteins, such as Beclin-1, TEX264, CHMP7, ATG7, SNAP29, and LC3, were enriched at/around DNA replication forks after CPT treatment. Clinically relevant doses of CPT (low-dose CPT, nM)[26–28] induce a higher level of recruitment to stalled replication forks than high-dose CPT (μM). We concluded that autophagy proteins are actively recruited at/around sites of DNA replication forks and enriched in response to TOP1cc stabilization.

To further support our observations, we created stable HeLa, HCT116, and hTERT RPE-1 cell lines expressing the tagged lysosomal resident protein TMEM192-hemagglutinin (HA) to isolate intact lysosomes by immunoprecipitation (IP), a method known as LysoIP (Figure 1E).[67] The isolated lysosomes were clean from contamination by other organelles, and immunofluorescence staining showed proper colocalization of the tagged lysosomal resident protein TMEM192-HA and late endosome marker LAMP1[68] (Figures S1C and S1D). The content of the intact lysosomes was isolated by LysoIP in HeLa and analyzed by quantitative label-free mass spectrometry. Consistent with previous results,[67] resident proteins of lysosomes, such as numerous cathepsins, V-ATPases, and hydrolyzes, were isolated. Interestingly, CPT treatment induced the lysosomal uptake of many DNA replication and nuclear proteins, such as DNA polymerases, MCM complex proteins, and nuclear pore components (Figure 1F; Table S2). Validation by immunoblotting in S-phase-synchronized cells confirmed the lysosomal uptake of core DNA replication proteins in response to CPT treatment (Figure 1G). TOP1 was also a substrate of lysosomes in HCT116 and hTERT RPE-1 upon low-dose CPT treatment (Figures S1E and S1F). Other TOP1 inhibitors, such as irinotecan and its active metabolite SN-38, induced TOP1 lysosomal uptake (Figure S1G). Altogether, we conclude that crosstalk between autophagy and DNA replication is enhanced as a response to the stabilization of cytotoxic TOP1cc.

Autophagy repairs TOP1cc and promotes cell survival to camptothecin

To assess whether autophagy has a functional role in the processing of TOP1cc, we analyzed TOP1cc level recovery after CPT treatment with a specific TOP1cc antibody (Figures 2A, S2A, and S2B).[69,70] Repair of TOP1cc foci was significantly faster in cells treated with the mTOR inhibitor Torin, a well-known booster of autophagy.[71] In contrast, the inactivation of autophagy by inducible depletion of ATG7, an essential protein for selective autophagy,[43] completely blocked the repair of TOP1cc foci. Autophagy impairment by ATG7 inactivation showed a similar effect on TOP1cc levels when assessed by RADAR assay, a specialized method to isolate proteins covalently bound to DNA[70,72] (Figures 2B and S2C). Interestingly, ATG7 inactivation strongly prevented TOP1 uptake in lysosomes by LysoIP (Figure 2C), suggesting that TOP1cc repair is mediated by selective autophagy.

To further confirm the role of autophagy in TOP1cc repair, we inactivated two other selective autophagy factors in HeLa cells: syntaxin 17 (STX17) and RB1CC1 (also known as FIP200). Syntaxin 17 is a SNARE protein involved in the fusion of mature autophagosomes to lysosomes,[73] and RB1CC1 is a member of the ULK complex and the master regulator of autophagy initiation.[74] As expected, depletion of syntaxin 17 caused the accumulation of autophagosome double-membrane vesicles (Figure S2D). RB1CC1 and syntaxin 17 depletion abolished TOP1 uptake in lysosomes (Figure S2E). Syntaxin 17 inactivation completely prevented TOP1cc repair after CPT treatment (Figure S2F). Strikingly, both ATG7 and syntaxin 17 knockdown strongly impaired cell survival in response to CPT treatment (Figure 2D). Correspondingly, inhibition of lysosomal acidification and function by bafilomycin A1 (BAF) caused increased sensitivity to CPT. However, boosting autophagy by Torin enhanced HeLa cell survival to CPT treatment (Figure S2G). These data suggest that autophagy positively regulates TOP1cc repair and cellular survival to CPT.

To further demonstrate that TOP1 translocates to lysosomes as a response to CPT treatment, we modified a well-established mCherry-GFP autophagy reporter assay to follow TOP1.[75] The mCherry-TOP1-GFP reporter can be detected in red and green channels, except when transported inside the highly acidic lysosomes, where GFP fluorescence is quenched while mCherry remains unaffected (Figure 2E). As expected, untreated cells

Figure 1. Crosstalk between autophagy and DNA replication upon replication fork stalling by CPT

(A) Co-immunoprecipitation of TEX264-WT-V5 in HeLa TEX264^{KO} background in asynchronized or S-phase-synchronized cells (n = 3).

(B) Strategy for replisome proteomics analysis. Venn diagram of the replisome found by nascent chromatin capture (NCC) coupled to stable isotope labeling by amino acids in cell culture (SILAC) and mass spectrometry (MS) analysis, NCC-SILAC-MS[63] overlapped with all known autophagy factors.

(C) Ridge regression plot of known autophagy factors at replication fork identified by SILAC-NCC-MS.[63]

(D) iPOND performed after 40 min of 100 nM CPT (0.1 μM) or 1 μM CPT. Representative blots from different biological repeats and quantification (n = 3). Error bar, SD.

(E) Strategy for purification of intact lysosomes; LysoIP.

(F) Proteome profiling of lysosomes purified by LysoIP after 6 h of 50 nM CPT. Proteins differentially expressed ($-10\log p > 1.301$) shown with full dark circles.

(G) LysoIP performed in S-phase-synchronized HeLa after 6 h of 50 nM CPT.

See also Figure S1 and Tables S1 and S2.

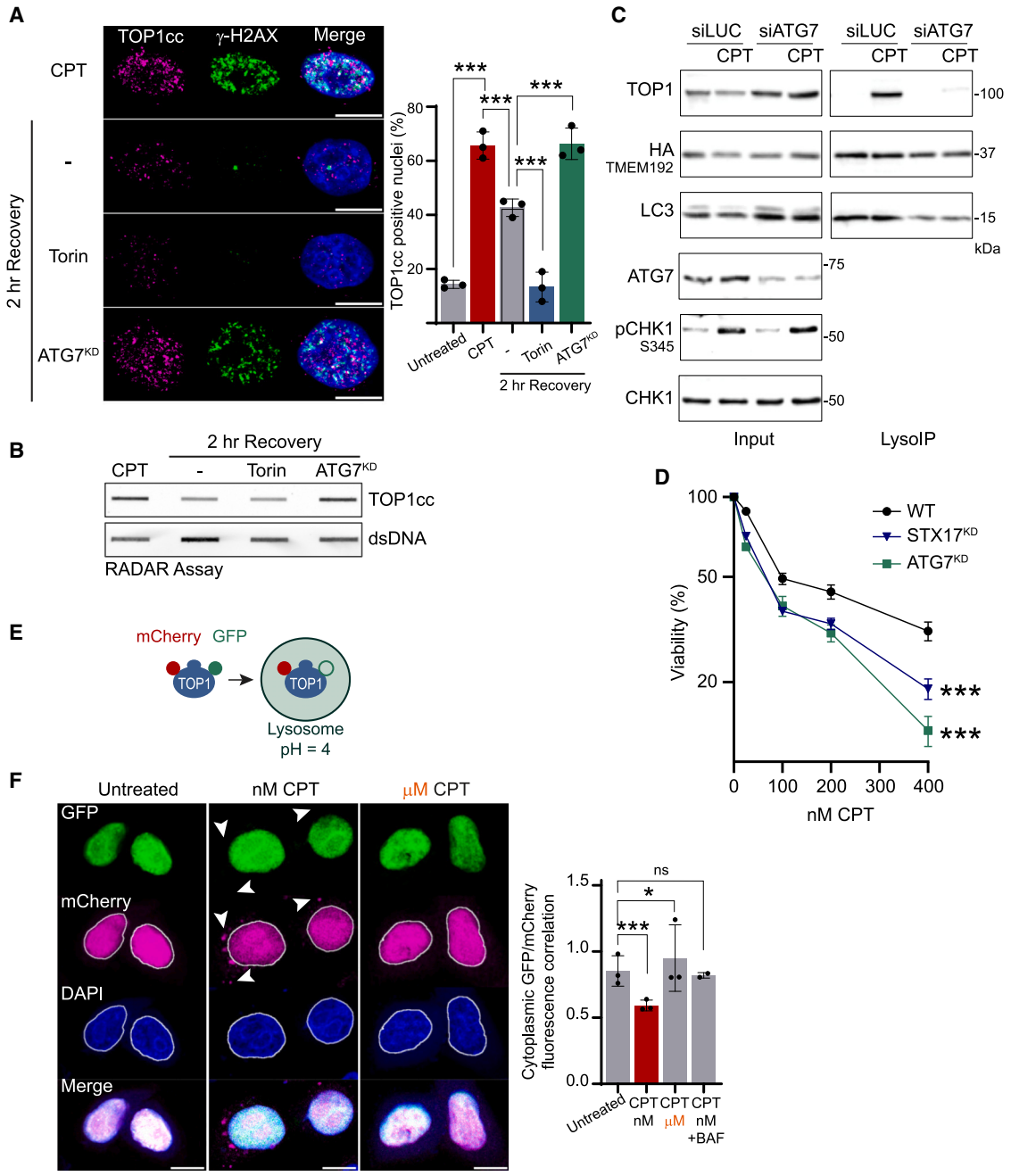

Figure 2. Autophagy repairs TOP1cc to promote cell survival to CPT

(A) Immunofluorescence after 2 h of 50 nM CPT. Torin, 250 nM Torin-1. Quantification of positive nuclei for TOP1cc foci ($n = 3$). Two-way ANOVA. Error bar, SD.

(B) RADAR assay after 2 h of 50 nM CPT ($n = 2$). Torin, 250 nM Torin-1. Double-stranded (ds) DNA; loading control.

(C) LysoIP performed after 6 h of 50 nM CPT ($n = 3$).

(D) Cell viability after 48 h of CPT ($n = 4$). Error bar, SEM.

(E) Strategy used to follow TOP1 delivery to lysosomes. The reporter mCherry-TOP1-GFP presents red and green fluorescence except if internalized in lysosomes (pH = 4).

(F) Imaging of mCherry-TOP1-GFP after 3 h of 50 nM CPT (nM) or 1 μM CPT (μM) ($n = 3$). Bafilomycin A1 (BAF), negative control. Quantification of the correlation between GFP and mCherry fluorescence in the cytoplasm. Two-way ANOVA. Error bar, SD.

Scale bar, 10 μm. $^{*}p < 0.05$; $^{***}p < 0.0005$; ns, not significant.

See also Figure S2.

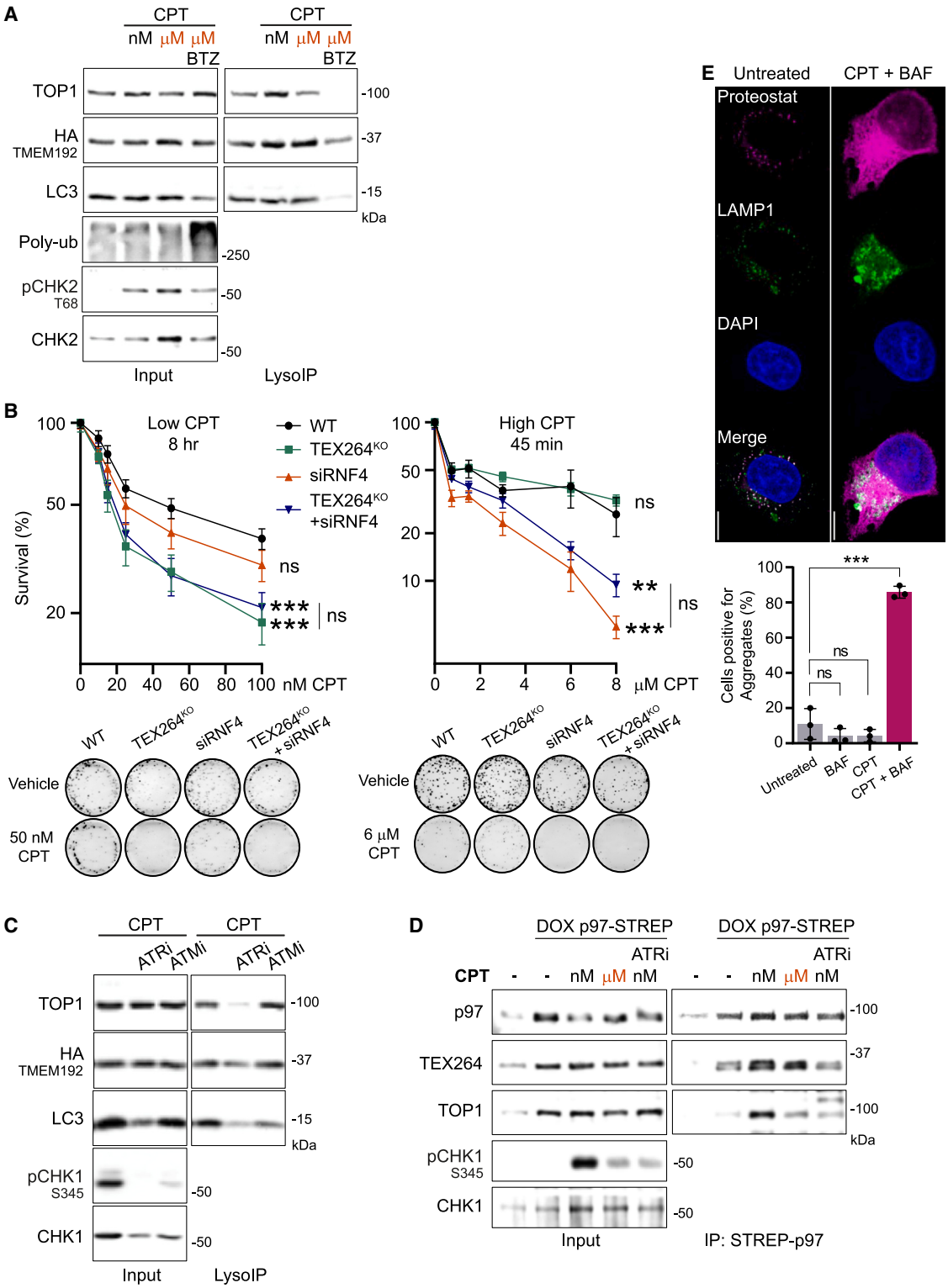

Figure 3. Autophagy promotes cell survival independently of the proteasome activity

(A) LysoIP performed after 3 h of 50 nM CPT (nM) or 1 µM CPT (µM) and the proteasome inhibitor bortezomib (BTZ) (n = 3).

(B) Clonogenic assays performed simultaneously with low- or high-dose CPT (n = 3). Error bar, SEM.

(legend continued on next page)

exhibit a robust nuclear signal for both colors and a limited cytoplasmic signal, consistent with the expression and localization of TOP1 in the nucleus (Figure 2F). Notably, the tagged TOP1 enzyme conserved its original DNA-binding activity, as CPT can stabilize mCherry-TOP1-GFP on DNA as it would for the endogenous TOP1 enzyme (Figure S2H). Upon treatment with low-dose CPT, but not high-dose CPT, we observed cytoplasmic red-only puncta, quantified by a decrease in the cytoplasmic GFP/mCherry colocalization ratio (Figure 2F). Inhibiting lysosomal acidification with bafilomycin A1 prevented GFP quenching and restored the GFP/mCherry colocalization ratio, demonstrating the specificity of this assay toward detecting proteins inside lysosomes. Similarly, inactivating either ATG7 or syntaxin 17 abolished the mCherry-TOP1-GFP translocation inside lysosomes in response to CPT treatment (Figure S2I), further suggesting that the autophagy pathway regulates TOP1cc repair and TOP1cc uptake into lysosomes.

Autophagy processes TOP1 during DNA replication stress

TOP1 processing by lysosomes is intriguing, as TOP1cc degradation by the proteasome has been extensively described. However, this process is predominantly described with μM doses of CPT.[21–25] Notably, treatment with high-dose CPT did not induce translocation of the mCherry-TOP1-GFP reporter to lysosomes (Figure 2F), nor did we observe increased lysosomal uptake of endogenous TOP1 assessed by LysoIP (Figure 3A). This shows that TOP1 is a substrate of lysosomes in response to clinically relevant doses of CPT only (low-dose CPT, nM).

To investigate the co-dependency between autophagy and the proteasome in TOP1cc repair, we used low-dose (nM) or high-dose (μM) CPT and monitored cell response. First, we tested the lysosomal uptake of TOP1. As expected, low-dose CPT stimulated TOP1 delivery to lysosomes (Figure 3A). However, this stimulation was not observed with high-dose CPT, even when the proteasome was blocked with bortezomib.

Second, we monitored cell survival in response to low- and high-dose CPT in cells inactivated for TEX264 or RNF4, independently or simultaneously. TEX264 inactivation is a specific way to prevent TOP1 processing by autophagy (see Figure 6). As RNF4 was reported to be essential for TOP1cc proteasomal degradation at high-dose CPT,[25,76,77] we used RNF4 inactivation as a specific way to inhibit TOP1cc processing by the proteasome. Also, we monitored TOP1 lysosomal uptake in response to low-dose CPT, and RNF4 inactivation did not severely impact it (Figure S6E). TEX264 inactivation specifically hypersensitized cells to low-dose CPT, whereas only RNF4-inactivation hypersensitized to high-dose CPT (Figures 3B and S3A). The co-inactivation of both factors did not further increase sensitivity, confirming the independence of the two degradation pathways.

Finally, we monitored the degradation of TOP1 in total cell extract (Figure S3B). Cells were treated with bafilomycin A1 or MG132 to inhibit lysosome function or the proteasome, respectively. Both low- and high-dose CPT induced TOP1 degradation. Still, only autophagy inhibition could rescue TOP1 levels in total cell extract upon low-dose CPT treatment. In contrast, only proteasome inhibition rescued the TOP1 level after high-dose CPT treatment. In conclusion, although autophagy and the proteasome can degrade TOP1cc, there is no co-dependency between the pathways.

Previous research analysis showed that μM and nM doses of CPT induce different types of secondary DNA damage.[28] Low-dose CPT induces DNA replication stress, as evidenced by the slow progression of DNA replication forks and activation of γ-H2AX, which do not localize with 53BP1 foci, a marker of DNA double-strand breaks (DSBs).[78] In contrast, high-dose CPT leads to a nearly complete arrest of DNA replication forks and the formation of DSBs. Monitoring the effect of low- and high-dose CPT on DNA damage by immunofluorescence, we observed that low-dose CPT only induced activation of γ-H2AX but not 53BP1 foci, in contrast to high-dose CPT that induced focal activation of both γ-H2AX and 53BP1 (Figure S3C). Based on these results, we hypothesized that DNA replication stress signaling could trigger TOP1cc processing by autophagy. Indeed, inhibition of ATR, the central kinase involved in the signaling of replication stress,[79,80] strongly abolished the delivery of TOP1cc to lysosomes (Figure 3C). In contrast, inhibition of ATM, the central kinase involved in DSB repair,[79,80] did not impact TOP1cc delivery to lysosomes. Moreover, ATR inhibition prevents the increased binding of p97 to TOP1 in response to low-dose CPT (Figure 3D), which happens through the p97 cofactor TEX264.[29]

We concluded that DNA replication stress, induced by low-dose CPT, drives TOP1 processing by autophagy. This pathway is uncoupled from the known RNF4-dependent proteasomal TOP1cc degradation pathway in response to DSB formation induced by high-dose CPT.

Low-dose CPT induces the formation of protein aggregates

Selective autophagy was first described as a pathway for clearing protein aggregates in cells.[81] To investigate the role of lysosomal degradation of TOP1 under replication stress, we monitored the formation of protein aggregates after low-dose CPT. In brief, the Proteostat dye becomes fluorescent upon binding to the amyloid-type β-sheet tertiary structure of protein aggregates.[82] Inhibition of autophagy combined with low-dose CPT treatment elicited a drastic accumulation of protein aggregates, mainly colocalizing with lysosomes and late endosome marker LAMP1 (Figure 3E).[68] Biochemical purification of protein aggregates using detergents confirmed the formation of TOP1 aggregates at low-dose CPT when lysosome function was

(C) LysoIP in S-phase HeLa cells after 3 h of 50 nM CPT and 1 μM ATR inhibitor VE-822 (ATRi) or 1 μM ATM inhibitor KU-55933 (ATMi) ($n = 3$).
(D) Co-immunoprecipitation of p97-Strep in S-phase HEK293T cells after 1 h of 50 nM CPT (nM) or 1 μM CPT (μM) or 1 μM ATR inhibitor VE-822 (ATRi) ($n = 2$).
(E) Immunofluorescence of protein aggregates using the Proteostat dye after 24 h of 50 nM CPT and quantification ($n = 3$).
Scale bar, 10 μm. Error bar, SD. Two-way ANOVA.
$^{**}p < 0.005$; $^{***}p < 0.0005$; ns, not significant.
See also Figure S3.

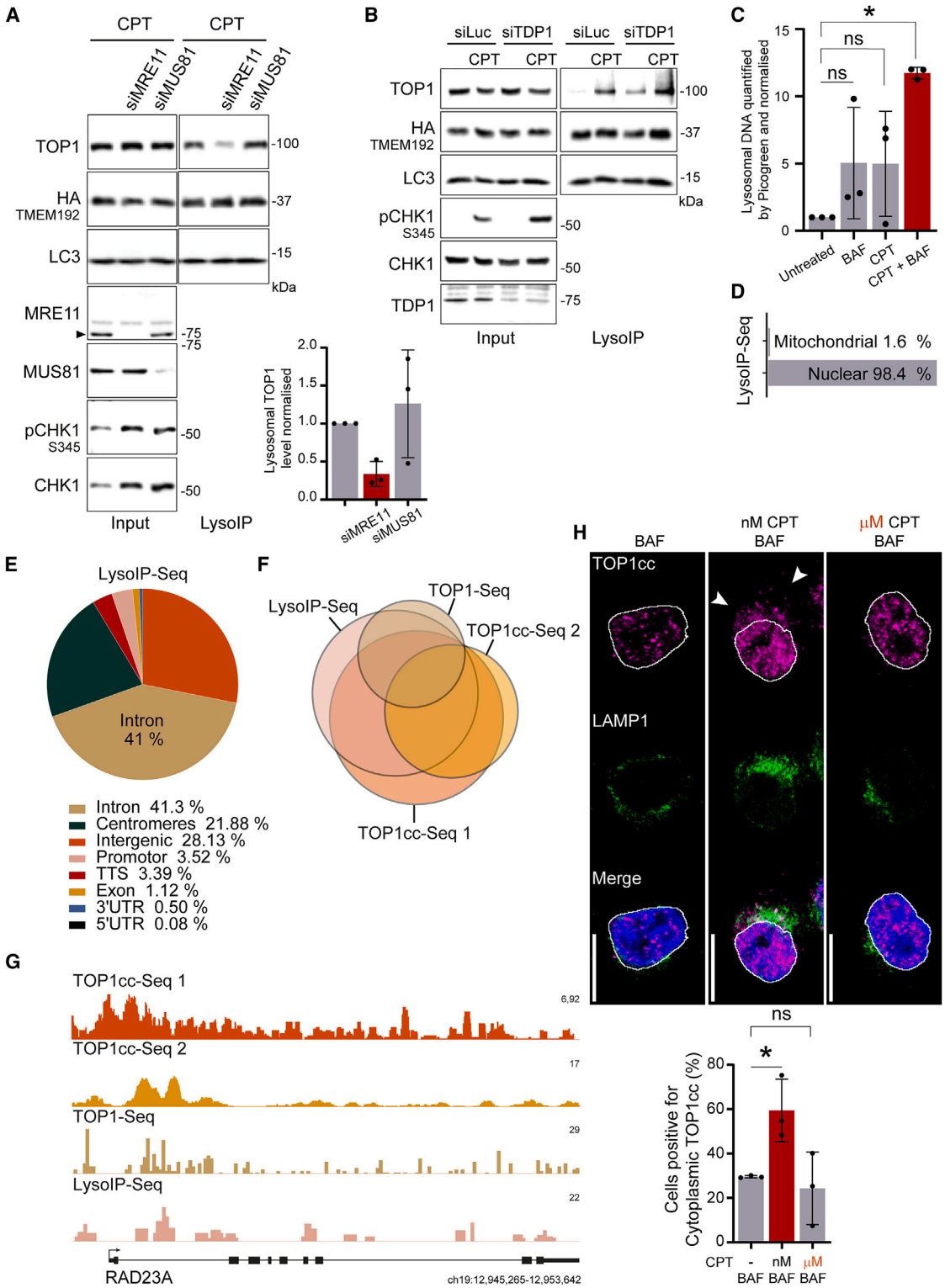

Figure 4. TOP1cc (TOP1 and its bound DNA fragment) are processed by lysosomes

(A) LysoIP performed after 5 h of 50 nM CPT, and quantification graph (n = 3). Error bar, SD.

(B) LysoIP performed after 5 h of 50 nM CPT (n = 3).

(C) Quantification of DNA by Picogreen assay to detect DNA purified by LysoIP after 6 h of treatment (n = 3). Two-way ANOVA. Error bar, SD. Around 450 ng of DNA fragments of less than 1 kb were purified from 20 million cells by LysoIP after treatment with 50 nM CPT and 50 nM BAF.

(legend continued on next page)

inhibited by bafilomycin A1 (Figure S3D). In contrast, high-dose CPT did not induce the formation of TOP1 aggregates. This observation further supports our earlier finding that TOP1 degradation in response to high-dose CPT, where DSBs are formed, is independent of lysosomes. These results show that TOP1cc repair at low-dose CPT depends on autophagy to prevent proteotoxic stress caused by aggregate formation.

Lysosomes directly process TOP1cc DNA lesions

At a nM dose of CPT, full-length TOP1 becomes a direct substrate for autophagy, as shown by the mCherry-TOP1-GFP reporter assay (Figure 2F) and LysoIP assays (Figures 1G, 2C, 3A, and 3C). Focusing on low-dose CPT, we hypothesized that lysosomes process the entire DNA lesion, including TOP1 and its associated DNA fragment. If so, TOP1cc should undergo cleavage by DNA nucleases to allow its export to lysosomes.

We investigated the role of known nucleases and phosphodiesterase in TOP1cc processing, including MRE11,[18,20] MUS81,[83–85] and TDP1.[4,17] Interestingly, neither depletion of MUS81, which promotes DSB formation during the repair of DNA replication fork collapse,[86] nor TDP1, which cleaves remnant TOP1cc peptide after upstream proteolysis, prevented TOP1cc delivery to lysosomes (Figures 4A and 4B). On the contrary, the inactivation of MRE11 nuclease strongly abolished the delivery of TOP1cc to lysosomes (Figure 4A).

To directly assess whether lysosomes process DNA fragments associated with TOP1cc lesions, we quantified and characterized DNA purified from intact lysosomes. DNA fragments of less than 500 bp were observed in lysosomes after combined treatment with CPT and bafilomycin A1 (Figures 4C, S4A, and S4B). This suggests that the complete DNA lesion, TOP1 and its associated DNA fragment, is transported to lysosomes for degradation.

NGS showed that over 98% of DNA fragments isolated from intact lysosomes were of nuclear origin (Figure 4D). TOP1 does not have a consensus binding region on DNA and is found at supercoiled regions ahead of active transcription sites, such as introns[87,88] or replicative centromeric regions.[28,89] Strikingly, the sequence analysis of isolated lysosomal DNA fragments represented mainly intronic and centromeric regions (Figure 4E). To investigate whether the DNA fragments isolated from lysosomes are likely to be covalently linked to TOP1, we overlapped three published TOP1 chromatin immunoprecipitation sequencing (ChIP-seq) results[87,88] with our LysoIP-seq data. The sequenced DNA fragments isolated from lysosomes overlapped 88.6% with the three known TOP1/TOP1cc ChIP-seq datasets (Figures 4F, 4G, and S4C). The overlap between the three independent TOP1 ChIP-seq datasets was similar (around 85%). These data prove that nuclear DNA regions covalently bound to TOP1 are translocated to lysosomes in response to low-dose CPT.

Immunofluorescence using the specific monoclonal antibody against TOP1cc, but not TOP1 alone,[69,70] confirmed the presence of TOP1cc in the cytoplasm in response to low-dose CPT but not to high-dose CPT (Figures 4H and S4D). Altogether, we conclude that lysosomes actively process entire TOP1cc lesions, including their proteinaceous part and the associated DNA fragments.

Lysosomal degradation of TOP1cc occurs in interphase cells

As low-dose CPT induces the direct recruitment of autophagy proteins at sites of stressed DNA replication forks (Figures 1B–1D) and the lysosomal uptake of replication proteins (Figures 1F and 1G), we hypothesized that TOP1cc repair by autophagy occurs during S-phase. To test this hypothesis, cells were synchronized in the G1/S-phase using a thymidine block released and treated with low-dose CPT for 6 h to stabilize TOP1cc during S-phase. Indeed, TOP1 uptake in lysosomes was increased in S-phase (Figure 5A).

To investigate whether TOP1 can exit the nucleus during interphase, we followed the mCherry-TOP1-GFP reporter in live cells stained with LysoView, a pH-sensitive dye specific for lysosomes (Figure 5B; Videos S1 and S2). Within 30 min of CPT treatment, a mCherry/GFP-positive protrusion emerged from the nucleus, eventually forming a new mCherry/GFP vesicle fused with lysosomes and turned mostly red due to GFP quenching. Finally, the red-only vesicle disappeared as the digestion process was completed. This live imaging, together with the quantification of the red-only cytoplasmic puncta in fixed cells (Figures 2F and S2I), demonstrated that TOP1cc degradation through autophagy occurs during interphase when the nuclear envelope is intact.

To investigate the state of the nuclear envelope during interphase in response to CPT, we monitored the lamina structure following the GFP-tagged Lamin A/C by live-cell imaging (Figure 5C; Video S3). Nuclear envelope rupturing during interphase (NERDI) is a transient loss of permeability in the barrier, documented in several cancer cell lines under severe stress conditions.[90,91] NERDI is associated with the tendency to form nuclear envelope protrusions that can lack a lamina structure.[92,93] Strikingly, the lamina undergoes transient and localized reshaping within 30 min of CPT exposure. Cell rendering reveals a thinner lamina structure, primarily observed at contact sites with lysosomes. This suggests that transient and restricted rupture of the nuclear envelope occurs in response to low-dose CPT.

We used transmission volume electron microscopy to visualize the nuclear envelope after treatment with CPT (Figures 5D and S5A; Video S4). The distance between the inner nuclear membrane (INM) and the outer nuclear membrane (ONM) under physiological conditions is about 50 nm,[94] as reproduced in our control

(D) Distribution of the LysoIP-purified DNA, mapped reads sequenced by NGS.
(E) Genomic distribution of the LysoIP-purified mapped reads sequenced by NGS.
(F) Proportional Eulerr representation of the overlap among the different ChIP-seq of TOP1cc, TOP1cc-seq 1 (MCF7—GEO: GSE135808),[87] TOP1cc-seq 2 (LNCAP—GEO: GSE135808),[87] and TOP1-seq (HCT116—GEO: GSE57628).[88] All conditions were treated with CPT.
(G) Genomic browser alignment on genome hg38 of the different TOP1cc ChIP-seq and LysoIP-seq at RAD23A gene loci as sequence tags per million (TPM).
(H) Immunofluorescence after 4 h of 50 nM CPT (nM) or 1 μM CPT (μM) and quantification ($n = 3$). Scale bar, 10 μm. Two-way ANOVA. *$p < 0.05$; ns, not significant.
See also Figure S4.

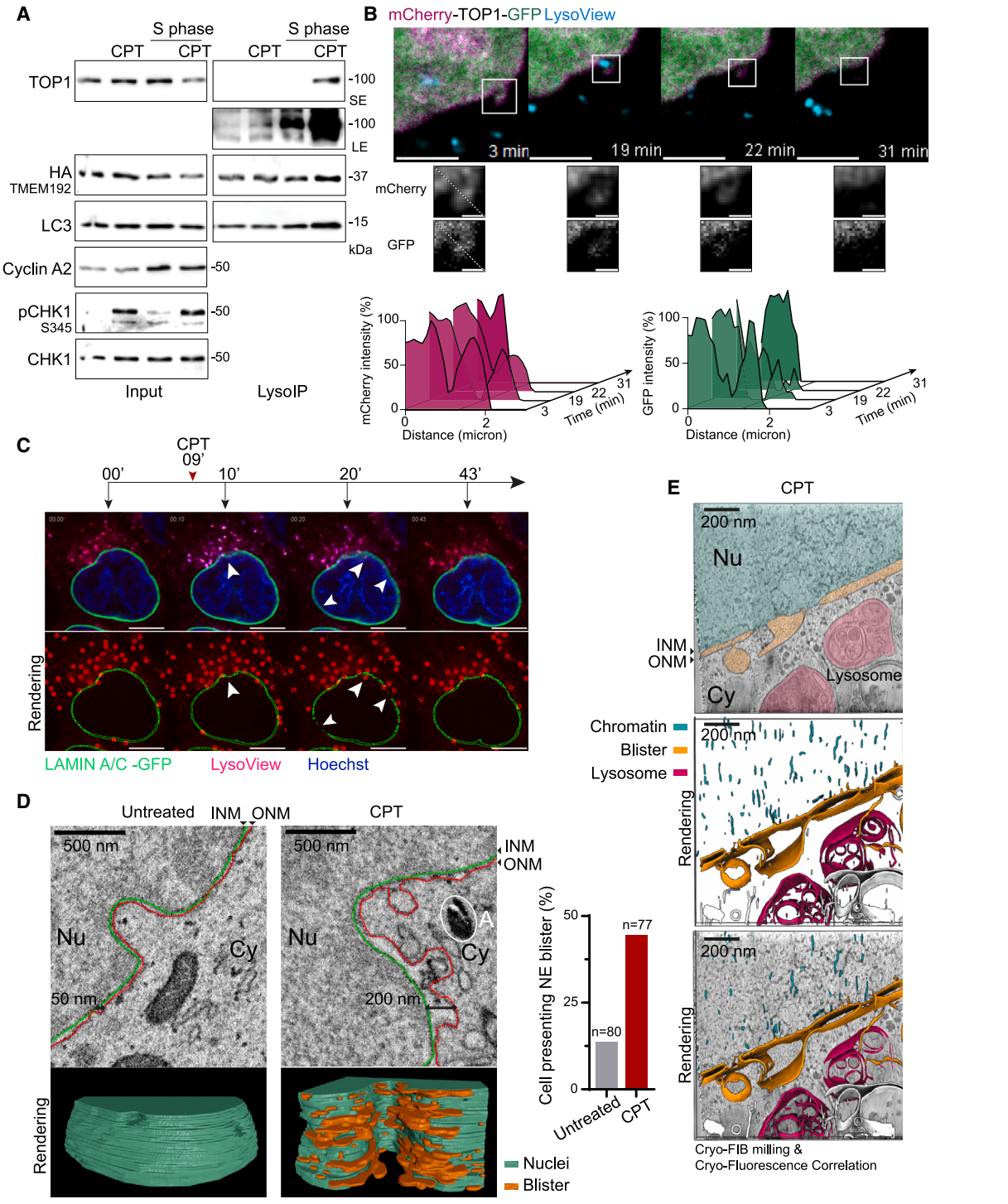

Figure 5. Lysosomal degradation of TOP1cc occurs in interphase cells through the nuclear envelope

(A) LysoIP performed after 6 h of 50 nM CPT in unsynchronized or S-phase HeLa cells (n = 3). SE, short exposure; LE, long exposure.

(B) Live-cell imaging started 3 min after treatment with 50 nM CPT. Normalized fluorescence intensity measured along the dashed line for both mCherry and GFP. Scale bar, 5 μm; zoom panel, 1 μm.

(C) Live-cell imaging. Arrows pointing at the alteration of Lamin A/C-GFP integrity at lysosomal contact sites (n = 3). Rendering by TrackMate of lysosomes and nuclear envelope integrity. Scale bar, 10 μm.

(legend continued on next page)

cells. However, treatment with CPT revealed abnormal enlargement of this space to more than 150 nm, forming blister-like structures protruding toward the cytoplasm. To exclude any technical artifacts due to the fixation process on the membrane structure, we confirmed the formation of the blister-like structure in response to CPT by using high-pressure freezing (Figure S5B). Cryo-focused ion beam (FIB) milling and cryo-fluorescence correlation images with the LysoTracker dye showed the proximity of lysosomes to the blister-like structures (Figures 5E and S5D).

Interestingly, similar blister-like structures were displayed in the nuclear envelope under ER stress.[95] These alterations are resolved by asymmetric autophagic digestion of the ONM. This was consistent with the enrichment of nuclear envelope proteins in intact lysosomes as identified by LysoIP mass spectrometry upon CPT treatment (Figures 1F and 1G). Moreover, inhibition of the major nuclear pore transport receptor, exportin-1, by leptomycin B, which is involved in the export of nucleic acids,[58,96,97] did not impact TOP1cc cytoplasmic localization in response to CPT (Figure S5C).

In summary, the nuclear protrusions observed by live imaging and electron microscopy, as well as the alterations observed in the lamina structure, suggest that TOP1cc processing by lysosomes occurs directly through the nuclear envelope.

TEX264 orchestrates TOP1cc repair by autophagy

To ensure cell survival and allow proliferation, the lysosomal degradation of genetic material and alterations of the nuclear envelope must be tightly regulated. So far, our data show that TOP1cc processing by lysosomes depends on selective autophagy mediated by ATG7, syntaxin 17, and RB1CC1 (Figures 2 and S2). Selective autophagy is tightly regulated and orchestrated by specific autophagy receptors that bind to cargo proteins. Among the 42 known autophagy receptors,[41,98,99] 6 were enriched in intact lysosomes in response to CPT treatment (Figure 6A; Table S3). Five of these six identified autophagy receptors in lysosomes were also present at the DNA replication fork, identified by NCC-SILAC proteomics[63] including TEX264. Given that TEX264 was recently recognized as essential for TOP1cc repair[29] and cell survival to low-dose CPT (Figure 3B), we asked whether TEX264 is the autophagy receptor that mediates TOP1cc repair by autophagy.

TEX264-knockout HeLa cells had defective TOP1cc repair and were hypersensitive to CPT compared with wild-type (WT) cells (Figures 3B, S6A, and S6B). Complementation of TEX264-knockout cells with TEX264-V5-WT fully restored cell survival and TOP1cc repair (Figures S6A and S6B). Structural analysis and previous interaction studies revealed defined domains in TEX264, such as TOP1-binding site (TBS), LIR, p97-binding motif (SHP), SUMO-interacting motif (SIM), and a phosphorylation site[29,33,34,100] (Figure 6B). To directly investigate the role of TEX264 in the autophagic degradation of TOP1cc, we created stable TEX264-V5 HeLa cell lines expressing either TEX264-WT or TEX264 variants in a TEX264-knockout background. Engineered cells expressing TEX264 variants were validated and displayed mild expression and proper cellular localization at the nuclear periphery (Figures 6C, S6C, and S6D).

Inactivation of TEX264 binding to TOP1, LC3, or p97 by mutations in its TBS, LIR, or SHP domains, respectively, abolished the TOP1cc repair compared with the TEX264-WT expression (Figure 6C). Furthermore, cells expressing TEX264 variants, which prevented their binding to TOP1, LC3, p97, or SUMO1, were defective in delivering TOP1 to lysosomes (Figure 6D). However, a mutation in the phosphorylation sites of TEX264, close to its LIR domain, had no impact on the delivery of TOP1 to lysosomes. As phosphorylation on two serines juxtaposed to the LIR region of TEX264 tunes its activity as a receptor for ER-phagy under starvation,[100] we concluded that these phosphorylation sites regulate its role in ER-phagy but not autophagy of TOP1cc.

In contrast, a mutation in the SIM domain of TEX264 strongly reduced TOP1 uptake in lysosomes (Figure 6D). Consistently, TOP1cc delivery to lysosomes was entirely blocked by using a specific E1-SUMO-activating enzyme inhibitor (ML792, Figure S6E). These data suggest that TOP1cc processing by lysosomes is dependent on SUMO. Because the E3-SUMO ligase PIAS4 and the SUMO-targeted ubiquitin ligase RNF4 are essential to direct TOP1cc for proteasomal degradation,[101] we investigated their role in regulating TOP1 delivery to lysosomes. Interestingly, neither PIAS4 nor RNF4 depletion prevented TOP1 uptake to the level of the specific E1-SUMO-activating enzyme inhibitor (Figure S6E). This implies that SUMOylation regulates TOP1cc lysosomal processing but in a PIAS4-independent manner. Lastly, TEX264 variants defective for binding to TOP1, LC3, p97, and SUMO were hypersensitive to CPT treatment compared with TEX264-WT cells (Figure 6E).

ATG7 regulates TEX264 binding to the replisome and autophagy machinery, MCM7 and LC3, respectively (Figure S1A). Therefore, we investigated where the TEX264-autophagy cascade starts in the cell using proximity ligation assay (PLA) between TEX264-V5 and LC3-GFP (Figure 6F). As established before, TEX264-LC3 interaction exists in the cytoplasm.[33,34] However, PLA demonstrated that TEX264 also interacts with LC3 inside the nucleus, near the nuclear periphery. Importantly, TEX264/LC3 interaction was abolished when the TEX264-LIR domain was mutated. Based on TEX264-LC3 interaction in the nucleus, the dependency on the LIR motif to deliver TOP1 to lysosomes (Figure 6D), and the recruitment of these two proteins at sites of DNA replication forks in response to CPT treatment (Figures 1C and 1D), we concluded that TEX264 is the receptor for TOP1cc degradation by autophagy within the nucleus at sites of stalled DNA replication forks.

(D) Volume electron microscopy images with nuclei segmentation and three-dimensional (3D) rendering after 30 min of 50 nM CPT. INM, inner nuclear membrane; ONM, outer nuclear membrane; Nu, nucleoplasm; Cy, cytoplasm; A, autophagosome. Scale bar, 500 nm. Blister-positive cells present at least 2 enlarged spaces between the INM and the ONM of more than 150 nm, close to a membrane invagination region.

(E) Cryo-focused ion beam (FIB) milling and cryo-fluorescence correlation using LysoTracker after 30 min of 50 nM CPT. (Top) Computational slice through a tomogram; (middle) segmentation of the tomogram; (bottom) overlay. Scale bar, 200 nm.

See also Figure S5 and Videos S1, S2, S3, and S4.

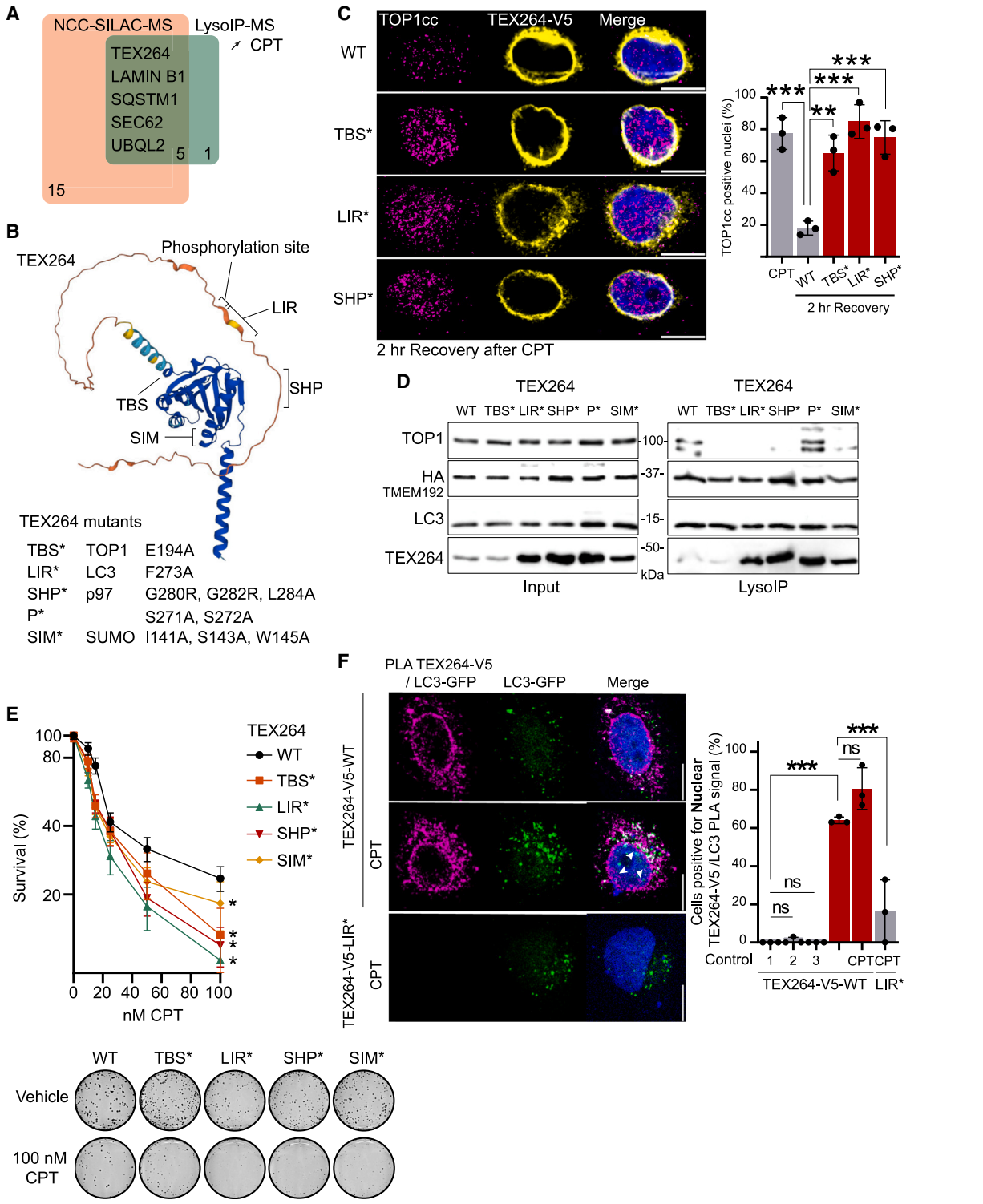

Figure 6. TEX264 is the receptor for TOP1cc degradation by selective autophagy

(A) Overlap of known autophagy receptors at replication fork by NCC-SILAC-MS[63] and in lysosomes upon 50 nM CPT by LysoIP-MS.

(B) AlphaFold prediction of TEX264 structure, with indicated domains.

(C) Immunofluorescence after 2 h of recovery after 2 h of 50 nM CPT and quantification (n = 3). Two-way ANOVA. Error bar, SD.

(legend continued on next page)

The TEX264-p97 axis orchestrates TOP1cc delivery to lysosomes

To investigate the role of p97 in TOP1cc processing by autophagy, we used the specific p97 inhibitor, CB-5083, which does not impact autophagy flux.[102,103] Similarly to the TEX264-SHP variant, p97 inhibition abolished TOP1 transfer to lysosomes and TOP1cc repair (Figures S6F and S6G). SPRTN was recently identified as a partner of p97 and TEX264 in the repair of TOP1cc,[29] so we investigated the role of SPRTN in the autophagy of TOP1cc. Interestingly, SPRTN inactivation did not affect TOP1cc delivery to lysosomes (Figure S6H) but caused the formation of cytoplasmic aggregates when the lysosomal function was blocked (Figure S7A). We concluded that SPRTN processes endogenous TOP1cc during S-phase,[29,30] and its inactivation combined with the lysosomal inactivation causes increased aggregate formation. These results suggest that the p97-TEX264 complex orchestrates TOP1cc delivery to lysosomes independently of SPRTN protease function.

TEX264 role in TOP1cc repair is evolutionarily conserved and relevant for chemotherapy response in the clinic

To investigate the role of TEX264 at the organismal level, we used a zebrafish model. Specific gene silencing of *tex264* in zebrafish embryos was achieved using morpholino oligonucleotides (*tex264*MO) and then complemented with either *tex264*-WT or LIR* sequence via co-injection into 1- to 4-cell-stage embryos. Despite robust *tex264* silencing and proper *tex264* re-expression, we did not observe any phenotypic changes in the zebrafish 2-day-old embryos (Figure 7A). Total genomic DNA was isolated from 2-day-old embryos, and TOP1cc level was analyzed by RADAR assay (Figure 7B). Inactivation of *tex264* caused an almost 2-fold increase in endogenous TOP1cc compared with the WT control embryos. The expression of *tex264*-WT, but not the autophagy-pathway-defective variant *tex264*-LIR*, prevented TOP1cc accumulation in *tex264*-depleted background. These data suggest that TEX264 and its autophagy role in TOP1cc repair are evolutionarily conserved and relevant at the organismal level.

Finally, to explore the relevance of TEX264 in a clinical setting, we analyzed TEX264 expression levels in 361 colorectal cancer primary tissues from patients treated with different chemotherapy regimens. We observed a strong positive association between TEX264 expression and the progression-free survival (PFS) of colorectal cancer patients in response to TOP1 inhibitor irinotecan (FOLFIRI: folinic acid, 5-fluorouracil [5-FU], and irinotecan) but not to 5-FU and folinic acid alone. Patients whose primary colorectal cancers express high levels of TEX264 had a 50% increase in PFS (9.1 months vs. 6.1 months, p value = 0.003) when treated with FOLFIRI compared with 5-FU and folinic acid (Figure 7C). In sum, TEX264-orchestrated autophagic repair of TOP1cc is highly relevant for response to irinotecan-based chemotherapy in the clinic and might prevent the increased genomic instability in colorectal cancers by ensuring proper DNA damage repair.

Indeed, depletion of TEX264 correlates with higher genomic instability measured by TOP1cc accumulation in cells (Figure S6A), the formation of Bloom syndrome protein (BLM)-positive ultrafine chromosomal bridges (Figure S7B), and DNA breaks measured by alkaline comet assay (Figure S7C). Moreover, TEX264 inactivation triggered a different mutational burden after long-term low-dose CPT treatment than in HeLa WT parental cells (Figures S7D–S7F). Whole-genome sequencing showed a shift to thymine-to-adenine (T>A) mutational profile compared with WT, corresponding to SBS25[104–106] and SBS34.[107] Finally, TEX264 inactivation combined with low-dose CPT induced the high formation of γ-H2AX/53BP1 foci, a recognized DSB marker (Figure S7G).[78] This effect is similar to the inactivation of ATR combined with the same dose of CPT, suggesting that TEX264 protects DNA replication fork collapse in response to TOP1cc. Based on all this evidence, we concluded that TEX264 mediates autophagic degradation of TOP1cc to protect DNA replication forks and, consequently, genome stability. These results are consistent with many publications correlating genomic instability to poor response to chemotherapy regimens and poor overall survival of colorectal cancer patients.[108–111]

DISCUSSION

Our findings demonstrate the direct involvement of selective autophagy in the repair of a specific type of nuclear DNA lesion, TOP1cc, in vertebrates (Figure 7D). As selective autophagy processes the nuclear DNA lesion, we refer to this process as nucleophagy. The mechanism of nucleophagy described here processes both endogenous and chemotherapy-relevant TOP1cc lesions that are excised from DNA replication forks by the nuclease MRE11. TOP1 and its associated DNA fragment are extruded from the nucleus to lysosomes through transient and restricted alteration of the nuclear envelope. Interestingly, besides TOP1cc, we also observed that replisome components were present in lysosomes after CPT-induced DNA damage. This suggests that, very likely, the replisome stalled at TOP1cc is excised and removed by nucleophagy. We focused our research on the mechanistic details of TOP1cc nucleophagy. However, the reason for the replisome or its components to be transported to lysosomes is unknown, and it will be essential to address in the future.

By comparing low- and high-dose CPT, we were able to elucidate that nucleophagy of TOP1cc is linked to stalled DNA replication. This process is inactivated when DNA replication forks collapse and are converted to DSBs. At high-dose CPT, TOP1cc

(D) LysoIP performed after 6 h of 50 nM CPT in TEX264^{KO} transiently expressing TEX264-WT or indicated TEX264 variants (n = 3).
(E) Clonogenic assay after 8 h of CPT (n = 3). Error bar, SEM.
(F) Proximity-ligation assay (PLA) between TEX264-V5-WT and LC3-GFP after 30 min of 50 nM CPT (n = 3) and quantification. Control 1, no LC3-GFP transfection; control 2, GFP antibody only (no V5); control 3, V5 antibody only (no GFP). Two-way ANOVA. Error bar, SD.
Scale bar, 10 μm. *p < 0.05; **p < 0.005; ***p < 0.0005; ns, not significant.
See also Figure S6 and Table S3.

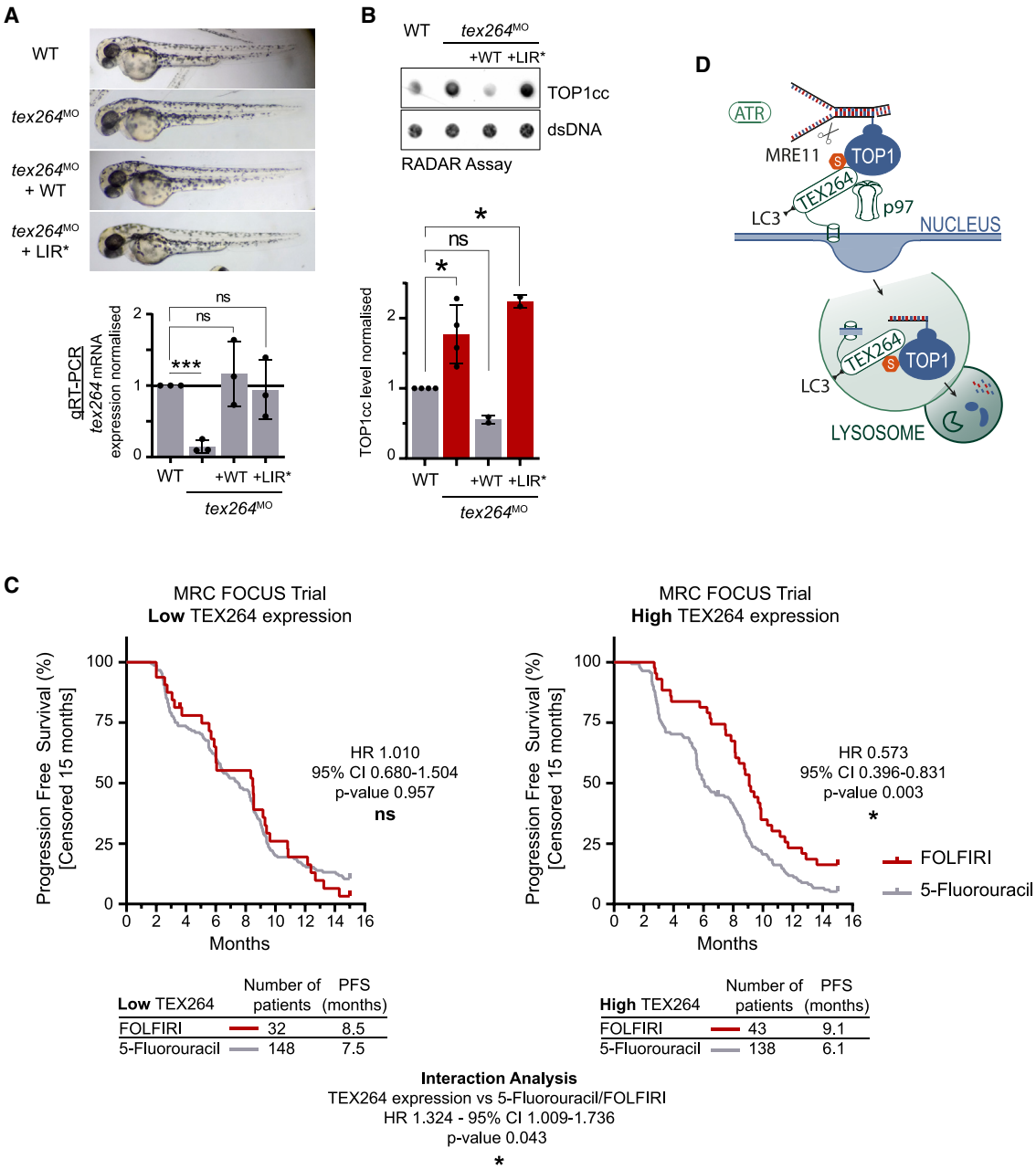

Figure 7. TEX264 expression level defines TOP1cc repair and the clinical response to irinotecan-based chemotherapy

(A) Representative images of 2-day-old zebrafish and RT-qPCR quantification of *tex264* expression. Two-way ANOVA. Error bar, SD.

(B) RADAR assay in 2-day-old zebrafish (lanes 1 and 2, $n = 4$; lanes 3 and 4, $n = 2$). Double-stranded (ds) DNA; loading control. Error bar, SD.

(C) Univariate Cox regression analysis of survival of colorectal cancer patients classified according to TEX264 mRNA expression. FOLFIRI: folinic acid, 5-fluorouracil (5-FU), and irinotecan.

(D) Model. S, SUMOylation.

*$p < 0.05$; ***$p < 0.0005$; ns, not significant.

See also Figure S7.

degradation primarily depends on proteasomal activity.[21–25] We hypothesize that the choice of the TOP1cc degradation pathway in the cell depends on the topological accessibility of the lesion. DSBs create more flexibility around the DNA damage[112,113] and could potentially facilitate the recruitment of the proteasome and downstream DNA-damage-repair proteins compared with a tighter conformation when the DNA replication fork is only stalled. Interestingly, a similar threshold concept for activating selective autophagy was also observed in the degradation of damaged mitochondria (mitophagy).[114] In response to

mitochondrial stress, autophagy regulates the removal of defective mitochondria. However, chronic stress leads to a complete cessation of mitophagy to prevent the potential depletion of mitochondria within the cell.

Specifically, we identified the autophagy factor TEX264 as a receptor for nucleophagy of TOP1cc. TEX264-mediated nucleophagy promotes DNA replication fork stability, genome stability, and cell survival response to DNA lesions induced by CPT. TEX264 bridges TOP1cc, stalled DNA replication and lysosomes, and orchestrates the export of DNA lesions to lysosomes in an ATR- but not ATM-dependent manner, further supporting the model that nucleophagy of TOP1cc is linked to DNA replication.

The questions arise: what are the roles of other degradation systems, namely the proteasome and SPRTN protease, in the removal of TOP1cc during DNA replication fork stalling as reported previously?[29–31,115] Inactivation of proteasome activity causes a pleiotropic effect on many cellular functions, including depletion of free nuclear ubiquitin.[116,117] By inactivation of the E3-ubiquitin ligase RNF4, which promotes proteasomal degradation of TOP1cc,[25,76,77] we overcame this pleiotropic effect of proteasomal inhibition and demonstrated that human cells were not sensitive to RNF4 inactivation when exposed to low-dose CPT that induces DNA replication stress but not DSBs. Our experiments also showed that the proteasome does not affect total TOP1 degradation after low-dose CPT. We concluded that the proteasome does not have a significant role in degrading TOP1cc around sites of DNA replication. On the contrary, the SPRTN protease was shown to process TOP1cc at/around sites of DNA replication[29–31,115] and SPRTN was shown to form a physical complex with TEX264 and p97 to process replication-related TOP1cc lesions.[29] However, the SPRTN protease cleaves specifically soluble proteins, including TOP1cc, during DNA replication fork progression and it works upstream of TDP1. This enzyme removes the remnant peptide from DNA after SPRTN proteolysis.[29–31,115,118] Neither SPRTN nor TDP1 inactivation prevented the delivery of TOP1 to lysosomes, but SPRTN inactivation increased the formation of aggregates. Based on these facts and previous knowledge of the role of SPRTN, we concluded that the p97-SPRTN complex removes soluble TOP1cc during DNA replication fork progression.

This work provides evidence that the p97-TEX264 pathway also operates during DNA replication and removes insoluble or aggregated TOP1cc by selective nucleophagy. This pathway depends on MRE11 nucleolytic cleavage of DNA lesions and is independent of SPRTN-TDP1 processing. Our conclusion is further supported by the fact that low-dose, but not high-dose, CPT induces the formation of aggregates.

Selective nucleophagy in yeast was discovered years ago, and different pathways co-exist.[53–55] However, no homolog for the yeast receptor atg39 that recognizes a substrate in the nucleus and delivers it to the autophagosome has been identified yet.[54,55] In mammals, nucleophagic clearance of abnormal nuclear content is observed in cells with laminar defects. In the context of laminopathies, inhibiting autophagy reduces cell viability, suggesting a beneficial role of autophagy in clearing leaking nuclear content.[60] In cancer cell lines and migrating primary cells, nuclear content is frequently transiently exposed and degraded by autophagy. This temporary loss of barrier integrity is often due to mechanical stress or weaknesses in the nuclear envelope structure.[91] However, how nucleophagy is orchestrated and how nucleophagy contributes to DNA repair and genome stability was not clear.

By discovering the TEX264-orchestrated nucleophagy pathway, we directly prove the existence of nucleophagy as a specialized DNA repair pathway in vertebrates. Whether this pathway also operates on other DNA-protein adducts remains to be further investigated. The increased T>A mutational profile in TEX264-inactivated cells treated with low-dose CPT led to the mutational signature resembling SBS25[104–106] and SBS34,[107] both of unknown etiology. This finding reinforces our statement that the TEX264-orchestrated TOP1cc nucleophagy pathway is a DNA repair mechanism that causes specific single base substitution (SBS) signatures when inactivated and does not belong to the previously described DNA repair pathway.

In summary, we reported TEX264-orchestrated selective nucleophagy of TOP1cc lesions as an evolutionarily conserved DNA repair pathway in vertebrates that operates at/around sites of DNA replication. This clinically relevant pathway promotes 50% better PFS in colorectal patients treated with the TOP1 inhibitor irinotecan. We believe this work opens avenues of research in biology, cancer therapy, and aging.

Limitations of the study

We suggest that the nucleophagy of TOP1cc is a DNA repair process that occurs at/around sites of DNA replication located at the nuclear periphery. Even though we showed that autophagy and the proteasome play a role in TOP1cc repair based on DNA structures induced by low-dose (stalled DNA replication) and high-dose (DSB) of CPT, respectively, it is still unknown how the different TOP1cc repair pathways cooperate at low-dose CPT. Interestingly, high-dose CPT also recruits autophagy factors at/around sites of DNA replication but to a lesser extent than low-dose CPT. The crosstalk between stalled or broken replication forks (converted to DSBs) and lysosomes should be investigated further. Finally, how the transient alteration of the nuclear envelope is formed and allows the transport of DNA lesions to lysosomes has yet to be discovered. Further work is needed to address the questions above and potentially translate this concept to the clinic.

Ethical consent

All subjects provided written informed consent for further research on their samples to the clinical trial. Both the original clinical trial (FOCUS Ref: 79877428) and S:CORT study (ref 15/EE/0241) were approved by the National Research Ethics Service in the United Kingdom.

RESOURCE AVAILABILITY

Lead contact

Further information and requests for resources and reagents should be directed to and will be fulfilled upon reasonable request by the lead contact, Kristijan Ramadan (kristijan.ramadan@ntu.edu.sg).

Materials availability

All unique/stable reagents generated in this study are available from the lead contact with a completed Materials Transfer Agreement.

Data and code availability

Both NGS datasets, LysoIP-Seq and WGS, are deposited to NCBI: GSE242298 and SRA: PRJNA1127335. The mass spectrometry proteomics data is deposited to the ProteomeXchange Consortium, PRIDE: PXD046037. Raw data are deposited on Mendeley Data: https://doi.org/10.17632/x6sv8zrjsv.1. The control arm of the FOCUS transcriptome is publicly available in GEO under accession number NCBI: GSE156915. The transcriptome of the irinotecan arm and additional S:CORT data is available to all academic researchers on submission of a data request to the data access committee. For commercial agencies, the data will be made available through Cancer Research Horizons on behalf of the funders and consortium members. This study did not generate a new unique code. Any additional information required to reanalyze the data reported in this paper is available from the lead contact upon request.

ACKNOWLEDGMENTS

We thank Drs H. Chino and N. Mizushima for generously providing the reagents and Misha Le Claire and Pranav Shah for their help with cryo-ET data processing. The Wellcome Trust Core award (203141/Z/16/Z) and the NIHR Oxford BRC supported access to computational resources. Clinical trial samples were obtained from the Medical Research Council (MRC) FOCUS trial and analyzed by the S:CORT consortium, which was funded by MRC and Cancer Research UK (MR/M016587/1).

MRC programme (MR/X006409/1), Breast Cancer Now (2022.11PR1570), Ministry of Education-Start-Up Grant, Singapore and Toh Kian Chui Distinguished Professorship Award supported K.R.; the Luxembourg National Fund (14548187) was awarded to P.L.; two MRC studentships were awarded to G.H. and C.P.; the Nuovo-Soldati Foundation Research Fellowship was awarded to C.P.; the MRC DTP from the University of Cambridge and the Cambridge Trust supported G.D.; the Saudi Arabian Cultural Bureau (1067945301) was awarded to F.A.; the Presidential Postdoctoral Fellowship (022543-00001) from Nanyang Technological University (NTU) Singapore was awarded to A.W.T.N.; the NIA-NIH (R56AG082790-01) was awarded to N.R.; the Croatian Science Foundation Installation Grant (UIP-2017-05-5258), Slovenian-Croatian Bilateral Research Project grant (IPS-2020-01-4225), and European Structural and Investment Funds STIM-REI project (KK.01.1.1.01.0003) was awarded to M.P.; the Wellcome Trust Investigator Award in Science (224361/Z/21/Z) and John Black Foundation was awarded to I.M.; and the Wellcome Trust Core Award (203141/Z/16/Z), with additional support from the NIHR Oxford BRC, was awarded to L.C.

AUTHOR CONTRIBUTIONS

Conceptualization, K.R. and P.L.; methodology, formal analysis, and investigation, P.L., G.H., S.T., C.T., A.R., I.T., S.K., Y.Z., I.A., C.O., H.Y., F.A., W.S., J.B., E.J., I.V., R.F., L.C., A.W.T.N., and J.N.; validation, P.L., C.T., G.H., S.T., I.A., and C.O.; resources, I.M., N.R., J.B., I.V., and E.J.; data curation, all authors; writing – original draft, P.L.; writing – review & editing, P.L. and K.R., with input from all authors; visualization, P.L.; supervision, K.R.; funding acquisition, P.L., M.P., I.M., N.R., and K.R.

DECLARATION OF INTERESTS

The authors declare no competing interests.

STAR★METHODS

Detailed methods are provided in the online version of this paper and include the following:

SUPPLEMENTAL INFORMATION

Supplemental information can be found online at https://doi.org/10.1016/j.cell.2024.08.020.

Received: October 27, 2023
Revised: June 4, 2024
Accepted: August 10, 2024
Published: September 11, 2024

REFERENCES

1. Pommier, Y., Sun, Y., Huang, S.N., and Nitiss, J.L. (2016). Roles of eukaryotic topoisomerases in transcription, replication and genomic stability. Nat. Rev. Mol. Cell Biol. *17*, 703–721. https://doi.org/10.1038/nrm.2016.111.
2. Watson, J.D., and Crick, F.H.C. (1953). Genetical Implications of the Structure of Deoxyribonucleic Acid. Nature *171*, 964–967. https://doi.org/10.1038/171964b0.
3. Corless, S., and Gilbert, N. (2016). Effects of DNA supercoiling on chromatin architecture. Biophys. Rev. *8*, 51–64. https://doi.org/10.1007/s12551-016-0242-6.
4. Ashour, M.E., Atteya, R., and El-Khamisy, S.F. (2015). Topoisomerase-mediated chromosomal break repair: an emerging player in many games. Nat. Rev. Cancer *15*, 137–151. https://doi.org/10.1038/nrc3892.
5. Brill, S.J., DiNardo, S., Voelkel-Meiman, K., and Sternglanz, R. (1987). Need for DNA topoisomerase activity as a swivel for DNA replication for transcription of ribosomal RNA. Nature *326*, 414–416. https://doi.org/10.1038/326414a0.
6. Pommier, Y. (2006). Topoisomerase I inhibitors: camptothecins and beyond. Nat. Rev. Cancer *6*, 789–802. https://doi.org/10.1038/nrc1977.
7. Stingele, J., Bellelli, R., and Boulton, S.J. (2017). Mechanisms of DNA–protein crosslink repair. Nat. Rev. Mol. Cell Biol. *18*, 563–573. https://doi.org/10.1038/nrm.2017.56.
8. Zimmermann, M., Murina, O., Reijns, M.A.M., Agathanggelou, A., Challis, R., Tarnauskaitė, Ž., Muir, M., Fluteau, A., Aregger, M., McEwan, A., et al. (2018). CRISPR screens identify genomic ribonucleotides as a source of

PARP-trapping lesions. Nature *559*, 285–289. https://doi.org/10.1038/s41586-018-0291-z.

9. Pommier, Y., Nussenzweig, A., Takeda, S., and Austin, C. (2022). Human topoisomerases and their roles in genome stability and organization. Nat. Rev. Mol. Cell Biol. *23*, 407–427. https://doi.org/10.1038/s41580-022-00452-3.
10. Rothenberg, M.L. (1997). Topoisomerase I inhibitors: Review and update. Ann. Oncol. *8*, 837–855. https://doi.org/10.1023/A:1008270717294.
11. Bailly, C. (2019). Irinotecan: 25 years of cancer treatment. Pharmacol. Res. *148*, 104398. https://doi.org/10.1016/j.phrs.2019.104398.
12. Thomas, A., and Pommier, Y. (2019). Targeting Topoisomerase I in the Era of Precision Medicine. Clin. Cancer Res. *25*, 6581–6589. https://doi.org/10.1158/1078-0432.CCR-19-1089.
13. Hammond, W.A., Swaika, A., and Mody, K. (2016). Pharmacologic resistance in colorectal cancer: a review. Ther. Adv. Med. Oncol. *8*, 57–84. https://doi.org/10.1177/1758834015614530.
14. Ozawa, S., Miura, T., Terashima, J., and Habano, W. (2021). Cellular irinotecan resistance in colorectal cancer and overcoming irinotecan refractoriness through various combination trials including DNA methyltransferase inhibitors: a review. Cancer Drug Resist. *4*, 946–964. https://doi.org/10.20517/cdr.2021.82.
15. Cortes Ledesma, F., El Khamisy, S.F., Zuma, M.C., Osborn, K., and Caldecott, K.W. (2009). A human 5′-tyrosyl DNA phosphodiesterase that repairs topoisomerase-mediated DNA damage. Nature *461*, 674–678. https://doi.org/10.1038/nature08444.
16. Zagnoli-Vieira, G., and Caldecott, K.W. (2020). Untangling trapped topoisomerases with tyrosyl-DNA phosphodiesterases. DNA Repair *94*, 102900. https://doi.org/10.1016/j.dnarep.2020.102900.
17. Pommier, Y., Huang, S.Y., Gao, R., Das, B.B., Murai, J., and Marchand, C. (2014). Tyrosyl-DNA-phosphodiesterases (TDP1 and TDP2). DNA Repair *19*, 114–129. https://doi.org/10.1016/j.dnarep.2014.03.020.
18. Rubio-Contreras, D., and Gómez-Herreros, F. (2023). TDP1 suppresses chromosomal translocations and cell death induced by abortive TOP1 activity during gene transcription. Nat. Commun. *14*, 6940. https://doi.org/10.1038/s41467-023-42622-7.
19. Sun, Y., Saha, S., Wang, W., Saha, L.K., Huang, S.N., and Pommier, Y. (2020). Excision repair of topoisomerase DNA-protein crosslinks (TOP-DPC). DNA Repair *89*, 102837. https://doi.org/10.1016/j.dnarep.2020.102837.
20. Sacho, E.J., and Maizels, N. (2011). DNA Repair Factor MRE11/RAD50 Cleaves 3′-Phosphotyrosyl Bonds and Resects DNA to Repair Damage Caused by Topoisomerase 1 Poisons. J. Biol. Chem. *286*, 44945–44951. https://doi.org/10.1074/jbc.M111.299347.
21. Desai, S.D., Liu, L.F., Vazquez-Abad, D., and D'Arpa, P. (1997). Ubiquitin-dependent Destruction of Topoisomerase I Is Stimulated by the Antitumor Drug Camptothecin. J. Biol. Chem. *272*, 24159–24164. https://doi.org/10.1074/jbc.272.39.24159.
22. Zhang, H.-F., Tomida, A., Koshimizu, R., Ogiso, Y., Lei, S., and Tsuruo, T. (2004). Cullin 3 Promotes Proteasomal Degradation of the Topoisomerase I-DNA Covalent Complex. Cancer Res. *64*, 1114–1121. https://doi.org/10.1158/0008-5472.CAN-03-2858.
23. Lin, C.-P., Ban, Y., Lyu, Y.L., Desai, S.D., and Liu, L.F. (2008). A Ubiquitin-Proteasome Pathway for the Repair of Topoisomerase I-DNA Covalent Complexes. J. Biol. Chem. *283*, 21074–21083. https://doi.org/10.1074/jbc.M803493200.
24. Lin, C.-P., Ban, Y., Lyu, Y.L., and Liu, L.F. (2009). Proteasome-dependent Processing of Topoisomerase I-DNA Adducts into DNA Double Strand Breaks at Arrested Replication Forks. J. Biol. Chem. *284*, 28084–28092. https://doi.org/10.1074/jbc.M109.030601.
25. Sun, Y., Chen, J., Huang, S.N., Su, Y.P., Wang, W., Agama, K., Saha, S., Jenkins, L.M., Pascal, J.M., and Pommier, Y. (2021). PARylation prevents the proteasomal degradation of topoisomerase I DNA-protein crosslinks and induces their deubiquitylation. Nat. Commun. *12*, 5010. https://doi.org/10.1038/s41467-021-25252-9.
26. Slichenmyer, W.J., Rowinsky, E.K., Donehower, R.C., and Kaufmann, S.H. (1993). The Current Status of Camptothecin Analogues as Antitumor Agents. J. Natl. Cancer Inst. *85*, 271–291. https://doi.org/10.1093/jnci/85.4.271.
27. Takimoto, C.H., and Arbuck, S.G. (1997). Clinical status and optimal use of topotecan. Oncology (Williston Park) *11*, 1635–1655.
28. Ray Chaudhuri, A., Hashimoto, Y., Herrador, R., Neelsen, K.J., Fachinetti, D., Bermejo, R., Cocito, A., Costanzo, V., and Lopes, M. (2012). Topoisomerase I poisoning results in PARP-mediated replication fork reversal. Nat. Struct. Mol. Biol. *19*, 417–423. https://doi.org/10.1038/nsmb.2258.
29. Fielden, J., Wiseman, K., Torrecilla, I., Li, S., Hume, S., Chiang, S.-C., Ruggiano, A., Narayan Singh, A., Freire, R., Hassanieh, S., et al. (2020). TEX264 coordinates p97- and SPRTN-mediated resolution of topoisomerase 1-DNA adducts. Nat. Commun. *11*, 1274. https://doi.org/10.1038/s41467-020-15000-w.
30. Vaz, B., Popovic, M., Newman, J.A., Fielden, J., Aitkenhead, H., Halder, S., Singh, A.N., Vendrell, I., Fischer, R., Torrecilla, I., et al. (2016). Metalloprotease SPRTN/DVC1 Orchestrates Replication-Coupled DNA-Protein Crosslink Repair. Mol. Cell *64*, 704–719. https://doi.org/10.1016/j.molcel.2016.09.032.
31. Stingele, J., Bellelli, R., Alte, F., Hewitt, G., Sarek, G., Maslen, S.L., Tsutakawa, S.E., Borg, A., Kjær, S., Tainer, J.A., et al. (2016). Mechanism and Regulation of DNA-Protein Crosslink Repair by the DNA-Dependent Metalloprotease SPRTN. Mol. Cell *64*, 688–703. https://doi.org/10.1016/j.molcel.2016.09.031.
32. Stingele, J., Schwarz, M.S., Bloemeke, N., Wolf, P.G., and Jentsch, S. (2014). A DNA-Dependent Protease Involved in DNA-Protein Crosslink Repair. Cell *158*, 327–338. https://doi.org/10.1016/j.cell.2014.04.053.
33. An, H., Ordureau, A., Paulo, J.A., Shoemaker, C.J., Denic, V., and Harper, J.W. (2019). TEX264 Is an Endoplasmic Reticulum-Resident ATG8-Interacting Protein Critical for ER Remodeling during Nutrient Stress. Mol. Cell *74*, 891–908.e10. https://doi.org/10.1016/j.molcel.2019.03.034.
34. Chino, H., Hatta, T., Natsume, T., and Mizushima, N. (2019). Intrinsically Disordered Protein TEX264 Mediates ER-phagy. Mol. Cell *74*, 909–921.e6. https://doi.org/10.1016/j.molcel.2019.03.033.
35. Dikic, I., and Elazar, Z. (2018). Mechanism and medical implications of mammalian autophagy. Nat. Rev. Mol. Cell Biol. *19*, 349–364. https://doi.org/10.1038/s41580-018-0003-4.
36. Morishita, H., and Mizushima, N. (2019). Diverse Cellular Roles of Autophagy. Annu. Rev. Cell Dev. Biol. *35*, 453–475. https://doi.org/10.1146/annurev-cellbio-100818-125300.
37. Klionsky, D.J. (2007). Autophagy: from phenomenology to molecular understanding in less than a decade. Nat. Rev. Mol. Cell Biol. *8*, 931–937. https://doi.org/10.1038/nrm2245.
38. Clarke, A.J., and Simon, A.K. (2019). Autophagy in the renewal, differentiation and homeostasis of immune cells. Nat. Rev. Immunol. *19*, 170–183. https://doi.org/10.1038/s41577-018-0095-2.
39. de Duve, C., and Wattiaux, R. (1966). Functions of Lysosomes. Annu. Rev. Physiol. *28*, 435–492. https://doi.org/10.1146/annurev.ph.28.030166.002251.
40. Klionsky, D.J. (2008). Autophagy revisited: A conversation with Christian de Duve. Autophagy *4*, 740–743. https://doi.org/10.4161/auto.6398.
41. Gubas, A., and Dikic, I. (2022). A guide to the regulation of selective autophagy receptors. FEBS J. *289*, 75–89. https://doi.org/10.1111/febs.15824.
42. Stolz, A., Ernst, A., and Dikic, I. (2014). Cargo recognition and trafficking in selective autophagy. Nat. Cell Biol. *16*, 495–501. https://doi.org/10.1038/ncb2979.
43. Komatsu, M., Waguri, S., Ueno, T., Iwata, J., Murata, S., Tanida, I., Ezaki, J., Mizushima, N., Ohsumi, Y., Uchiyama, Y., et al. (2005). Impairment of

starvation-induced and constitutive autophagy in Atg7-deficient mice. J. Cell Biol. *169*, 425–434. https://doi.org/10.1083/jcb.200412022.

44. Dikic, I. (2018). Open questions: why should we care about ER-phagy and ER remodelling? BMC Biol. *16*, 131. https://doi.org/10.1186/s12915-018-0603-7.
45. Khaminets, A., Heinrich, T., Mari, M., Grumati, P., Huebner, A.K., Akutsu, M., Liebmann, L., Stolz, A., Nietzsche, S., Koch, N., et al. (2015). Regulation of endoplasmic reticulum turnover by selective autophagy. Nature *522*, 354–358. https://doi.org/10.1038/nature14498.
46. Levine, B., and Kroemer, G. (2008). Autophagy in the Pathogenesis of Disease. Cell *132*, 27–42. https://doi.org/10.1016/j.cell.2007.12.018.
47. Holdgaard, S.G., Cianfanelli, V., Pupo, E., Lambrughi, M., Lubas, M., Nielsen, J.C., Eibes, S., Maiani, E., Harder, L.M., Wesch, N., et al. (2019). Selective autophagy maintains centrosome integrity and accurate mitosis by turnover of centriolar satellites. Nat. Commun. *10*, 4176. https://doi.org/10.1038/s41467-019-12094-9.
48. Robert, T., Vanoli, F., Chiolo, I., Shubassi, G., Bernstein, K.A., Rothstein, R., Botrugno, O.A., Parazzoli, D., Oldani, A., Minucci, S., et al. (2011). HDACs link the DNA damage response, processing of double-strand breaks and autophagy. Nature *471*, 74–79. https://doi.org/10.1038/nature09803.
49. Rodriguez-Rocha, H., Garcia-Garcia, A., Panayiotidis, M.I., and Franco, R. (2011). DNA damage and autophagy. Mutat. Res. *711*, 158–166. https://doi.org/10.1016/j.mrfmmm.2011.03.007.
50. Muciño-Hernández, G., Acevo-Rodríguez, P.S., Cabrera-Benitez, S., Guerrero, A.O., Merchant-Larios, H., and Castro-Obregón, S. (2023). Nucleophagy contributes to genome stability through degradation of type II topoisomerases A and B and nucleolar components. J. Cell Sci. *136*, jcs260563. https://doi.org/10.1242/jcs.260563.
51. Karantza-Wadsworth, V., Patel, S., Kravchuk, O., Chen, G., Mathew, R., Jin, S., and White, E. (2007). Autophagy mitigates metabolic stress and genome damage in mammary tumorigenesis. Genes Dev. *21*, 1621–1635. https://doi.org/10.1101/gad.1565707.
52. Ajazi, A., Bruhn, C., Shubassi, G., Lucca, C., Ferrari, E., Cattaneo, A., Bachi, A., Manfrini, N., Biffo, S., Martini, E., et al. (2021). Endosomal trafficking and DNA damage checkpoint kinases dictate survival to replication stress by regulating amino acid uptake and protein synthesis. Dev. Cell *56*, 2607–2622.e6. https://doi.org/10.1016/j.devcel.2021.08.019.
53. Pan, X., Roberts, P., Chen, Y., Kvam, E., Shulga, N., Huang, K., Lemmon, S., and Goldfarb, D.S. (2000). Nucleus–Vacuole Junctions in Saccharomyces cerevisiae Are Formed Through the Direct Interaction of Vac8p with Nvj1p. Mol. Biol. Cell *11*, 2445–2457. https://doi.org/10.1091/mbc.11.7.2445.
54. Mochida, K., Oikawa, Y., Kimura, Y., Kirisako, H., Hirano, H., Ohsumi, Y., and Nakatogawa, H. (2015). Receptor-mediated selective autophagy degrades the endoplasmic reticulum and the nucleus. Nature *522*, 359–362. https://doi.org/10.1038/nature14506.
55. Chino, H., and Mizushima, N. (2020). ER-Phagy: Quality Control and Turnover of Endoplasmic Reticulum. Trends Cell Biol. *30*, 384–398. https://doi.org/10.1016/j.tcb.2020.02.001.
56. Ivanov, A., Pawlikowski, J., Manoharan, I., van Tuyn, J., Nelson, D.M., Rai, T.S., Shah, P.P., Hewitt, G., Korolchuk, V.I., Passos, J.F., et al. (2013). Lysosome-mediated processing of chromatin in senescence. J. Cell Biol. *202*, 129–143. https://doi.org/10.1083/jcb.201212110.
57. Dou, Z., Xu, C., Donahue, G., Shimi, T., Pan, J.-A., Zhu, J., Ivanov, A., Capell, B.C., Drake, A.M., Shah, P.P., et al. (2015). Autophagy mediates degradation of nuclear lamina. Nature *527*, 105–109. https://doi.org/10.1038/nature15548.
58. Crossley, M.P., Song, C., Bocek, M.J., Choi, J.-H., Kousouros, J.N., Sathirachinda, A., Lin, C., Brickner, J.R., Bai, G., Lans, H., et al. (2023). R-loop-derived cytoplasmic RNA–DNA hybrids activate an immune response. Nature *613*, 187–194. https://doi.org/10.1038/s41586-022-05545-9.
59. Zhao, M., Wang, F., Wu, J., Cheng, Y., Cao, Y., Wu, X., Ma, M., Tang, F., Liu, Z., Liu, H., et al. (2021). CGAS is a micronucleophagy receptor for the clearance of micronuclei. Autophagy *17*, 3976–3991. https://doi.org/10.1080/15548627.2021.1899440.
60. Park, Y.-E., Hayashi, Y.K., Bonne, G., Arimura, T., Noguchi, S., Nonaka, I., and Nishino, I. (2009). Autophagic degradation of nuclear components in mammalian cells. Autophagy *5*, 795–804. https://doi.org/10.4161/auto.8901.
61. Lan, Y.Y., Londoño, D., Bouley, R., Rooney, M.S., and Hacohen, N. (2014). Dnase2a Deficiency Uncovers Lysosomal Clearance of Damaged Nuclear DNA via Autophagy. Cell Rep. *9*, 180–192. https://doi.org/10.1016/j.celrep.2014.08.074.
62. Fielden, J., Popović, M., and Ramadan, K. (2022). TEX264 at the intersection of autophagy and DNA repair. Autophagy *18*, 40–49. https://doi.org/10.1080/15548627.2021.1894059.
63. Nakamura, K., Kustatscher, G., Alabert, C., Hödl, M., Forne, I., Völker-Albert, M., Satpathy, S., Beyer, T.E., Mailand, N., Choudhary, C., et al. (2021). Proteome dynamics at broken replication forks reveal a distinct ATM-directed repair response suppressing DNA double-strand break ubiquitination. Mol. Cell *81*, 1084–1099.e6. https://doi.org/10.1016/j.molcel.2020.12.025.
64. Dungrawala, H., Rose, K.L., Bhat, K.P., Mohni, K.N., Glick, G.G., Couch, F.B., and Cortez, D. (2015). The Replication Checkpoint Prevents Two Types of Fork Collapse without Regulating Replisome Stability. Mol. Cell *59*, 998–1010. https://doi.org/10.1016/j.molcel.2015.07.030.
65. Ribeyre, C., Zellweger, R., Chauvin, M., Bec, N., Larroque, C., Lopes, M., and Constantinou, A. (2016). Nascent DNA Proteomics Reveals a Chromatin Remodeler Required for Topoisomerase I Loading at Replication Forks. Cell Rep. *15*, 300–309. https://doi.org/10.1016/j.celrep.2016.03.027.
66. Srivastava, M., Chen, Z., Zhang, H., Tang, M., Wang, C., Jung, S.Y., and Chen, J. (2018). Replisome Dynamics and Their Functional Relevance upon DNA Damage through the PCNA Interactome. Cell Rep. *25*, 3869–3883.e4. https://doi.org/10.1016/j.celrep.2018.11.099.
67. Abu-Remaileh, M., Wyant, G.A., Kim, C., Laqtom, N.N., Abbasi, M., Chan, S.H., Freinkman, E., and Sabatini, D.M. (2017). Lysosomal metabolomics reveals V-ATPase- and mTOR-dependent regulation of amino acid efflux from lysosomes. Science *358*, 807–813. https://doi.org/10.1126/science.aan6298.
68. Akasaki, K., Michihara, A., Mibuka, K., Fujiwara, Y., and Tsuji, H. (1995). Biosynthetic Transport of a Major Lysosomal Membrane Glycoprotein, Lamp-1: Convergence of Biosynthetic and Endocytic Pathways Occurs at Three Distinctive Points. Exp. Cell Res. *220*, 464–473. https://doi.org/10.1006/excr.1995.1338.
69. Patel, A.G., Flatten, K.S., Peterson, K.L., Beito, T.G., Schneider, P.A., Perkins, A.L., Harki, D.A., and Kaufmann, S.H. (2016). Immunodetection of human topoisomerase I-DNA covalent complexes. Nucleic Acids Res. *44*, 2816–2826. https://doi.org/10.1093/nar/gkw109.
70. Torrecilla, I., Ruggiano, A., Kiianitsa, K., Aljarbou, F., Lascaux, P., Hoslett, G., Song, W., Maizels, N., and Ramadan, K. (2024). Isolation and detection of DNA–protein crosslinks in mammalian cells. Nucleic Acids Res. *52*, 525–547. https://doi.org/10.1093/nar/gkad1178.
71. Wang, R.C., Wei, Y., An, Z., Zou, Z., Xiao, G., Bhagat, G., White, M., Reichelt, J., and Levine, B. (2012). Akt-Mediated Regulation of Autophagy and Tumorigenesis Through Beclin 1 Phosphorylation. Science *338*, 956–959. https://doi.org/10.1126/science.1225967.
72. Kiianitsa, K., and Maizels, N. (2013). A rapid and sensitive assay for DNA-protein covalent complexes in living cells. Nucleic Acids Res. *41*, e104. https://doi.org/10.1093/nar/gkt171.
73. Itakura, E., Kishi-Itakura, C., and Mizushima, N. (2012). The Hairpin-type Tail-Anchored SNARE Syntaxin 17 Targets to Autophagosomes for Fusion with Endosomes/Lysosomes. Cell *151*, 1256–1269. https://doi.org/10.1016/j.cell.2012.11.001.

74. Hara, T., Takamura, A., Kishi, C., Iemura, S.-I., Natsume, T., Guan, J.-L., and Mizushima, N. (2008). FIP200, a ULK-interacting protein, is required for autophagosome formation in mammalian cells. J. Cell Biol. *181*, 497–510. https://doi.org/10.1083/jcb.200712064.

75. Kimura, S., Noda, T., and Yoshimori, T. (2007). Dissection of the Autophagosome Maturation Process by a Novel Reporter Protein, Tandem Fluorescent-Tagged LC3. Autophagy *3*, 452–460. https://doi.org/10.4161/auto.4451.

76. Yin, Y., Seifert, A., Chua, J.S., Maure, J.-F., Golebiowski, F., and Hay, R.T. (2012). SUMO-targeted ubiquitin E3 ligase RNF4 is required for the response of human cells to DNA damage. Genes Dev. *26*, 1196–1208. https://doi.org/10.1101/gad.189274.112.

77. Liu, J.C.Y., Ackermann, L., Hoffmann, S., Gál, Z., Hendriks, I.A., Jain, C., Morlot, L., Tatham, M.H., McLelland, G.-L., Hay, R.T., et al. (2024). Concerted SUMO-targeted ubiquitin ligase activities of TOPORS and RNF4 are essential for stress management and cell proliferation. Nat. Struct. Mol. Biol. *1*, 1–13. https://doi.org/10.1038/s41594-024-01294-7.

78. de Feraudy, S., Revet, I., Bezrookove, V., Feeney, L., and Cleaver, J.E. (2010). A minority of foci or pan-nuclear apoptotic staining of γH2AX in the S phase after UV damage contain DNA double-strand breaks. Proc. Natl. Acad. Sci. USA *107*, 6870–6875. https://doi.org/10.1073/pnas.1002175107.

79. Liu, S., Opiyo, S.O., Manthey, K., Glanzer, J.G., Ashley, A.K., Amerin, C., Troksa, K., Shrivastav, M., Nickoloff, J.A., and Oakley, G.G. (2012). Distinct roles for DNA-PK, ATM and ATR in RPA phosphorylation and checkpoint activation in response to replication stress. Nucleic Acids Res. *40*, 10780–10794. https://doi.org/10.1093/nar/gks849.

80. Williams, R.M., and Zhang, X. (2021). Roles of ATM and ATR in DNA double strand breaks and replication stress. Prog. Biophys. Mol. Biol. *161*, 27–38. https://doi.org/10.1016/j.pbiomolbio.2020.11.005.

81. Ravikumar, B., Duden, R., and Rubinsztein, D.C. (2002). Aggregate-prone proteins with polyglutamine and polyalanine expansions are degraded by autophagy. Hum. Mol. Genet. *11*, 1107–1117. https://doi.org/10.1093/hmg/11.9.1107.

82. Shen, D., Coleman, J., Chan, E., Nicholson, T.P., Dai, L., Sheppard, P.W., and Patton, W.F. (2011). Novel Cell- and Tissue-Based Assays for Detecting Misfolded and Aggregated Protein Accumulation Within Aggresomes and Inclusion Bodies. Cell Biochem. Biophys. *60*, 173–185. https://doi.org/10.1007/s12013-010-9138-4.

83. Zhang, H., Xiong, Y., Su, D., Wang, C., Srivastava, M., Tang, M., Feng, X., Huang, M., Chen, Z., and Chen, J. (2022). TDP1-independent pathways in the process and repair of TOP1-induced DNA damage. Nat. Commun. *13*, 4240. https://doi.org/10.1038/s41467-022-31801-7.

84. Marini, V., Nikulenkov, F., Samadder, P., Juul, S., Knudsen, B.R., and Krejci, L. (2023). MUS81 cleaves TOP1-derived lesions and other DNA–protein cross-links. BMC Biol. *21*, 110. https://doi.org/10.1186/s12915-023-01614-1.

85. Regairaz, M., Zhang, Y.-W., Fu, H., Agama, K.K., Tata, N., Agrawal, S., Aladjem, M.I., and Pommier, Y. (2011). Mus81-mediated DNA cleavage resolves replication forks stalled by topoisomerase I–DNA complexes. J. Cell Biol. *195*, 739–749. https://doi.org/10.1083/jcb.201104003.

86. Hanada, K., Budzowska, M., Davies, S.L., van Drunen, E., Onizawa, H., Beverloo, H.B., Maas, A., Essers, J., Hickson, I.D., and Kanaar, R. (2007). The structure-specific endonuclease Mus81 contributes to replication restart by generating double-strand DNA breaks. Nat. Struct. Mol. Biol. *14*, 1096–1104. https://doi.org/10.1038/nsmb1313.

87. Tan, Y., Yao, L., Gamliel, A., Nair, S.J., Taylor, H., Ohgi, K., Aggarwal, A.K., and Rosenfeld, M.G. (2023). Signal-induced enhancer activation requires Ku70 to read topoisomerase1–DNA covalent complexes. Nat. Struct. Mol. Biol. *30*, 148–158. https://doi.org/10.1038/s41594-022-00883-8.

88. Baranello, L., Wojtowicz, D., Cui, K., Devaiah, B.N., Chung, H.-J., Chan-Salis, K.Y., Guha, R., Wilson, K., Zhang, X., Zhang, H., et al. (2016). RNA Polymerase II Regulates Topoisomerase 1 Activity to Favor Efficient Transcription. Cell *165*, 357–371. https://doi.org/10.1016/j.cell.2016.02.036.

89. Aze, A., Sannino, V., Soffientini, P., Bachi, A., and Costanzo, V. (2016). Centromeric DNA replication reconstitution reveals DNA loops and ATR checkpoint suppression. Nat. Cell Biol. *18*, 684–691. https://doi.org/10.1038/ncb3344.

90. Vargas, J.D., Hatch, E.M., Anderson, D.J., and Hetzer, M.W. (2012). Transient nuclear envelope rupturing during interphase in human cancer cells. Nucleus *3*, 88–100. https://doi.org/10.4161/nucl.18954.

91. Karoutas, A., and Akhtar, A. (2021). Functional mechanisms and abnormalities of the nuclear lamina. Nat. Cell Biol. *23*, 116–126. https://doi.org/10.1038/s41556-020-00630-5.

92. Karoutas, A., Szymanski, W., Rausch, T., Guhathakurta, S., Rog-Zielinska, E.A., Peyronnet, R., Seyfferth, J., Chen, H.-R., de Leeuw, R., Herquel, B., et al. (2019). The NSL complex maintains nuclear architecture stability via lamin A/C acetylation. Nat. Cell Biol. *21*, 1248–1260. https://doi.org/10.1038/s41556-019-0397-z.

93. Srivastava, N., Nader, G.P.F., Williart, A., Rollin, R., Cuvelier, D., Lomakin, A., and Piel, M. (2021). Nuclear fragility, blaming the blebs. Curr. Opin. Cell Biol. *70*, 100–108. https://doi.org/10.1016/j.ceb.2021.01.007.

94. Crisp, M., Liu, Q., Roux, K., Rattner, J.B., Shanahan, C., Burke, B., Stahl, P.D., and Hodzic, D. (2006). Coupling of the nucleus and cytoplasm: Role of the LINC complex. J. Cell Biol. *172*, 41–53. https://doi.org/10.1083/jcb.200509124.

95. Kucińska, M.K., Fedry, J., Galli, C., Morone, D., Raimondi, A., Soldà, T., Förster, F., and Molinari, M. (2023). TMX4-driven LINC complex disassembly and asymmetric autophagy of the nuclear envelope upon acute ER stress. Nat. Commun. *14*, 3497. https://doi.org/10.1038/s41467-023-39172-3.

96. Koo, C.X., Kobiyama, K., Shen, Y.J., LeBert, N., Ahmad, S., Khatoo, M., Aoshi, T., Gasser, S., and Ishii, K.J. (2015). RNA Polymerase III Regulates Cytosolic RNA:DNA Hybrids and Intracellular MicroRNA Expression. J. Biol. Chem. *290*, 7463–7473. https://doi.org/10.1074/jbc.M115.636365.

97. Chatzidoukaki, O., Stratigi, K., Goulielmaki, E., Niotis, G., Akalestou-Clocher, A., Gkirtzimanaki, K., Zafeiropoulos, A., Altmüller, J., Topalis, P., and Garinis, G.A. (2021). R-loops trigger the release of cytoplasmic ssDNAs leading to chronic inflammation upon DNA damage. Sci. Adv. *7*, eabj5769. https://doi.org/10.1126/sciadv.abj5769.

98. Johansen, T., and Lamark, T. (2020). Selective Autophagy: ATG8 Family Proteins, LIR Motifs and Cargo Receptors. J. Mol. Biol. *432*, 80–103. https://doi.org/10.1016/j.jmb.2019.07.016.

99. Deng, Z., Purtell, K., Lachance, V., Wold, M.S., Chen, S., and Yue, Z. (2017). Autophagy Receptors and Neurodegenerative Diseases. Trends Cell Biol. *27*, 491–504. https://doi.org/10.1016/j.tcb.2017.01.001.

100. Chino, H., Yamasaki, A., Ode, K.L., Ueda, H.R., Noda, N.N., and Mizushima, N. (2022). Phosphorylation by casein kinase 2 enhances the interaction between ER-phagy receptor TEX264 and ATG8 proteins. EMBO Rep. *23*, e54801. https://doi.org/10.15252/embr.202254801.

101. Sun, Y., Miller Jenkins, L.M., Su, Y.P., Nitiss, K.C., Nitiss, J.L., and Pommier, Y. (2020). A conserved SUMO pathway repairs topoisomerase DNA-protein cross-links by engaging ubiquitin-mediated proteasomal degradation. Sci. Adv. *6*, eaba6290. https://doi.org/10.1126/sciadv.aba6290.

102. Wang, F., Li, S., Cheng, K.-W., Rosencrans, W.M., and Chou, T.-F. (2022). The p97 Inhibitor UPCDC-30245 Blocks Endo-Lysosomal Degradation. Pharmaceuticals (Basel) *15*, 204. https://doi.org/10.3390/ph15020204.

103. Kilgas, S., and Ramadan, K. (2023). Inhibitors of the ATPase p97/VCP: From basic research to clinical applications. Cell Chem. Biol. *30*, 3–21. https://doi.org/10.1016/j.chembiol.2022.12.007.

104. Alexandrov, L.B., Jones, P.H., Wedge, D.C., Sale, J.E., Campbell, P.J., Nik-Zainal, S., and Stratton, M.R. (2015). Clock-like mutational

processes in human somatic cells. Nat. Genet. *47*, 1402–1407. https://doi.org/10.1038/ng.3441.

105. Nik-Zainal, S., Davies, H., Staaf, J., Ramakrishna, M., Glodzik, D., Zou, X., Martincorena, I., Alexandrov, L.B., Martin, S., Wedge, D.C., et al. (2016). Landscape of somatic mutations in 560 breast cancer whole-genome sequences. Nature *534*, 47–54. https://doi.org/10.1038/nature17676.

106. Petljak, M., Alexandrov, L.B., Brammeld, J.S., Price, S., Wedge, D.C., Grossmann, S., Dawson, K.J., Ju, Y.S., Iorio, F., Tubio, J.M.C., et al. (2019). Characterizing Mutational Signatures in Human Cancer Cell Lines Reveals Episodic APOBEC Mutagenesis. Cell *176*, 1282–1294.e20. https://doi.org/10.1016/j.cell.2019.02.012.

107. Alexandrov, L.B., Kim, J., Haradhvala, N.J., Huang, M.N., Tian Ng, A.W., Wu, Y., Boot, A., Covington, K.R., Gordenin, D.A., Bergstrom, E.N., et al. (2020). The repertoire of mutational signatures in human cancer. Nature *578*, 94–101. https://doi.org/10.1038/s41586-020-1943-3.

108. Bakhoum, S.F., Ngo, B., Laughney, A.M., Cavallo, J.-A., Murphy, C.J., Ly, P., Shah, P., Sriram, R.K., Watkins, T.B.K., Taunk, N.K., et al. (2018). Chromosomal instability drives metastasis through a cytosolic DNA response. Nature *553*, 467–472. https://doi.org/10.1038/nature25432.

109. Li, J., Hubisz, M.J., Earlie, E.M., Duran, M.A., Hong, C., Varela, A.A., Lettera, E., Deyell, M., Tavora, B., Havel, J.J., et al. (2023). Non-cell-autonomous cancer progression from chromosomal instability. Nature *620*, 1080–1088. https://doi.org/10.1038/s41586-023-06464-z.

110. Namløs, H.M., Khelik, K., Nakken, S., Vodák, D., Hovig, E., Myklebost, O., Boye, K., and Meza-Zepeda, L.A. (2023). Chromosomal instability and a deregulated cell cycle are intrinsic features of high-risk gastrointestinal stromal tumours with a metastatic potential. Mol. Oncol. *17*, 2432–2450. https://doi.org/10.1002/1878-0261.13514.

111. Lukow, D.A., Sausville, E.L., Suri, P., Chunduri, N.K., Wieland, A., Leu, J., Smith, J.C., Girish, V., Kumar, A.A., Kendall, J., et al. (2021). Chromosomal instability accelerates the evolution of resistance to anti-cancer therapies. Dev. Cell *56*, 2427–2439.e4. https://doi.org/10.1016/j.devcel.2021.07.009.

112. Strecker, J., Gupta, G.D., Zhang, W., Bashkurov, M., Landry, M.-C., Pelletier, L., and Durocher, D. (2016). DNA damage signalling targets the kinetochore to promote chromatin mobility. Nat. Cell Biol. *18*, 281–290. https://doi.org/10.1038/ncb3308.

113. Kruhlak, M.J., Celeste, A., Dellaire, G., Fernandez-Capetillo, O., Müller, W.G., McNally, J.G., Bazett-Jones, D.P., and Nussenzweig, A. (2006). Changes in chromatin structure and mobility in living cells at sites of DNA double-strand breaks. J. Cell Biol. *172*, 823–834. https://doi.org/10.1083/jcb.200510015.

114. Deus, C.M., Yambire, K.F., Oliveira, P.J., and Raimundo, N. (2020). Mitochondria–Lysosome Crosstalk: From Physiology to Neurodegeneration. Trends Mol. Med. *26*, 71–88. https://doi.org/10.1016/j.molmed.2019.10.009.

115. Ruggiano, A., Vaz, B., Kilgas, S., Popović, M., Rodriguez-Berriguete, G., Singh, A.N., Higgins, G.S., Kiltie, A.E., and Ramadan, K. (2021). The protease SPRTN and SUMOylation coordinate DNA-protein crosslink repair to prevent genome instability. Cell Rep. *37*, 110080. https://doi.org/10.1016/j.celrep.2021.110080.

116. Dantuma, N.P., Groothuis, T.A.M., Salomons, F.A., and Neefjes, J. (2006). A dynamic ubiquitin equilibrium couples proteasomal activity to chromatin remodeling. J. Cell Biol. *173*, 19–26. https://doi.org/10.1083/jcb.200510071.

117. Collins, G.A., and Goldberg, A.L. (2017). The Logic of the 26S Proteasome. Cell *169*, 792–806. https://doi.org/10.1016/j.cell.2017.04.023.

118. Anticevic, I., Otten, C., Vinkovic, L., Jukic, L., and Popovic, M. (2023). Tyrosyl-DNA phosphodiesterase 1 (TDP1) and SPRTN protease repair histone 3 and topoisomerase 1 DNA–protein crosslinks in vivo. Open Biol. *13*, 230113. https://doi.org/10.1098/rsob.230113.

119. Malla, S.B., Fisher, D.J., Domingo, E., Blake, A., Hassanieh, S., Redmond, K.L., Richman, S.D., Youdell, M., Walker, S.M., Logan, G.E., et al. (2021). In-depth Clinical and Biological Exploration of DNA Damage Immune Response as a Biomarker for Oxaliplatin Use in Colorectal Cancer. Clin. Cancer Res. *27*, 288–300. https://doi.org/10.1158/1078-0432.CCR-20-3237.

120. Ritz, D., Vuk, M., Kirchner, P., Bug, M., Schütz, S., Hayer, A., Bremer, S., Lusk, C., Baloh, R.H., Lee, H., et al. (2011). Endolysosomal sorting of ubiquitylated caveolin-1 is regulated by VCP and UBXD1 and impaired by VCP disease mutations. Nat. Cell Biol. *13*, 1116–1123. https://doi.org/10.1038/ncb2301.

121. Jumper, J., Evans, R., Pritzel, A., Green, T., Figurnov, M., Ronneberger, O., Tunyasuvunakool, K., Bates, R., Žídek, A., Potapenko, A., et al. (2021). Highly accurate protein structure prediction with AlphaFold. Nature *596*, 583–589. https://doi.org/10.1038/s41586-021-03819-2.

122. Varadi, M., Anyango, S., Deshpande, M., Nair, S., Natassia, C., Yordanova, G., Yuan, D., Stroe, O., Wood, G., Laydon, A., et al. (2022). AlphaFold Protein Structure Database: massively expanding the structural coverage of protein-sequence space with high-accuracy models. Nucleic Acids Res. *50*, D439–D444. https://doi.org/10.1093/nar/gkab1061.

123. Zheng, S., Wolff, G., Greenan, G., Chen, Z., Faas, F.G.A., Bárcena, M., Koster, A.J., Cheng, Y., and Agard, D.A. (2022). AreTomo: An integrated software package for automated marker-free, motion-corrected cryo-electron tomographic alignment and reconstruction. J. Struct. Biol. X *6*, 100068. https://doi.org/10.1016/j.yjsbx.2022.100068.

124. Ermel, U.H., Arghittu, S.M., and Frangakis, A.S. (2022). ArtiaX: An electron tomography toolbox for the interactive handling of sub-tomograms in UCSF ChimeraX. Protein Sci. *31*, e4472. https://doi.org/10.1002/pro.4472.

125. Weigert, M., Schmidt, U., Boothe, T., Müller, A., Dibrov, A., Jain, A., Wilhelm, B., Schmidt, D., Broaddus, C., Culley, S., et al. (2018). Content-aware image restoration: pushing the limits of fluorescence microscopy. Nat. Methods *15*, 1090–1097. https://doi.org/10.1038/s41592-018-0216-7.

126. Carpenter, A.E., Jones, T.R., Lamprecht, M.R., Clarke, C., Kang, I.H., Friman, O., Guertin, D.A., Chang, J.H., Lindquist, R.A., Moffat, J., et al. (2006). CellProfiler: image analysis software for identifying and quantifying cell phenotypes. Genome Biol. *7*, R100. https://doi.org/10.1186/gb-2006-7-10-r100.

127. Pettersen, E.F., Goddard, T.D., Huang, C.C., Meng, E.C., Couch, G.S., Croll, T.I., Morris, J.H., and Ferrin, T.E. (2021). UCSF ChimeraX: Structure visualization for researchers, educators, and developers. Protein Sci. *30*, 70–82. https://doi.org/10.1002/pro.3943.

128. Rohou, A., and Grigorieff, N. (2015). CTFFIND4: Fast and accurate defocus estimation from electron micrographs. J. Struct. Biol. *192*, 216–221. https://doi.org/10.1016/j.jsb.2015.08.008.

129. Yu, F., Haynes, S.E., and Nesvizhskii, A.I. (2021). IonQuant Enables Accurate and Sensitive Label-Free Quantification With FDR-Controlled Match-Between-Runs. Mol. Cell. Proteomics *20*, 100077. https://doi.org/10.1016/j.mcpro.2021.100077.

130. Schindelin, J., Arganda-Carreras, I., Frise, E., Kaynig, V., Longair, M., Pietzsch, T., Preibisch, S., Rueden, C., Saalfeld, S., Schmid, B., et al. (2012). Fiji: an Open-Source platform for biological-image analysis. Nat. Methods *9*, 676–682. https://doi.org/10.1038/nmeth.2019.

131. Kremer, J.R., Mastronarde, D.N., and McIntosh, J.R. (1996). Computer Visualization of Three-Dimensional Image Data Using IMOD. J. Struct. Biol. *116*, 71–76. https://doi.org/10.1006/jsbi.1996.0013.

132. Robinson, J.T., Thorvaldsdóttir, H., Winckler, W., Guttman, M., Lander, E.S., Getz, G., and Mesirov, J.P. (2011). Integrative genomics viewer. Nat. Biotechnol. *29*, 24–26. https://doi.org/10.1038/nbt.1754.

133. Gyori, B.M., Venkatachalam, G., Thiagarajan, P.S., Hsu, D., and Clement, M.-V. (2014). OpenComet: An automated tool for comet assay image analysis. Redox Biol. *2*, 457–465. https://doi.org/10.1016/j.redox.2013.12.020.

134. Tyanova, S., Temu, T., Sinitcyn, P., Carlson, A., Hein, M.Y., Geiger, T., Mann, M., and Cox, J. (2016). The Perseus computational platform for comprehensive analysis of (prote)omics data. Nat. Methods *13*, 731–740. https://doi.org/10.1038/nmeth.3901.

135. Nakane, T., Kimanius, D., Lindahl, E., and Scheres, S.H. (2018). Characterisation of molecular motions in cryo-EM single-particle data by multi-body refinement in RELION. eLife *7*, e36861. https://doi.org/10.7554/eLife.36861.

136. Mastronarde, D.N. (2003). SerialEM: A Program for Automated Tilt Series Acquisition on Tecnai Microscopes Using Prediction of Specimen Position. Microsc. Microanal. *9*, 1182–1183. https://doi.org/10.1017/S1431927603445911.

137. Ershov, D., Phan, M.-S., Pylvänäinen, J.W., Rigaud, S.U., Le Blanc, L., Charles-Orszag, A., Conway, J.R.W., Laine, R.F., Roy, N.H., Bonazzi, D., et al. (2022). TrackMate 7: integrating state-of-the-art segmentation algorithms into tracking pipelines. Nat. Methods *19*, 829–832. https://doi.org/10.1038/s41592-022-01507-1.

138. Aleström, P., D'Angelo, L., Midtlyng, P.J., Schorderet, D.F., Schulte-Merker, S., Sohm, F., and Warner, S. (2020). Zebrafish: Housing and husbandry recommendations. Lab. Anim. *54*, 213–224. https://doi.org/10.1177/0023677219869037.

139. Seymour, M.T., Maughan, T.S., Ledermann, J.A., Topham, C., James, R., Gwyther, S.J., Smith, D.B., Shepherd, S., Maraveyas, A., Ferry, D.R., et al. (2007). Different strategies of sequential and combination chemotherapy for patients with poor prognosis advanced colorectal cancer (MRC FOCUS): a randomised controlled trial. Lancet *370*, 143–152. https://doi.org/10.1016/S0140-6736(07)61087-3.

140. Sirbu, B.M., Couch, F.B., Feigerle, J.T., Bhaskara, S., Hiebert, S.W., and Cortez, D. (2011). Analysis of protein dynamics at active, stalled, and collapsed replication forks. Genes Dev. *25*, 1320–1327. https://doi.org/10.1101/gad.2053211.

141. Hanssen, F., Garcia, M.U., Folkersen, L., Pedersen, A.S., Lescai, F., Jodoin, S., Miller, E., Seybold, M., Wacker, O., Smith, N., et al. (2024). Scalable and efficient DNA sequencing analysis on different compute infrastructures aiding variant discovery. NAR Genom. Bioinform. *6*, lqae031. https://doi.org/10.1093/nargab/lqae031.

142. McKenna, A., Hanna, M., Banks, E., Sivachenko, A., Cibulskis, K., Kernytsky, A., Garimella, K., Altshuler, D., Gabriel, S., Daly, M., et al. (2010). The Genome Analysis Toolkit: A MapReduce framework for analyzing next-generation DNA sequencing data. Genome Res. *20*, 1297–1303. https://doi.org/10.1101/gr.107524.110.

143. Kim, S., Scheffler, K., Halpern, A.L., Bekritsky, M.A., Noh, E., Källberg, M., Chen, X., Kim, Y., Beyter, D., Krusche, P., et al. (2018). Strelka2: fast and accurate calling of germline and somatic variants. Nat. Methods *15*, 591–594. https://doi.org/10.1038/s41592-018-0051-x.

144. Díaz-Gay, M., Vangara, R., Barnes, M., Wang, X., Islam, S.M.A., Vermes, I., Duke, S., Narasimman, N.B., Yang, T., Jiang, Z., et al. (2023). Assigning mutational signatures to individual samples and individual somatic mutations with SigProfilerAssignment. Bioinformatics *39*, btad756. https://doi.org/10.1093/bioinformatics/btad756.

145. Tate, J.G., Bamford, S., Jubb, H.C., Sondka, Z., Beare, D.M., Bindal, N., Boutselakis, H., Cole, C.G., Creatore, C., Dawson, E., et al. (2019). COSMIC: the Catalogue Of Somatic Mutations In Cancer. Nucleic Acids Res. *47*, D941–D947. https://doi.org/10.1093/nar/gky1015.

146. Sanchez, M.A., Tran, K.D., Valli, J., Hobbs, S., Johnson, E., Gluenz, E., and Landfear, S.M. (2016). KHARON Is an Essential Cytoskeletal Protein Involved in the Trafficking of Flagellar Membrane Proteins and Cell Division in African Trypanosomes. J. Biol. Chem. *291*, 19760–19773. https://doi.org/10.1074/jbc.M116.739235.

147. Johnson, E., Seiradake, E., Jones, E.Y., Davis, I., Grünewald, K., and Kaufmann, R. (2015). Correlative in-resin super-resolution and electron microscopy using standard fluorescent proteins. Sci. Rep. *5*, 9583. https://doi.org/10.1038/srep09583.

148. Eisenstein, F., Yanagisawa, H., Kashihara, H., Kikkawa, M., Tsukita, S., and Danev, R. (2023). Parallel cryo electron tomography on in situ lamellae. Nat. Methods *20*, 131–138. https://doi.org/10.1038/s41592-022-01690-1.

149. Lamm, L., Righetto, R.D., Wietrzynski, W., Pöge, M., Martinez-Sanchez, A., Peng, T., and Engel, B.D. (2022). MemBrain: A deep learning-aided pipeline for detection of membrane proteins in Cryo-electron tomograms. Comput. Methods Programs Biomed. *224*, 106990. https://doi.org/10.1016/j.cmpb.2022.106990.

150. Hazeki, N., Tukamoto, T., Goto, J., and Kanazawa, I. (2000). Formic Acid Dissolves Aggregates of an N-Terminal Huntingtin Fragment Containing an Expanded Polyglutamine Tract: Applying to Quantification of Protein Components of the Aggregates. Biochem. Biophys. Res. Commun. *277*, 386–393. https://doi.org/10.1006/bbrc.2000.3682.

151. Nasevicius, A., and Ekker, S.C. (2000). Effective targeted gene 'knockdown' in zebrafish. Nat. Genet. *26*, 216–220. https://doi.org/10.1038/79951.

152. Simon, P. (2003). Q-Gene: processing quantitative real-time RT–PCR data. Bioinformatics *19*, 1439–1440. https://doi.org/10.1093/bioinformatics/btg157.

153. Popovic, M., Zaja, R., and Smital, T. (2010). Organic anion transporting polypeptides (OATP) in zebrafish (*Danio rerio*): Phylogenetic analysis and tissue distribution. Comp. Biochem. Physiol. A Mol. Integr. Physiol. *155*, 327–335. https://doi.org/10.1016/j.cbpa.2009.11.011.

154. Irizarry, R.A., Hobbs, B., Collin, F., Beazer-Barclay, Y.D., Antonellis, K.J., Scherf, U., and Speed, T.P. (2003). Exploration, normalization, and summaries of high density oligonucleotide array probe level data. Biostatistics *4*, 249–264. https://doi.org/10.1093/biostatistics/4.2.249.

STAR★METHODS

KEY RESOURCES TABLE

REAGENT or RESOURCE	SOURCE	IDENTIFIER
Antibodies		
Rabbit polyclonal anti-BLM	Abcam	Cat# ab2179, RRID:AB_2290411
Rabbit polyclonal anti-Cyclin B1	Cell Signaling Technology	Cat# 4138, RRID:AB_2072132
Rabbit polyclonal anti-GFP antibody	Abcam	Cat# ab290, RRID:AB_303395
Rat monoclonal anti-HA (Immunofluorescence)	Roche	Cat# 11867423001, RRID:AB_390918
Rabbit monoclonal anti-LAMP1	Cell Signaling Technology	Cat# 9091, RRID:AB_2687579
Mouse monoclonal anti-RPA32/RPA2	Abcam	Cat# ab2175, RRID:AB_302873
Mouse monoclonal anti-TOP1cc	Millipore	Cat# MABE 1084, RRID:AB_2756354
Rabbit polyclonal anti-V5	Abcam	Cat# ab9116, RRID:AB_307024
Mouse monoclonal anti-V5 antibody (PLA)	Innovative Research	Cat# R96025, RRID:AB_159313
Mouse monoclonal anti-γ-H2AX	Sigma-Aldrich	Cat# 05636
Rabbit polyclonal anti-53BP1 (Low vs High dose)	Santa Cruz Biotechnology	Cat# SC-22760, RRID:AB_2256326
Rabbit polyclonal anti-53BP1 (TEX264^{KO}, ATRi)	Cell Signaling Technology	Cat# 4937, RRID:AB_10694558
Rabbit monoclonal anti-ATG7	Cell Signaling Technology	Cat# 8558, RRID:AB_10831194
Rabbit monoclonal anti-phospho-ATM (Ser1981) – pATM S1981	Abcam	Cat# ab81292, RRID:AB_1640207
Mouse monoclonal anti-ATM	Sigma-Aldrich	Cat# A1106, RRID:AB_796190
Rabbit polyclonal anti-Beclin-1	Proteintech	Cat# 11306-1-AP, RRID:AB_2259061
Rabbit monoclonal anti-Calreticulin	Cell Signaling Technology	Cat# 12238, RRID:AB_2688013
Rabbit monoclonal anti-phospho-CHK1 (Ser354) – pCHK1 S354	Cell Signaling Technology	Cat# 2348, RRID:AB_331212
Rabbit monoclonal anti-CHK1	Abcam	Cat# ab32531, RRID:AB_726821
Rabbit polyclonal anti-phospho-CHK2 (Thr68) – pCHK2 (T68)	Cell Signaling Technology	Cat# 2661, RRID:AB_331479
Rabbit polyclonal anti-CHK2	Cell Signaling Technology	Cat# 2662, RRID:AB_2080793
Rabbit polyclonal anti-CHMP7	Proteintech	Cat# 16424-1-AP, RRID:AB_2079500
Rabbit recombinant monoclonal anti-Cyclin A2	Abcam	Cat# ab181591, RRID:AB_2890136
Rabbit polyclonal anti-DNA Polymerase alpha – POL α	Abcam	Cat# ab31777, RRID:AB_731976
Rabbit recombinant monoclonal anti-DNA Polymerase delta, catalytic subunit – POL δ	Abcam	Cat# Ab306083
Mouse monoclonal anti-dsDNA	Abcam	Cat# ab27156, RRID:AB_470907
Rabbit polyclonal anti-EEA1	Thermo Fisher Scientific	Cat # PA1-063A, RRID:AB_2096819
Rabbit polyclonal anti-GAPDH	Proteintech	Cat# 10494-1-AP, RRID:AB_2263076
Rabbit polyclonal anti-HA	Santa Cruz Biotechnology	Cat# sc-805, RRID:AB_631618
Mouse monoclonal anti-Histone H3	BioLegend	Cat# 819414, RRID:AB_2832857
Rabbit monoclonal anti-LAMP1	Cell Signaling Technology	Cat# 9091T, RRID:AB_2687579
Rabbit polyclonal anti-LC3B	Cell Signaling Technology	Cat# 2775, RRID:AB_915950
Mouse monoclonal anti-MCM7	Santa Cruz Biotechnology	Cat# sc-9966, RRID:AB_627235
Rabbit polyclonal anti-MRE11	Abcam	Cat# 33125; RRID:AB_776530
Mouse Monoclonal anti-MUS81	Sigma-Aldrich	Cat# M1445, RRID:AB_532259
Rabbit monoclonal anti-PARP	Abcam	Cat# ab32138, RRID:AB_777101

(*Continued on next page*)

Continued

REAGENT or RESOURCE	SOURCE	IDENTIFIER
Rabbit polyclonal anti-PCNA	Santa Cruz Biotechnology	Cat# sc-7907, RRID:AB_2160375
Mouse monoclonal anti-PIAS4	Millipore	Cat# 217669, RRID:AB_211625
Rabbit polyclonal anti-Rab7	Novus Biologicals	Cat# NBP1-05048, RRID:AB_1522232
Mouse monoclonal anti-RANBP2	Santa Cruz Biotechnology	Cat# sc-74518, RRID:AB_2176784
Rabbit polyclonal anti-RB1CC1 (FIP200)	Proteintech	Cat# 17250-1-AP, RRID:AB_10666428
Rabbit polyclonal anti-RNF4	Proteintech	Cat# 17810-1-AP, RRID:AB_2878443
Rabbit polyclonal anti-RPL7	Abcam	Cat# ab72550, RRID:AB_1270391
Rabbit polyclonal anti-SPRTN	Atlas Antibodies	Cat# HPA025073, RRID:AB_1847695
Rabbit monoclonal anti-SNAP29	Abcam	Cat# ab138500, RRID:AB_2687667
Rabbit polyclonal anti-STX17 (Syntaxin 17)	Sigma-Aldrich	Cat# HPA001204, RRID:AB_1080118
Rabbit polyclonal anti-TDP1	Abcam	Cat# ab4166, RRID:AB_304337
Rabbit polyclonal anti-TEX264	Fielden et al.[29]	N/A (gift)
Rabbit polyclonal anti-phospho-TEX264, GASGpSpSFEEL (a.a. 267–276 of TEX264) – pTEX264	Chino et al.[100]	N/A (gift)
Rabbit polyclonal anti-TOP1	Bethyl	Cat# A302-589A, RRID:AB_2034865
Mouse monoclonal anti-TOP1 antibody (Zebrafish)	Santa Cruz Biotechnology	Cat# sc-271285, RRID:AB_10611597
Mouse recombinant monoclonal anti-mono- and polyubiquitinylated conjugates – Poly-ub	Enzo Life Sciences	Cat# ENZ-ABS840, RRID:AB_2935893
Rabbit polyclonal anti-VCP/p97	Proteintech	Cat# 10736-1-AP, RRID:AB_2214635
Rabbit polyclonal anti-VCP/p97 (IPOND)	Novus Biologicals	Cat# NB100-1557, RRID:AB_2272824
Rabbit monoclonal anti-VDAC1	Cell Signaling Technology	Cat# 4661, RRID:AB_10557420
Bacterial and Virus Strains		
NEB® 5-alpha Competent E. coli (High Efficiency)	New England Biolabs	Cat# C2987
Chemicals, peptides, and recombinant proteins		
Bafilomycin A1	LKT Labs	Cat# B0025
Blasticidin	Cayman Chemical	Cat# 14499
Bortezomib	ApexBio	Cat# A2614-APE
Camptothecin	Sigma-Aldrich	Cat# 208925
CB-5083	Selleck Chemical	Cat# S8101
Doxycycline	PanReac AppliChem	Cat# A2951,0025
Irinotecan	Sigma-Aldrich	Cat# I1406
KU-55933	Selleck Chemical	Cat# S1092
Leptomycin B	Cayman Chemical	Cat# CAY10004976
ML792	MedChem Express	Cat# HY-108702
MG132	Calbiochem	Cat# 474787
Pen-strep	Sigma-Aldrich	Cat# P4333
Puromycin	Sigma-Aldrich	Cat# P8833
SN38	Selleck Chemical	Cat# S4908
Torin-1	Cell Signaling Technology	Cat# 14379
VE-822	Selleck Chemical	Cat# S7102
EdU	Thermo Fisher Scientific	Cat# A10044
Biotin	Sigma-Aldrich	Cat# B4501
FuGENE® HD	Promega	Cat# E2311
Lipofectamine™ RNAiMAX	Thermo Fisher Scientific	Cat# 13778150
Polyethylenimine, PEI	Sigma-Aldrich	Cat# 408727

(*Continued on next page*)

Continued

REAGENT or RESOURCE	SOURCE	IDENTIFIER
Resazurin powder	Sigma-Aldrich	Cat# R7017
Benzonase	Millipore	Cat# 71205
Low Melt Agarose	BioRad	Cat# 1613111
LysoTracker™ Deep Red	Thermo Fisher Scientific	Cat# L12492
LysoView™ 680	Biotium	Cat# 70086
Proteostat®	Enzo	Cat# ENZ-51035-0025
Hoechst 34580	Thermo Fisher Scientific	Cat# H21486
VECTASHIELD antifade mounting medium	Eurobio Scientific	Cat# H-1000
ProLong™ Glass Antifade Mountant	Invitrogen	Cat# P36982
SYBR™ Gold Nucleic Acid Gel Stain	Invitrogen	Cat# S11494
Protein A Magnetic Beads	New England BioLabs	Cat# S1425S
Pierce anti-HA magnetic beads	Thermo Fisher Scientific	Cat# 88837
Strep-Tactin® Sepharose® resin	Iba LifeSciences	Cat# 2-1201-010
Streptavidin agarose beads	Novagen	Cat# 69203
V5-Trap® agarose beads	Chomoteck	Cat# v5ta
Critical commercial assays		
Acclaim™ PepMap™ 100 C18 HPLC Columns (100 μm x 2 cm)	Thermo Fisher Scientific	Cat# 164750
ARCA kit	New England Biolabs	Cat# S1411
Bio-Dot Microfiltration System	BioRad	Cat# 1703938
Duolink® In Situ Detection Reagents FarRed	Sigma-Aldrich	Cat# DUO92013
Duolink® In Situ PLA® Probe Anti-Mouse MINUS	Sigma-Aldrich	Cat# DUO92004
Duolink® In Situ PLA® Probe Anti-Rabbit PLUS	Sigma-Aldrich	Cat# DUO92002
EASY-Spray™ HPLC column (2 μm, 100 A, 74 μm x 500 mm)	Thermo Fisher Scientific	Cat# ES903
Genomic DNA Buffer Set	Qiagen	Cat# 19060
GoTaq qPCR mix	Promega	Cat# A6001
Hieff NGS® OnePot Pro DNA Library Prep Kit V2	Yeasen	Cat# 12195E
HiScribe SP6 RNA kit	New England Biolabs	Cat# E2070
In-Fusion® Snap Assembly Master Mix	Takara Bio	Cat# 638947
Monarch Total RNA Miniprep Kit	New England Biolabs	Cat# T2040L
MycoAlert™ Mycoplasma Detection Kit	Lonza Bioscience	Cat# LT07-318
NEBuilder® HiFi DNA Assembly Cloning Kit	New England Biolabs	Cat# E5520S
ProtoScript II First Strand cDNA Synthesis Kit	New England Biolabs	Cat# E6560L
Quant-iT™ PicoGreen™	Thermo Fisher Scientific	Cat# P11496
Quantifoil™ R 2/2 on 200 gold mesh grids	Jenna Bioscience	Cat# X-103-Au200
QuikChange Lightning Multi Site-Directed Mutagenesis Kit	Agilent	Cat# 210515
S-Trap™ micro columns	Protifi	Cat# C02-micro
T4 polynucleotide kinase	New England BioLabs	Cat# M0201S
VAHTS Dual UMI UDI Adapters Set 1 – Set 4 for Illumina	Vazyme	Cat# N351
Deposited data		
Raw mass spectrometry data	This paper	ProteomeXchange Consortium PRIDE: PXD046037

(*Continued on next page*)

Continued

REAGENT or RESOURCE	SOURCE	IDENTIFIER
Bigwig files of LysoIP-Seq	This paper	NCBI: GSE242298
BAM files of WGS	This paper	SRA: PRJNA1127335
Raw data on Mendeley	This paper	Mendeley Data: https://doi.org/10.17632/x6sv8zrjsv.1
MRC FOCUS transcriptome	Malla et al.[119]	NCBI: GSE156915
Experimental models: Cell lines		
HeLa	ATCC	Cat# CCL-2
HeLa TEX264^{KO}	Fielden et al.[29] Generated with sc-417333 (Santa Cruz)	N/A
HeLa Δ-SPRTN (partial knockout)	Vaz et al.[30]	N/A
HEK293T	ATCC	Cat# CRL-3216
HEK293 Dox-inducible p97 Myc/Strep tagged	Ritz et al.[120]	N/A
HCT116	ATCC	Cat# CCL-247
HeLa shATG7	This study, generated with V3SH11252-224923093 (Dharmacon)	N/A
HeLa shSTX17	This study, generated with V3SH11252-224923093 (Dharmacon)	N/A
hTERT RPE-1	ATCC	Cat# CRL-4000
Experimental models: Organisms/strains		
Zebrafish AB strain (*Danio rerio*)	European Zebrafish Resource Centre (EZRC), Germany	Cat# 1175
Oligonucleotides		
siATG7 – CCAACACACUCGAGUCUUU	Dharmacon	Cat# J-020112-05-0010
shATG7 – CAGTTGGATGGGAAAAGAA	Dharmacon	Cat# V3SH11252-224923093
siMRE11 – GAGCAUAACUCCAUAAGUA	Thermo Fisher Scientific	Cat# 10620310
siMUS81 – Smart pool	Dharmacon	Cat# L-016143-01-0005
siPIAS4 – Exon 2	Silencer Ambion	Cat# s28370
siRB1CC1 (FIP200) – GGAGUGGGCUGGUGCUUUA	Dharmacon	Cat# J-021117-05
siRNF4 – GCUAAUACUUGCCCAACUU, GAAUGGACGUCUCAUCGUU, GACAGAGACGUAUAUGUGA, GCAAUAAAUUCUAGACAAG	Dharmacon – Smart pool	Cat# 006557-00-0005
siSPRTN – GUCAGGAAGUUCUGGUUAA	Microsynth	N/A
shSTX17 – TTTGAGGTGTTAGAAGACAGG Clone 118 used in figures	Dharmacon	Cat# RHS3979-201777905
shSTX17 – AATGAATTTCTGGATAGCTGG Confirmation	Dharmacon	Cat# RHS3979-201777909
siTDP1 – GGAUAUUGCGUUUGGAACA	Silencer Ambion	Cat# s31481
tex264^{MO} (splice) GTCATAAAGGGTCGAGCTACTGACC	Genetools (LCC)	N/A
tex264^{MO} (ATG) AAGTCCGACATTTTTGTTTGCCCGG	Genetools (LCC)	N/A
RT-PCR *tex264*_F ACCGAAGCTCTCGTCTGTC	Macrogen	N/A
RT-PCR *tex264*_R GGAGTTCTTCGTCGGGTTTC	Macrogen	N/A
RT-PCR *atp50*_F CTTGCAGAGCTGAAAGTGGC	Macrogen	N/A

(*Continued on next page*)

Continued

REAGENT or RESOURCE	SOURCE	IDENTIFIER
RT-PCR *atp50*_R sACCACCAA GGATTGAGGCAT	Macrogen	N/A
KpnI_TOP1_F GCAACCTTGGG TACCGATGAGTGGGGACCAC CTCCAC	Invitrogen	N/A
BamHI_TOP1_R AAGGTTGCGAC CGGTGGATCCCGAAACTCATAG TCTTCATCAGCCATGTCAAT	Invitrogen	N/A
TEX-pLX313_Fwd aggtgtcgtga ggctagcATGTCGGACCTGCTAC TACTGGGC	Invitrogen	N/A
TEX-pLX313_Rev gataggcttacc gatatcCTCCTTGCCCTTCTCA GGGGC	Invitrogen	N/A
*tex264*_F	AGAGGATCTGCTCGAGAT GTCGGACTTTATCATTTTACTGC	N/A
*tex264*_R	TCACTATAGTTCTAGATCA CTCTTCCCTGTTGCCC	N/A
*tex264*_F283A LIR mutagenesis	GGCAGCGGCTCCTCCgcTG AAGAACTAGACCTG	N/A
Recombinant DNA		
LC3- pEGFP-C2	Addgene	RRID:Addgene_24920
mCherry-GFP-pEGFP-N1	Addgene	RRID: Addgene_86639
mCherry-TOP1-GFP-pEGFP-N1	This Study	N/A
pCDH_blast_MCS_Nard_GFP_LAMIN	Addgene	RRID:Addgene_167340
pLJC5-TMEM192-3xHA	Addgene	RRID:Addgene_102930
pLJC6-3XHA-TMEM192	Addgene	RRID:Addgene_104434
TEX264-V5-pLX313	This Study	N/A
pLX313-TP53-WT	Addgene	RRID:Addgene_118014
pCS2+HisMyc	Addgene	RRID:Addgene_ 24682
Software and algorithms		
AlphaFold	Jumper et al.[121] and Varadi et al.[122]	https://alphafold.ebi.ac.uk/
AreTomo v1.3.3	Zheng et al.[123]	https://msg.ucsf.edu/software
Arivis 4D	Zeiss Software	https://www.arivis.com/products/pro
ArtiaX	Ermel et al.[124]	https://github.com/FrangakisLab/ArtiaX
CARE	Weigert et al.[125]	https://csbdeep.bioimagecomputing.com/tools/care/
CellProfiler™	Carpenter et al.[126]	https://cellprofiler.org/
ChimeraX	Pettersen et al.[127]	https://www.cgl.ucsf.edu/chimerax/
CTFFIND4 v4.14	Rohou and Grigorieff[128]	https://grigoriefflab.umassmed.edu/ctffind4
Fragpipe v19.1	Yu et al.[129]	https://fragpipe.nesvilab.org/
ImageJ	Schindelin et al.[130]	https://imagej.net/Fiji/Downloads
IMOD	Kremer et al.[131]	https://bio3d.colorado.edu/imod/
Integrative Genomics Viewer – IGV	Robinson et al.[132]	https://software.broadinstitute.org/software/igv/
OpenComet – ImageJ plugin	Gyori et al.[133]	https://cometbio.org/
Perseus v1.6.2.2	Tyanova et al.[134]	https://maxquant.net/download_asset/perseus/latest
Prism v10	GraphPad Software	https://www.graphpad.com

(*Continued on next page*)

Continued

REAGENT or RESOURCE	SOURCE	IDENTIFIER
RELION v5.0 beta	Nakane et al.[135]	https://relion.readthedocs.io/en/release-5.0/
SerialEM v4.1 beta	Mastronarde[136]	https://bio3d.colorado.edu/SerialEM/
TrackMate – ImageJ plugin	Ershov et al.[137]	https://imagej.net/plugins/trackmate/
WebUI v1.1	Thermo Fisher Scientific	https://stable-diffusion-art.com/automatic1111/

EXPERIMENTAL MODEL AND SUBJECT DETAILS

Cell culture and transfection

All experiments were performed in HeLa cells unless stated otherwise. HeLa, HEK293T, HCT116, and hTERT RPE-1 cells were obtained from ATCC and grown with Dulbecco's modified Eagle medium (DMEM) containing 10% fetal bovine serum (FBS) and 1% Penicillin/Streptomycin, at 37 °C at 5% CO_2. All cell lines were regularly screened for mycoplasma using a MycoAlert™ Mycoplasma Detection Kit. Cell synchronisation was performed using Thymidine (2 mM). Treatments were performed on attached cells for the indicated time with Bafilomycin A1 (BAF, 50 nM), Torin-1 (150 nM for clonogenic assay and 250 nM for immunoblot and immunofluorescence assays), Leptomycin B (LTB, 10 nM), MG132 (2 μM), CB-5083 (10 μM), VE-822 (Berzosertib, ATR inhibitor, 1 μM), KU-55933 (ATM inhibitor, 1 μM), Irinotecan (5 μM), SN38 (50 nM), ML792 (1 μM) or Bortezomib (5 μM). Camptothecin treatment (CPT) was done using 50 nM unless indicated otherwise (100 nM or 1 μM). Live imaging experiments were performed in FluoroBrite™ DMEM.

Cloning procedure

Cloning of the mCherry-TOP1-GFP construct for the reporter assay was performed by inserting the TOP1 DNA sequence[29] into the backbone mCherry-GFP-pEGFP-N1 (Addgene). Due to the challenging cloning procedure to insert TOP1 into a lentivirus backbone, transient expression was performed with the above construct mCherry-TOP1-GFP-pEGFP-N1. It was expressed transiently for 24 hr before imaging. The backbone was linearised by KpnI and BamHI. Phusion Hot Start II High-Fidelity DNA Polymerase (Thermofisher) was used to amplify the TOP1 sequence with primers (KpnI_TOP1_F and BamHI_TOP1_R). Ligation was performed using NEBuilder® HiFi DNA Assembly Cloning Kit (NEB) following the manufacturer's instructions.

Cloning of the TEX264-V5-pLX313 plasmids was performed using TEX264 sequences generated previously[29,100] including WT or TEX264 E194A (TBS*), F273A (LIR*), G280R, G282R, L284A (SHP*), I141A, S143A, W145A (SIM*) or S271A, S272A (P*). The pLX313-TP53-WT plasmid (Addgene) was used as the backbone for all the TEX264-V5-pLX313 plasmids. The backbone was digested by NHeI-HF and EcoRV-HF to remove TP53. TEX264 sequences were amplified by the Phusion Hot Start II High-Fidelity DNA Polymerase (Thermofisher) with primers (TEX-pLX313_Fwd and TEX-pLX313_Rev). NEBuilder® HiFi DNA Assembly Cloning Kit (NEB, E5520S) was used to ligate the TEX264 sequences into the pLX313 backbone according to the manufacturer's protocol. Sequencing of the correct insertion was performed using the EF1a_Fwd and WPRE_Rev primers (Invitrogen). All plasmids were sequenced by Source BioScience, Oxford, UK.

Zebrafish assays were performed using *tex264* complementation. Full-length *tex264-WT* was amplified with primers (tex264_F and tex264_R) from the cDNA of 2 days post fertilisation embryos and cloned into a pCS2+HisMyc expression vector (Addgene) using XhoI and XbaI restriction sites with the In-Fusion® Snap Assembly Master Mix (Takara Bio USA, Inc.). The *tex264*-pCS2+HisMyc plasmid was modified using the QuikChange Lightning Multi Site-Directed Mutagenesis Kit (Agilent) with the primer (tex264_F283A LIR mutagenesis) to create *tex264* F283A LIR* mutant. The plasmids were linearized using NotI and transcribed *in vitro* using the HiScribe SP6 RNA kit (NEB) together with the ARCA kit (NEB) to cap the resulting mRNA. The mRNA was purified with the Monarch® RNA cleanup kit (NEB) for subsequent injections.

Transfection and generation of stable cell

Transient plasmid transfections were performed using polyethylenimine (PEI) for biochemistry application or FuGENE® for microscopy usage, following the manufacturer's instructions. All siRNA transfections were carried out using Lipofectamine™ RNAiMAX, according to the manufacturer's protocol and assayed after 72 h.

Lentiviruses were produced by transfecting HEK-293T with the transfer plasmid containing the insert of interest flanked by the viral LTR and combined with the CMV-pAmphoR envelope and CMV-Δ8.2R packaging plasmids. Transfection was performed using PEI (ratio DNA:PEI; 3 μg:1 μl). Fifty hours after transfection, the virus-containing supernatant was collected and centrifuged at 1,000 x g to remove cells and filtered with 0.45 μm PVDF filters. A stable cell line was produced by seeding 500,000 cells in 6-well plates in 250 μl of DMEM with 10% FBS, 8 μg/mL polybrene and 750 μl of virus-containing media. Sixteen hours later, selection with antibiotics was started. After clonal expansion, clones obtained were tested for correct insertion by immunoblotting and immunofluorescence. The pLJC5-TMEM192-3xHA construct was used to produce cell lines stably expressing TMEM192-3xHA in HeLa, HCT116 and hTERT

RPE-1. The pLJC6-3XHA-TMEM192 construct was used for LysoIP in HeLa TEX264^{KO} as the cells were already puromycin resistant. To induce the depletion of ATG7, 1 μg/ml of doxycycline was added to the cell 4 days and again 2 days before the experiment. To induce the expression of p97- Myc/Strep, 1 μg/ml of doxycycline was added to the cell 24 hours prior to the experiment. Stable cell lines expressing TEX264 WT and the different mutants were generated in a TEX264^{KO} background and used for clonogenic assay and immunofluorescence experiments. Transient transfection with the same plasmids was used for LysoIP, with plasmid validation by immunoprecipitation and a representative image of the immunofluorescence experiment. LysoIP in freshly made TEX264^{KO} HeLa without complementation or transient siTEX264-depletion still displays TOP1 uptake in lysosomes. Once the cell settled after about 10 passages, TOP1 uptake was prevented.

Zebrafish model

The AB strain of zebrafish (Danio rerio) was obtained from the European Zebrafish Resource Centre (EZRC) in Karlsruhe, Germany, and its housing and care were carried out following ethical guidelines (EU Directive 86/609/EEC, Croatian Federal Act on Animal Protection) under project licence HR-POK-023. According to established protocols, the zebrafish were kept at 28°C and a 14-hour light and 10-hour dark cycle.[138] Zebrafish embryos of both gender were cultured in E3 media (5 mM NaCl, 0.17 mM KCl, 0.33 mM CaCl2, and 0.33 mM MgSO4) at the same temperature and light cycle until they reached 2 days post-fertilization (dpf). Before starting the experiments, the embryos were manually dechorionated. Phenotypes were observed and recorded at 6 hpf, 30 hpf and 48 hpf. Images were captured using a Samsung 13-megapixel camera with an f/1.9 aperture applied to the ocular of the binocular Motic SMZ-171.

MRC FOCUS trial

The transcriptome of 361 formalin-fixed paraffin-embedded primary resections from advanced colorectal cancer patients enrolled in the randomised controlled MRC FOCUS trial[139] were analysed. All data concerning the patients characteristics, consent, and study design are reported here.[139] Patients were required to have a colorectal adenocarcinoma diagnosis confirmed by histopathology, with inoperable metastatic or locoregional disease. These patients, starting first-line treatment with non-curative intent, were randomly assigned in the trial to either single agent 5-fluorouracil (given with levofolinate over 48 hours every two weeks – 286 patients) or 5-fluorouracil plus irinotecan (FOLFIRI – 75 patients) until progression. The study was registered as an International Standard Randomised trial (ISRCTN 79877428).

METHOD DETAILS

Total cell extract & immunoblot

For the total cell extract, cells were lysed using RIPA buffer supplemented with protease and phosphatase inhibitors and sonicated with a Bioruptor Plus sonicator (30 s ON, 30 s OFF for 10 cycles). The supernatant obtained from centrifugation at 21,000 x g for 15 min at 4°C was quantified with a BCA assay (ThermoFisher Scientific).

For immunoblot, samples were denatured by boiling for 5 min at 95 °C in Laemmli buffer, then separated by SDS-PAGE and transferred (wet transfer) to PVDF membrane. Membranes were blocked in 5% milk in TBS-T for 1 hour at room temperature. Membranes were incubated overnight with primary antibodies (5% BSA in TBS-T), washed three times with TBS-T and incubated with secondary antibodies coupled to HRP for 1 hour at room temperature. After three additional washes with TBS-T, membranes were detected with ECL-based chemiluminescence on the iBright imaging system. The immunoblot images were taken using the iBright system and contrast was adjusted using the iBright analysis software. The images presented correctly represent the original data. The contrast and brightness adjustment were equally applied to an entire membrane.

Isolation of proteins on nascent DNA – iPOND

iPOND was performed as described previously.[140] Briefly, HEK293T cells were synchronised by a single thymidine pulse for 17 hr, then released for 3 hr into the S phase. Approximately 100 million cells per condition were labelled with 10 μM EdU for 15 min or treated with Camptothecin (CPT) at 100 nM or 1 μM for 40 min and labelled with EdU for the final 20 min. A longer EdU pulse accounted for the reduced EdU incorporation rates in CPT-treated cells.[63] Cells were fixed with 1% formaldehyde for 20 min and quenched with 0.125 M glycine. After permeabilization with 0.25% Triton, the click reaction was performed at room temperature for 1 hr in a buffer containing 10 μM biotin azide, 10 mM sodium L-ascorbate and 2 mM CuSO4. For negative control samples, DMSO was used instead of biotin azide. Cells were then lysed in 1% SDS supplemented with phosphatase and protease inhibitors, and chromatin was fragmented into 50–300 bp fragments by sonication with a Bioruptor Pico sonicator (Diagenone, 30 s ON, 30 s OFF, 50 cycles). After centrifugation at 16,100 x g for 20 min, a 5% lysate volume was set aside as input. Biotin-labelled EdU was captured by incubating samples with streptavidin-coupled agarose beads (Novagen) for 16 hr. Beads were washed once with 1% SDS, once with 1 M NaCl and twice with NTN buffer (100 mM NaCl, 20 mM Tris HCl pH 7.4, 0.05% IGEPAL). Crosslink reversal and elution of immunoprecipitated proteins were achieved by heating beads in 2x Laemmli buffer at 95 °C for 5 min.

LysoIP

LysoIP was performed in HeLa expressing TMEM192-3×HA as described previously.[67] All conditions were treated with Bafilomycin A1 except for the proteomics analysis samples. For immunoblotting, 8 million cells of HeLa or HCT116 or 20 million cells of hTERT

RPE-1 were collected in KPBS (136 mM KCl, 10 mM KH2PO4, adjusted pH 7.25 with KOH). For the input, 2.5% of the cells were lysed for total cell extract analysis. Cells for LysoIP were homogenized with 20 strokes of a 2 ml homogenizer. The homogenate was then centrifuged at 1000 x g for 2 min at 4°C. The supernatant containing the cellular organelles, including lysosomes, was incubated with anti-HA magnetic beads on a rotator shaker for 15 min at 4 °C. Beads were washed four times in KPBS and eluted in 2 X Laemmli buffer, then boiled 10 min at 95 °C.

LysoIP – Mass Spectrometry and data analysis

Sample preparation

LysoIP was performed from 60 million HeLa cells per condition on four biological replicates. Lysosome content proteins (LysoIP) of non-treated and CPT-treated cells (50 nM for 6 hr) were obtained using 125 μl of beads per condition. Beads were washed 5 times and tubes containing the beads were changed twice. Elution was done in 60 μl Milli-Q water and sonication with the Bioruptor Plus sonicator (30 s ON, 30 s OFF for 10 cycles). 17% of the sample was used to assess the quality of the sample (immunoblotting and Coomassie staining), and the remaining 83% was digested using the S-Trap™ micro columns following manufacturer's protocol (ProTifi). Briefly, SDS was added to the samples (3% final concentration) before they were sequentially reduced with DTT (20 mM final concentration) and alkylated with Iodoacetamide (40 mM final concentration) for 30 min in the dark at room temperature. Samples were then acidified with phosphoric acid (1.2% final concentration) and proteins precipitated by adding 90% methanol in 100 mM TEAB buffer (1 to 7, sample: buffer ratio). Samples were loaded into the S-Trap™ micro-column cartridges and washed four times with 90% methanol in 100 mM TEAB buffer. One microgram of trypsin in 50 mM TEAB buffer was added into the S-Trap™ micro columns and incubated overnight at 37 °C. Finally, tryptic peptides were sequentially eluted from the S-Trap™ micro columns with 50 mM TEAB, 0.2% formic acid and 0.2% formic acid in 50% acetonitrile solution. Tryptic peptides were dried using a vacuum concentrator and reconstituted in 20 μl of 2% acetonitrile, 0.1% trifluoracetic acid.

LC_MS/MS

Peptides were analysed by reverse phase chromatography using a Vanquish Neo UHPLC system (operated in Trap and Elute mode) connected to an Orbitrap Ascend (Thermo Fisher Scientific). 1.5% of tryptic peptides were loaded onto a trap column (Acclaim™ PepMap™ 100 C18) and separated on a 50 cm-long EASY-Spray™ HPLC column using a 60 min linear gradient from 2% to 35% of buffer B (0.1% forsmic acid in acetonitrile) at 250 nl/min flow rate. Eluted peptides were then analysed on an Orbitrap Ascend operated in data-dependent mode, with advanced peak detection (APD) enabled. Survey scans were acquired in the Orbitrap at 120 k resolution over a m/z range of 400 -1500 and S-lens RF of 30. MS2 scans were obtained in the Ion trap (rapid scan mode) with a Quad isolation window of 1.6, 40% AGC target and a maximum injection time at auto, with HCD activation and 28% collision energy.

Data analysis

Mass spectrometry raw files were analysed in Fragpipe (v19.1) using the Label-Free Quantitation with Match Between Runs workflow (LFQ-MBR) with minor changes to the default settings. Briefly, data were searched against the reviewed human UniProt-Swissprot database (downloaded Jul 2022, containing 20386 sequences), selecting trypsin as proteolytic enzyme (maximum 2 missed cleavages), carbamidomethylation (C) as fixed modification and oxidation (M), acetylation (K, N-terminal) and phosphorylation (STY) as variable modifications. MS1 IonQuant was selected to calculate LFQ with MBR ion FDR at 1% and to report MaxLFQ. In addition, the top N ion was set up to 10 to get an iBAQ equivalent output. Fragpipe outputs were further analysed in Perseus (v1.6.2.2). In brief, the top 10N intensities were log 2-transformed, filtered by three valid numbers out of the four in at least one group and normalised by median subtraction. Missing values were then imputed (following the normal distribution). A two-sample student t-test combined with a Permutation – FDR correction (5%) was applied.

LysoIP-Seq

NGS sequencing of the DNA fragments purified by LysoIP was performed by GenScript for two biological replicates. After the capture of lysosomes by LysoIP from 40 million Hela cells, beads were washed four times in KPBS and eluted in 50 mM Tris pH 7.4, 150 mM NaCl and 0.2% Triton. For Picogreen quantification, samples were digested with proteinase K for 1 hr at 55 °C before quantification according to the manufacturer protocol. For the library preparation, samples were denatured at 95 °C to convert (ds)DNA into (ss) DNA. Adapters were added to both ends of the ssDNA fragments using the T4 polynucleotide kinase and the T4 ligase. Subsequently, a digestion enzyme was used to remove excess adapters, adapter dimers and unligated ssDNA samples. PCR amplification of the library was performed by the KAPA HiFi HotStart (Roche). The library was sequenced on the Illumina NovaSeq platform.

Data analysis was performed using Trimmomatic, to remove adapters and low-quality reads, Pandaseq, to merge the clean data, and BWA-MEM, to align the merge sequence to Hg38 reference genome. Samtools was used to extract the Mitochondrial DNA and Nuclear DNA mapping reads and assess the enrichment in centromeric regions. Genome distributions were obtained using the Homer annotates peaks tool. The bedtool multiple intersection was used to identify overlapping picks in the sequencing data, and the Venn diagram was produced using Eulerr online tool. Bigwig files were generated for visualisation in the Genomic browser IGV.

Whole genome sequencing

Genomic extraction was performed in HeLa WT or TEX264^{KO}, either untreated or treated with 10 nM CPT for 7 days continuously. Treatment was changed every 48 hr, and cells were split on day 5 to avoid overconfluency. When collected, a fraction was kept for immunoblotting. After harvesting, genomic DNA was purified using the Genomic DNA Buffer Set (Qiagen).

Whole genome sequencing was performed GenScript. Genomic DNA quality was assessed using a Qubit® 3.0 Fluorometer. Whole genome DNA libraries were prepared using Hieff NGS® OnePot Pro DNA Library Prep Kit V2 (Yeasen) and VAHTS Dual UMI UDI Adapters Set 1 – Set 4 for Illumina (Vazyme). The quality of the libraries produced was controlled using Qsep 100 Analyzer (BiOptic Inc.) and Qubit® 3.0 Fluorometer. Each genome DNA library was sequenced using 150bp paired end reads on the Illumina NovaSeq6000 platform. All samples satisfied the minimum 150G data with an average 50x coverage. Quality control on raw Illumina fastq reads was done to detect contamination and assess the quality of reads. Reads were cleaned by removing low-quality reads and adapters using Trimmomatic (v0.3). Somatic variant calling was carried out using the Sarek workflow[141] v3.3.2, with reads aligned using BWA-MEM v0.7.17-r1188 and single base substitutions (SBS) called using Mutect2[142] v4.4.0.0 and Strelka[143] v2.9.10. SBS mutational signatures were assigned based on the union of Mutect2 and Strelka variant calls, using SigProfilerAssignment[144] v0.0.31 against COSMIC[145] signatures set v3.3.

Immunofluorescence

For standard immunofluorescence, cells were fixed in 4% formaldehyde in PBS for 15 min at room temperature. Then washed with PBS and permeabilised in 0.5% Triton X-100 in PBS for 15 min at 4 °C. After blocking in 5% BSA/PBS for 1 hr at 37 °C, cells were incubated with primary antibody (1:250) diluted in 2.5% BSA/PBS solution for 1 hr at room temperature. Then, coverslips were washed with PBS and incubated with secondary antibodies (1:500) and DAPI (1:500) for 1 hr at room temperature. Coverslips were mounted onto slides using Fluoromount G (ThermoFisher). Images were taken using a Zeiss 710 LSM microscope utilising a Plan-apochromat 63 x lens with a 1.4 NA and oil immersion. Images were collected sequentially to avoid any overlap between dyes, ensuring the same MBS filterset was maintained for all acquisitions. Images were gathered in 1024 x 1024-pixel format at approximately 55% Nyquist sampling, with full Nyquist sampling not being appropriate for this experiment. Images were acquired at 12-bit with 4x averaging being utilised to help with spurious noise within the images. Analysis was carried out using ImageJ Fiji and CellProfiler.

For imaging the reporter mCherry-TOP1-GFP protein, cell were transfected transiently and seeded on coverslips. After treatment, cell were fixed in PBS containing 2% FBS, 3.2% formaldehyde. Then stained with DAPI, mount and imaged as standard.

For imaging of the protein aggregates, cells were fixed in 4% formaldehyde, permeabilised in 0.5% Triton X-100 and 3 mM EDTA in PBS for 15 min at 4 °C. Blocking was performed in 5% BSA, 3 mM EDTA in PBS for 1 hr at 37 °C. EDTA was used to avoid staining of membranes, nuclei or lipid droplets.[82] Staining with Proteostat at 1:2,000 diluted in 2.5% BSA in PBS was done in the dark for 1 hr. Then, the dye was washed five times with 0.1% BSA, 0.2% Tween and 0.3 mM EDTA in PBS and twice with PBS only. Cells were incubated with primary and secondary antibodies and DAPI as described for standard immunofluorescence if needed. Imaging of the Proteostat dye was done using the Rhodamine settings as standard.

For imaging of TOP1cc foci, the protocol was previously described.[69] Briefly, cells were fixed in 4% formaldehyde, permeabilised in 0.5% Triton X-100, and blocked with 5% BSA/PBS for 1 hr at 37 °C. To render the DNA-protein crosslinks more accessible to the antibody, the coverslips wee incubated in 1% SDS/PBS at RT for 5 min. Then washed five times with wash buffer (0.1% BSA, 0.1% Triton X-100 in PBS) and twice with PBS. Incubation with TOP1cc primary antibody in 2.5% BSA/PBS was performed for 1 hr at RT. Before subsequent incubation, cells were washed once with a wash buffer for 3 minutes with gentle shaking and twice with PBS. Cells were incubated with another primary antibody if needed, then secondary antibodies, DAPI, and imaged as described for standard immunofluorescence.

For imaging of Anaphase Ultrafine Bridge (UFB), cells were fixed and permeabilised with the UFB pre-extraction/fixation buffer (4% PFA in 20 mM PIPES at pH 6.8, 1 mM MgCl2, 10 mM EGTA, and 0.2% Triton X-100) for 10 minutes at room temperature and washed with PBS containing 0.2% Triton for 5 minutes before being blocked with blocking buffer. Primary antibodies were incubated overnight and then washed using 0.2% Triton in PBS three times. After 2 hours of incubation with secondary antibodies, coverslips were washed with 0.2% Triton in PBS three times before being mounted onto a glass slide using VECTASHIELD antifade mounting medium (Eurobio Scientific) supplemented with 5 μg/ml DAPI.

Pre-extraction was used to better visualise γ-H2AX and 53BP1 foci in the experiment with TEX264^{KO} and ATR inhibition. Before fixation, cells were washed with ice-cold PBS and incubated with pre-extraction buffer on ice for 2 min (HEPES 25 mM pH 7.4, 50 mM NaCl, 1 mM EDTA, 3 mM MgCl2, 0.5% Triton X-100). Then, it was washed in a pre-extraction buffer without Triton for 2 minutes on ice before fixation. Images were taken using the Leica DMi8 SP8 FALCON (see below).

Proximity Ligation Assay

Proximity ligation assay was performed according to the manufacturer's protocol of the Duolink® In Situ PLA® kits (Sigma-Aldrich). HeLa cells stably expressing V5-tagged TEX264-WT were transfected with LC3-pEGFP-C2 for 24 hours before fixing and permeabilising as described for standard immunofluorescence. After blocking in the provided blocking reagent, coverslips were washed with wash buffer A (150 mM NaCl, 10 mM Tris pH 7.4, 0.05% Tween 20) before incubation with anti-GFP and anti-V5 primary antibodies (dilution 1:500). After 3 washes in buffer A, coverslips were incubated with PLA PLUS and MINUS probes. Coverslips were incubated with ligase followed by polymerase, with washes in buffer A between each step. Coverslips were washed twice for 10 minutes with wash buffer B (100 mM NaCl, 250 mM Tris pH 7.5) before staining with DAPI (1:1000) for 10 minutes. Finally, coverslips were washed twice with buffer A and once with 0.01 x buffer B before mounting using ProLong™ Glass Antifade Mountant (Invitrogen). Images were taken using the Leica DMi8 SP8 FALCON laser scanning confocal microscope with a 63x lens with a 1.2 NA water immersion

objective lens and a confocal pinhole size set to 111.4 μm. Images were acquired in 2048 x 2048-pixel format at 8-bit with a pixel size of 90nm. Analysis was carried out using ImageJ and CellProfiler.

Alkaline Comet Assay

Around 50,000 cells per condition were collected with Trypsin and resuspended in PBS 1% low melting point agarose (BioRad). Cell were added on slides already prepared with dried 1% agarose and lysed in lysis buffer (2.5 M NaCl, 100 mM EDTA, 10 mM Tris–HCl at pH 10.5, 1% DMSO and 1% Triton X-100) overnight at 4 °C. DNA denaturation was performed in electrophoresis buffer (300 mM NaOH, 1 mM EDTA, 1% DMSO, pH > 13) for 30 min at 4 °C. Then electrophoresis was performed for 25 min at 25 V. Neutralisation was performed with 500 mM Tris–HCl, pH 8 for 5 min twice and staining with SYBR™ Gold Nucleic Acid Gel Stain (1:10 000, Invitrogen) for 30 min. Images were acquired using a Nikon Ni-E (Nikon, Japan) microscope utilising an Andor Zyla 4.2 Plus sCMOS camera (Oxford Instruments, United Kingdom) and a CoolLED PE-4000 light source (CoolLED, United Kingdom). For comet assay images a 10x magnification with 0.45 NA Plan Apo Lamba objective lens (Nikon, Japan) was used. Images were acquired using the standard FITC Nikon filter set with excitation set to 10% on the 470 nm line. The camera was exposed for 6 ms at gain 4 to allow a 12-bit image to be acquired. Olive moment was obtained using the OpenComet plugin on ImageJ software.

Live cell microscopy

Live imaging of the Lamin A/C -GFP assay was performed using the custom-made spinning disc confocal setup based on the UltraVIEW VoX (Perkin Elmer, Waltham, Massachusetts, USA) with the scan head (CSU-X1, Yokogawa) and a Nikon Eclipse Ti-E microscope with a Plan APO oILED PE-4000 li DIC N2 ∞ / 0,17 WD 0.13 OFN 25 and APO TIRF 100x / 1.49 DIC N2 ∞ / 0,13-0,20 WD 0.12 objectives. The illumination was provided by a diode pumped solid state 488nm/50mW laser diode and a cobalt solid state 561nm/50mW laser diode. 405/488/561/640 dichroic mirror and multi-color channels were used, and images were acquired using an EMCCD iXon897 camera (Andor Technologies) and Volocity software (Improvision) every 20 s. Bleaching correction and rendering were done using ImageJ and the package TrackMate.

Live imaging of the reporter mCherry-TOP1-GFP assay was performed using an Olympus/Evident SpinSR SoRa spinning disc with Yokogawa CSU-W1 in spinning disc mode (50 μm pinhole disc). Imaging was carried out using a 60 x 1.3 NA silicone oil objective. Detection was carried out in dual camera mode with 2x Hamamatsu ORCA Fusion BT cameras set to 480 MHz read speed. A 561 LP dichroic mirror sent blue/green emission light to camera 2 and red/far-red emission to camera 1. The channel combinations were designed in 2 groups. Chanel group 1 was used at 561 nm 3% laser with only camera 1 at a 617/73 nm filter and 30 ms exposure. Chanel group 2 was used at 640 nm 3% laser and 488 nm 3% laser with camera 1 at a filter of 685/40 nm and 30 ms exposure and camera 2 at a filter of 525/50 nm and 30 ms exposure. Seven Z sections were captured at 0.4 μm spacing every across 5 independent xy positions every 20 s for 2 hr. A humidified 5% CO2 atmosphere and 37 °C temperature control ensured sample viability. Post-acquisition images were deconvolved using Evident/Olympus Cellense constrained iterative deconvolution using an advanced maximum likelihood algorithm with 5 processing iterations. The included adaptive PSF was used, and noise reduction was applied. Images and videos displayed are single z-slices. Repeats of the live imaging of the reporter mCherry-TOP1-GFP assay were performed using the custom-made confocal spinning disc.

Electron Microscopy

Cells were fixed in 2.5% glutaraldehyde and 4% PFA in 0.1 M PIPES buffer and embedded using the modified NCMIR Method for Serial Block Face SEM sample preparation.[146] Following embedding, the blocks were sectioned (90 nm sections on 200 mesh Cu grids) and were imaged without further staining using a JEOL 1400 TEM operated at 120 kV with a Gatan Rio CMOS camera for a first check. The tip of the resin block containing the cell was then sawed off and remounted onto a 3View pin using conductive epoxy glue and polymerised overnight. The surface was then polished using a diamond knife and sputter coated with ~15 nm gold/palladium. Volume EM datasets were acquired using a Zeiss Merlin Compact SEM fitted with a Gatan 3View system and OnPoint Detector. The parameters were 1.8 kV accelerating voltage, 30 μm aperture, and Focal Charge Compensation at 100%. The voxel size is 7.7 nm (x) x 7.7 nm (y) x 100 nm (z). At least 740 slices were acquired for each dataset. Manual characterisation and quantification of the blister-like structure were done using ImageJ. Further segmentation and 3D rendering of the volume EM was done using Arivis Vision 4D. $STX17^{KD}$ were validated using a LEO 912AB transmission electron microscope with an Omega energy filter operated at 120 kV.

To preserve membrane and structure integrity, growing cells were fixed using high-pressure freezing fixation. Cells attached to 3 mm coverslips were put in a small volume of cryoprotectant solution (20% BSA in PIPES buffer) and high-pressure frozen using a Leica EM ICE. Frozen samples were then transferred under liquid nitrogen to a Leica EM AFS2 freeze substitution unit and processed as described[147] with the following alterations: the freeze substitution medium was 0.2% Uranyl acetate and 5% water in acetone, the resin used was Lowicryl HM20 Monostep (PolySciences) and the UV polymerisation schedule was 24 hr at - 45 °C, warm to 0 °C over 12 hr, then 36 hr at 0 °C. 90 nm sections were transferred to 50 mesh formvar-coated Cu grids and post-stained for 5 min with Reynolds lead citrate, washed and air dried, and then imaged on the JEOL 1400 TEM as above.

Cryo-Focused Ion Beam (FIB) milling

Quantifoil™ R 2/2 on 200 gold mesh grids (Jenna Bioscience) were glow discharged at air atmosphere for 45s on high power using a Harrick plasma cleaner. The grids were then immersed in a solution of fibronectin at 20 ng/ml, deposited in a 6-well plate and incubated in a droplet of fibronectin for an extra 30 min. Grids were washed twice with PBS, and 300 000 HeLa cells in media were added on top of the grids and left overnight. Cells were incubated with 50 nM of LysoTracker™ Deep Red (Thermo Fisher Scientific) for 2 hr, then treated with 50 nM CPT for 25 to 35 min before fixing by being plunge frozen using a Leica GP2. Vitrified grids were then clipped into autogrids and subsequently stored under liquid nitrogen.

Autogrid-clipped TEM grids were inserted into a cassette and loaded into the Plasma FIB Arctis microscope (Thermo Fisher Scientific). Identification of lamella sites and milling was then carried out using webUI (Sagio Development LLC). Briefly, an SEM tile set of the grid was used to identify cells suitable for milling. A reflection and far-red fluorescent z-stack were acquired for each identified cell using the in-chamber fluorescent microscope across a +/- 7.5 μm distance from the focus position in 0.5 μm increments. The fluorescent z-stack was used to guide the position of the lamella template. The grid was then coated with organo-platinum using the gas injection system (GIS) for 50 and then sputter coated with platinum metal for 120. For each site, electron centring of the fluorescent target, followed by eucentric height and milling angle search (12° target), was performed before positioning a 15 μm width lamella milling template. Milling was performed at 30 kV using Argon gas to generate plasma and a targeted final lamella thickness of 150 nm. For each site, stress relief cuts away on each side of the intended lamella were first milled using a 0.74 nA ion beam followed by three milling steps at 0.74 nA, 0.2 nA and 60 pA to obtain a ∼400 nm thick lamella. Once all three milling steps had been completed for all the lamella sites, these thicker lamellae were successively "polished" using 20 pA down to a nominal software target thickness of 150 nm. A final reflection and far-red fluorescent z-stack was acquired using the in-chamber fluorescent microscope across a +/- 7.5 μm distance from the focus position, in 0.5 μm increment for each of the polished lamellas followed by 5 s sputter coating with platinum metal before retrieving the autogrid into the cassette.

Grids were directly moved from the Arctis into the Titan Krios for data collection. Cryogenic electron tomography (cryo-ET) data were acquired on a G3i Titan Krios equipped with a Falcon 4i and Selectris-X energy filter. The PACEtomo_targetsFromMontage.py script[148] was used in SerialEM to add targets from medium mag montages acquired at 15,000x magnification. The PACEtomo_measureOffset.py script[148] was used to measure and calculate the tilt axis offset value optimized for the z-movement of the sample. For the correlation, medium magnification montages were saved as single images and imported into MAPS for manual correlation. After the setup, the PACEtomo.py script[148] was run to collect selected targets in parallel, with beam tilt compensation. A dose-symmetrical tilt scheme covering the +/- 54° range with 3° increments starting at a -12 degrees tilt angle to compensate for the lamellae pretilt was used. Tilt-series were recorded at a nominal magnification of 42.000x, resulting in a pixel size of 2.95 Å, with 3.36 e-/Å2 per tilt, across 8 frames, leading to a total dose of 121 $e^-/Å^2$.

Data were pre-processed using RELION, MRC files were motion-corrected using the RELION motion correction algorithm, half maps were created for downstream denoising, and CTF was estimated with CTFFIND4. Tomograms for initial visualization were reconstructed using automated reconstruction in AreTomo, while reconstructions from RELION were used for denoising using CARE. Membrane segmentation was carried out on denoised tomograms using the standard Membrain-Seg protocol.[149] Segmentations were trimmed using IMOD before visualisation in ArtiaX in ChimeraX.

Rapid approach to DNA adducts recovery – RADAR

A modified RADAR assay was used to assess the level of TOP1cc.[72] Around 20 million HeLa cells were lysed in M buffer (6 M guanidine thiocyanate, 10 mM Tris–HCl pH 6.8, 20 mM EDTA, 4% Triton X-100, 1% N-lauroylsarcosine and 1% dithiothreitol). DNA was precipitated by adding 100% ethanol, then washed three times in DNA wash buffer (20 mM Tris–HCl pH 7.4, 50 mM NaCl, 1 mM EDTA, and 50% ethanol), and solubilised in 8 mM NaOH. DNA concentrations were quantified by Picogreen and confirmed by slot blot analysis on a Hybond N + membrane, followed by detection with an anti-(ds)DNA antibody. For TOP1cc, samples were digested with 100 U/mL of Benzonase nuclease for 30 min at 37 °C and analysed by slot blotting on a Nitrocellulose membrane.

Isolation and detection of TOP1cc from zebrafish embryos was performed using a modified RADAR protocol[118] optimised for zebrafish embryos. DPCs were isolated from wild-type (WT) and *tex264*-silenced embryos at two days post fertilisation, as well as embryos overexpressing recombinant zebrafish *tex264*-WT or *tex264*-LIR mutant (30 embryos per condition were used for isolation). The main change from previously published RADAR isolations was snap-freezing the samples in liquid nitrogen and overnight lyophilization using a FreeZone 2.5 lyophilizer (Labconco, USA) instead of TCA precipitation. DPC isolates were dissolved in 50 μL of SDS loading buffer (4 M urea, 62.5 mM Tris-HCl (pH 6.8), 1 mM EDTA, and 2% SDS). For the detection of TOP1cc, an equivalent of 1-2 μg of DNA-normalized DPCs were dissolved in 200 μL TBST buffer (10 mM Tris-HCl (pH 7.5), 15 mM NaCl, 0.02% Tween 20), and applied to a nitrocellulose membrane using the vacuum aspiration and dot blot system (Bio-Dot Microfiltration System, BioRad). To validate the DNA quantifications, dot blot analysis was performed using a nylon membrane (RPN303B, GE Healthcare). 2 ng of DNA was applied to the nylon membrane, and DNA was detected with an anti-(ds)DNA antibody.

Biochemical purification of protein aggregates

The isolation of aggregates was adapted from a protocol previously described.[150] Briefly, 8 million HeLa cells were treated for 12 hr. Lysis was performed using 50 mM Tris-Cl (pH 8), 150 mM NaCl, 0.2% Triton X-100 and 100 U/mL of Benzonase nuclease for 30 min with shaking at 4 °C. Centrifugation was conducted at 21,000 x g for 30 min at 4 °C. Supernatant was collected and used as the

soluble fraction. The pellet was washed twice with 1.5% SDS in 50 mM Tris-Cl (pH 8) and 150 mM NaCl and centrifuged at 21,000 x g for 30 min at 16 °C. A higher temperature was used to avoid SDS precipitation. The supernatant was collected and used as the SDS soluble fraction. The final pellet was solubilised in 100% formic acid by sonication with a Bioruptor Plus sonicator (30 s ON, 30 s OFF for 10 cycles). After at least 3 hr at RT, samples were centrifuged at 1,000 x g for 2 min, and then formic acid was evaporated using a Concentrator 5301 (Eppendorf) at 60 °C for approximately 30 min. Once dried, the pellet was resuspended in water and 5 X Laemmli buffer. The pH was adjusted using 7.5 μl of 2 M Tris Base.

Immunoprecipitation

TEX264^{KO} HeLa cells transiently transfected with WT or TEX264 mutants were seeded at 20 million cells per condition. Doxycycline-inducible HEK293 Flp-In TRex cells expressing p97-Myc/Strep were seeded at 20 million cells per condition. When indicated, cells were synchronised in the S phase by a single Thymidine pulse for 17 hr, followed by a 3-hr released step. Cells were lysed in IP lysis buffer (50 mM Tris, pH 7.4, 150 mM NaCl, 1 mM EDTA, 0.2% Triton X-100, supplemented with protease and phosphatase inhibitors) and incubated on a rotator at 4 °C for 10 min. Chromatin was then pelleted by centrifugation for 5 min at 1000 x g and then digested with 100 U/mL Benzonase in Benzonase buffer (2 mM MgCl2, 50 mM Tris, pH 7.4, 150 mM NaCl). A fraction of the lysates representing 1% of the elution was taken for the input. For recombinant TEX264-V5 or p97-Strep IP, lysates were supplemented with ethidium bromide (50 μg/mL) and incubated with anti-V5 agarose beads (ChromoTek) or anti-Strep-Tactin® Sepharose® resin (iba LifeSciences) for 2 hr on a rotator at 4 °C, washed four times with IP wash buffer (150 mM NaCl, 50 mM Tris–HCl, 0.06% Triton X-100), and resuspended in 2 X Laemmli buffer. For endogenous TEX264 IP, the lysates were incubated with 5 μg of TEX264 or IgG control antibodies (both homemade) for 2 hours on a rotator at 4 °. Then, the lysates and antibodies mix was incubated with Protein A magnetic beads (New England BioLabs) overnight on a rotator at 4 °C, washed and eluted as previously described.

Clonogenic assay

For the S-phase study, cells were seeded at 1,000 HeLa cells per well and synchronised by a single Thymidine pulse for 16 hr, then released for 3 hr into S-phase. Cells were then treated with the indicated autophagy drug and indicated doses of CPT for 6 hr. For the study comparing TEX264^{KO} to RNF4 inactivation, all cell lines used were seeded 72 hr after RNF4 siRNA depletion for both low- and high-dose CPT treatment at the same time. Low-dose CPT study was treated for 8 hr with the indicated doses of CPT (nM), and high-dose CPT study for 45 min (μM). For the study of TEX264 mutant, stable cell lines expressing the WT or the mutant TEX264 were treated for 8 hr with the indicated doses of CPT. Seven days after treatment, colonies were fixed in 100% methanol for 10 min and stained using 0.5% crystal violet and 20% methanol for 10 min. The number of colonies was counted using the automated GelCount colony counter (Oxford Optronix). The surviving fraction was determined by normalizing the number of colonies in each condition to the CPT-untreated control. All experiments were conducted in triplicate across technical replicates.

Cell Viability Assay

Cells were seeded in 96-well plates (3,000 cells/well), synchronised by a single Thymidine pulse for 20 hr, and then released for 3 hr into the S phase. Treatment was performed for 48 hr with indicated doses of CPT. Cell viability was measured using the resazurin assay 4 hr after adding 30 μg/ml of resazurin (Sigma-Aldrich) to the cell. Reading was done using a microplate reader (BMG LABTECH CLARIOstar Plus,Serial no. 430-3000) excitation at 560-15 nm and emission at 590-20 nm.

Zebrafish assay

To silence zebrafish *tex264* (ENSDARG00000092154), a specific antisense morpholino oligonucleotide (tex264MO-splice) was designed to bind to the exon1 – intron 1 boundary,[151] thereby preventing splicing. Another *tex264* morpholino was designed to inhibit translation (tex264MO-ATG) and was combined with the splice morpholino. To verify the specificity of the *tex264* morpholino, we performed rescue experiments by co-injecting *tex264*MO and mRNA encoding the full-length coding sequence of either WT *tex264* or mutant *tex264* (LIR mutation, F283A) into embryos at the 1-4 cell stage. Zebrafish embryos were injected with a 1 nl injection mix between the one and the four-cell stage. The injection mix contained splice MO (100 μM), ATG-MO (100 μM), mRNA (250ng/ul) and 0,02 % phenol red in 300 mM KCl solution.

RNA isolation from zebrafish embryos was performed using the Monarch Total RNA Miniprep Kit (NEB). At two days post-fertilisation (dpf), five embryos per condition were collected and pooled to measure *tex264* expression levels. Reverse transcription was performed with the ProtoScript II First Strand cDNA Synthesis Kit (NEB) using random primer and oligo-dT primer mix, according to the manufacturer's instructions. Analysis of RT-qPCR was performed using GoTaq qPCR mix (Promega), and primer pairs were designed to span exon-exon boundaries, thus ensuring specific amplification without interference with genomic DNA. Normalisation was done using the housekeeping gene *atp50* (ENSDARG00000001788). Quantification was performed using the Qgene method.[152] Gene expression levels were calculated as Mean Normalized Expression (MNE) as previously described.[153]

MRC FOCUS trial analysis

The transcriptome of the primary resections from advanced colorectal cancer patients enrolled in the MRC FOCUS trial[139] were analysed. Samples were profiled as part of the S:CORT consortium by Xcel microarray (Almac). The control arm of the MRC FOCUS transcriptome is publicly available in GEO as part of GSE156915,[119] while the FOLFIRI arm was profiled at a later stage. CEL files

from both arms underwent robust multiarray average normalization with the 'affy' R package,[154] and batch effects were corrected at the probeset level by ComBat with the 'sva' R package. TEX264 expression was represented by one single probeset (ADXEC.3184.C1_s_at).

The primary endpoint was progression-free survival (PFS) censored at 15 months as previously done[119] and agreed by the investigators prior to any inspection of the data or analyses. This endpoint is biologically relevant and spans the timeframe of differential effects of first-line FOLFIRI on survival. Tumour assessment was done at baseline ($\leq$4 weeks before treatment), then every 12 weeks, with either CT or MRI, and scored according to RECIST 1.0. criteria.

Patients were divided into two groups, TEX264 high and TEX264 low, according to the median of their TEX264 RNA expression. Kaplan-Meier curves were produced according to the treatment received by the patients, either 5-fluorouracil alone or FOLFIRI. Univariate Cox regression determined hazard ratios (HR), confidence intervals (95% CI) and p-values with no addition of confounding factors. Interaction analysis between TEX264 vs Treatments (FOLFIRI/5-Fluorouracil) was also performed, providing a significant p-value.

QUANTIFICATION AND STATISTICAL ANALYSIS

Experiments were conducted in at least two biological replicates (n) and statistical analysis was performed using Prism 10 (GraphPad Software); significance is labelled as follows * $p < 0.05$; ** $p < 0.005$; *** $p < 0.0005$; ns, not significant. Statistical tests, biological replicates and details of the experiment can be found in the figure legend. Error bars are displayed as standard deviation (SD), unless stated otherwise in figure legend. Normality (Gaussian) distribution was tested using the Shapiro-Wilk test to determine whether the data met the assumptions of the statistical approach used (Ordinary Two-way ANOVA with main effect only and Dunnett's multiple comparisons tests, with a single pool variance).

ADDITIONAL RESOURCES

Published mass spectrometry proteomics was obtained from the ProteomeXchange Consortium via the PRIDE: PXD018092 and PRIDE: PXD011727 (Nakamura et al.[63] and Srivastava et al.[66]) and from the source data of the publications (Dungrawala et al.[64] and Ribeyre et al.[65]). All proteins found by proteomics were compared to a list of known autophagy-related proteins created from the human UniProt-Swissprot database, the Gene Ontology (GO) database and the Kyoto Encyclopedia of Genes and Genomes (KEGG) database. Category identification for the 277 autophagy proteins identified by IPOND proteomics was done manually. Ridge regression plot was performed using Anaconda with Python packages. Published ChIP–seq data were obtained from the Gene Expression Omnibus database for TOP1cc and TOP1 under accession numbers NCBI: GSE135808 and NCBI: GSE57628 (Tan et al.[88] and Baranello et al.[87]). TEX264 structure was predicted by AlphaFold.

CellPress
OPEN ACCESS

Supplemental figures

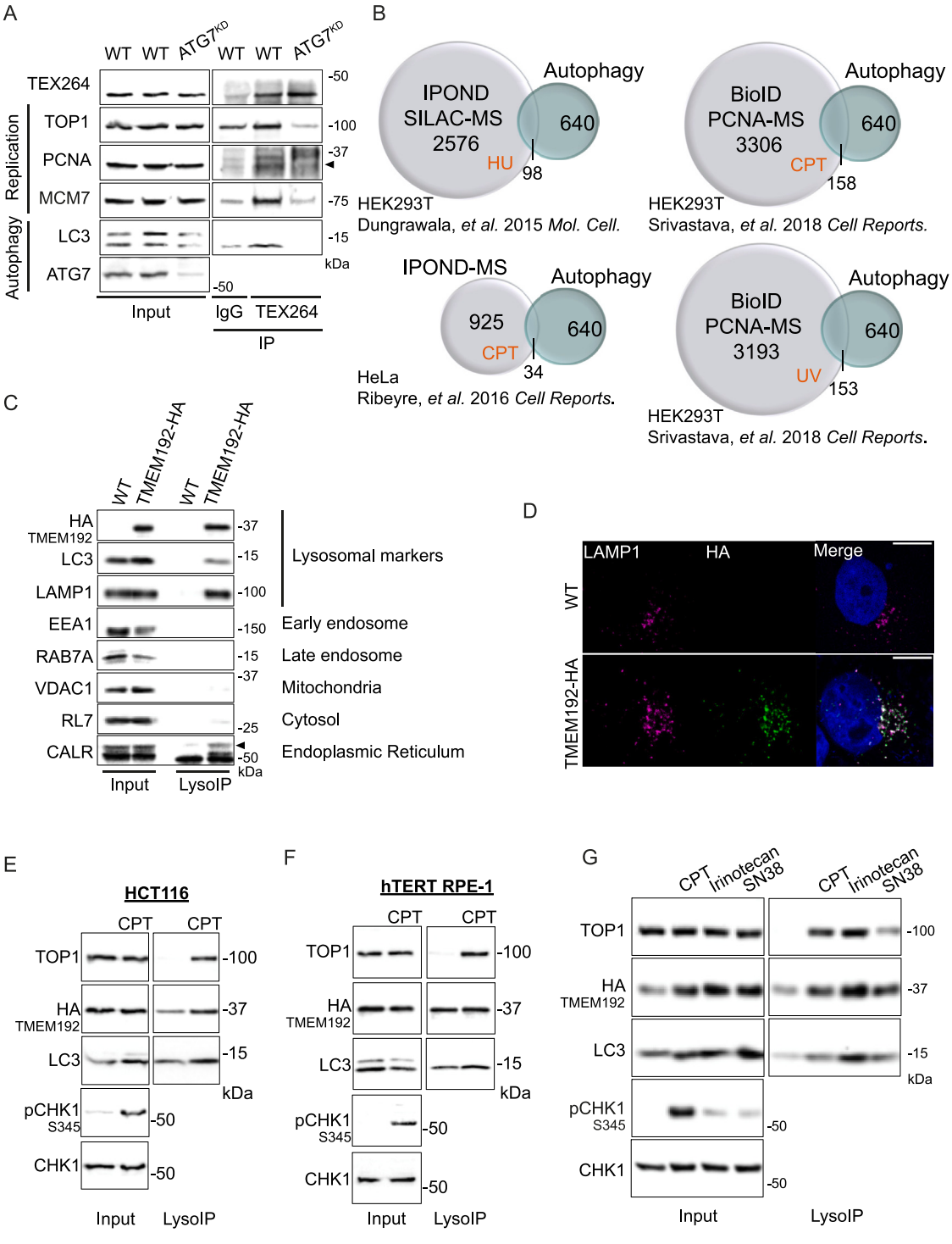

(legend on next page)

Figure S1. Autophagy recruitment at stalled replication forks promotes TOP1cc degradation, related to Figure 1 and Table S1

(A) Co-immunoprecipitation of endogenous TEX264 in WT cells or in the context of ATG7 depletion ($n = 2$). Unspecific immunoglobulin G (IgG) was used instead of TEX264 antibody as a control.

(B) Overlap of the protein set identified by immunoprecipitation of replication forks interactome by MS[64–66] and known autophagy-related proteins from the human UniProt-Swissprot database, the Gene Ontology (GO) database, and the Kyoto Encyclopedia of Genes and Genomes (KEGG) database. Replisomes were identified by iPOND, or Bio-ID of PCNA, in different cell lines after treatment with different replication stress inducers. HU, hydroxyurea; UV, ultraviolet.

(C) LysoIP was performed in HeLa WT or cells modified for LysoIP experiments by expression of the resident lysosomal tagged protein TMEM192-HA ($n = 3$). The LysoIP cell line allows the specific pull-down of lysosome vesicles without contamination from other cellular organelles.

(D) Immunofluorescence of HeLa WT cells and TMEM192-HA cells used for LysoIP, using anti-HA antibody and anti-LAMP1 marker of the late endosome and lysosome vesicles ($n = 3$). Scale bar, 10 μm.

(E) LysoIP performed after 6 h of treatment with 50 nM CPT in S-phase-synchronized HCT116 cells ($n = 3$). All conditions were treated with 50 nM BAF.

(F) LysoIP performed after 6 h of treatment with 50 nM CPT in S-phase-synchronized cells in hTERT RPE-1 ($n = 3$). All conditions were treated with 50 nM BAF.

(G) LysoIP performed in HeLa released from a single thymidine block into the S-phase and treated for 3 h with 50 nM CPT, 5 μM irinotecan, or 50 nM SN38 ($n = 3$). All conditions are treated with 50 nM BAF.

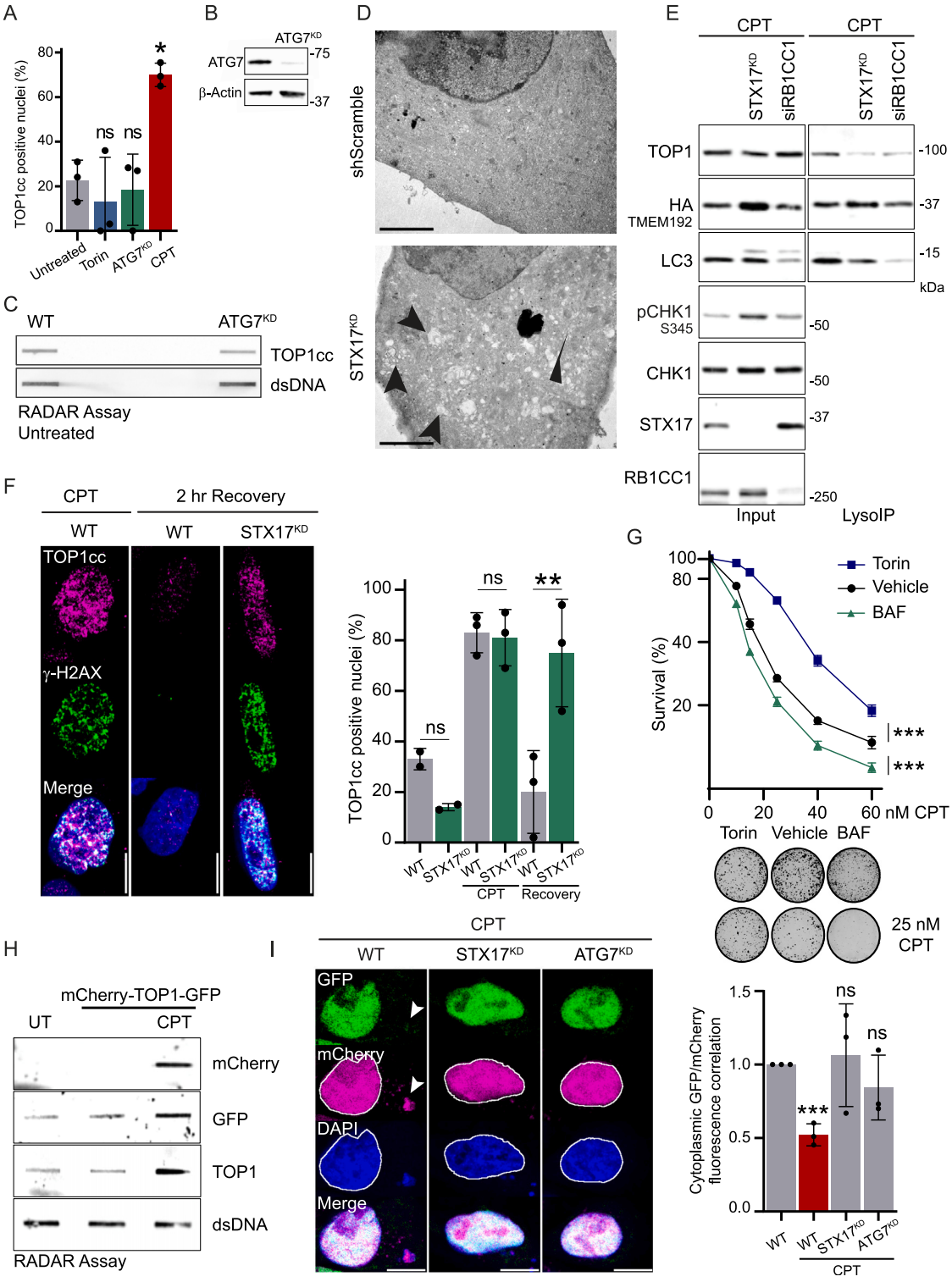

Figure S2. Autophagy regulates TOP1 degradation to promote DNA damage repair and cell survival, related to Figure 2

(A) Immunofluorescence of TOP1cc foci in WT cells, after induction of shATG7 (ATG7^{KD}), 4 h of treatment with 250 nM Torin, or 2 h of treatment with 50 nM CPT. Quantification of positive nuclei for TOP1cc foci (n = 3). Two-way ANOVA, error bar, SD; comparison against untreated.

(B) Immunoblot showing ATG7 depletion in cells used for immunofluorescence and RADAR.

(C) RADAR assay to assess TOP1cc level in WT and ATG7^{KD} cells unchallenged (n = 2). Double-stranded (ds) DNA is used as a loading control.

(legend continued on next page)

(D) Electron microscopy images of HeLa cells transformed with scrambled short hairpin RNA (shRNA; control) and STX17 shRNA. STX17^{KD} presents an accumulation of double-membrane structures, labeled with arrows.
(E) LysoIP was performed in HeLa WT or STX17^{KD}, and cells were depleted for RB1CC1 (FIP200) using small interfering RNA (siRNA). Cells were released from a single thymidine block into S-phase and treated with 50 nM CPT and 50 nM BAF for 5 h (n = 3).
(F) Immunofluorescence of TOP1cc foci in WT cells or in STX17^{KD} untreated, after 2 h of treatment with 50 nM CPT and after 2 h recovery from CPT treatment. Scale bar, 10 μm. Quantification of positive nuclei for TOP1cc foci (n = 3). Two-way ANOVA. Error bar, SD.
(G) Quantification of clonogenic assay of S-phase-synchronized cell treated for 6 h with CPT and either 150 nM Torin-1 or 50 nM BAF (n = 3). Error bar represents mean ± SEM. Two-way ANOVA on the area under the curve. Representative images of untreated or 25 nM CPT colonies obtained by clonogenic assay.
(H) RADAR assay to assess the accumulation of TOP1cc when TOP1 is fused to GFP and mCherry after 1 h of 100 nM CPT (n = 2). Double-stranded (ds) DNA is used as a loading control. UT, untransfected untreated condition.
(I) Imaging of the reporter mCherry-TOP1-GFP after 3 h of treatment with 50 nM CPT (nM) in WT cells, STX17^{KD}, or ATG7^{KD} (n = 3). Scale bar, 10 μm. Quantification of the correlation between GFP and mCherry fluorescence in the cytoplasm. Two-way ANOVA. Error bar, SD.
*p < 0.05; **p < 0.005; ***p < 0.0005; ns, not significant.

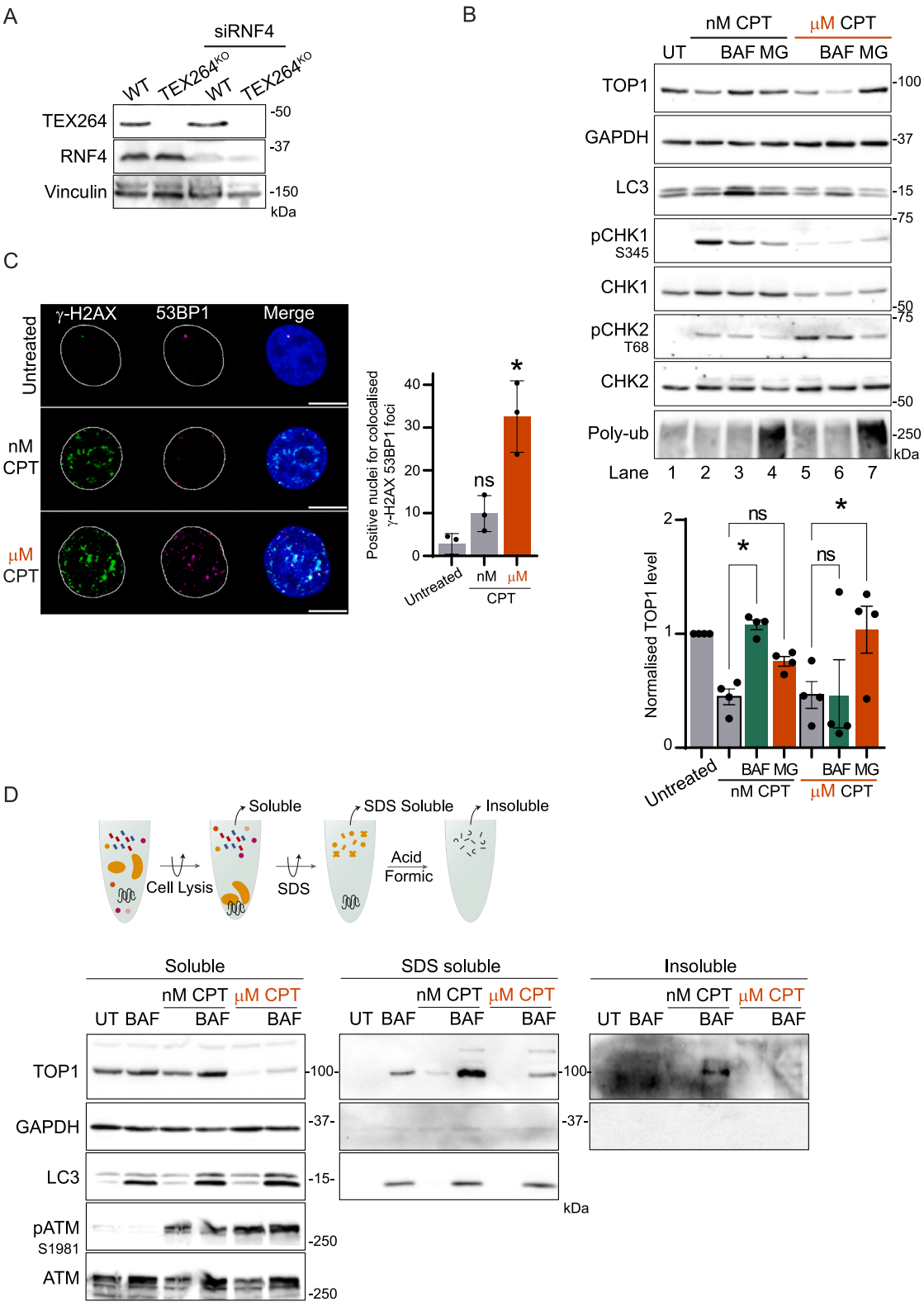

(legend on next page)

Figure S3. Autophagy promotes TOP1 degradation during replication stress to prevent protein aggregation, related to Figure 3

(A) Immunoblot showing TEX264 and RNF4 depletion in cells used for clonogenic assay.

(B) Immunoblot of TOP1 level in total cell extract ($n = 4$). Treatment with 50 nM CPT was performed for 24 h, and 2 μM MG132 (MG) or 50 nM BAF was added in the last 8 h. Treatment with 1 μM CPT was performed for 3 h with MG132 or BAF. Quantification of normalized TOP1 protein level. One-way ANOVA, SEM represented; UT, untreated.

(C) Immunofluorescence of γ-H2AX and 53BP1 foci after 1 h of 50 nM CPT or 1 μM CPT ($n = 3$). Scale bar, 10 μm. Quantification of positive nuclei for colocalized foci of both γ-H2AX and 53BP1. Two-way ANOVA. Error bar, SD.

(D) Method for isolation of aggregated protein by sequential lysis and denaturation step. The aggregates fraction is insoluble in lysis buffer and 1.5% SDS but solubilized in 100% formic acid to be loaded on the gel. Isolation of the aggregates performed after 12 h of treatment with 50 nM CPT or 1 μM CPT ($n = 3$); UT, untreated.

*$p < 0.05$; ns, not significant.

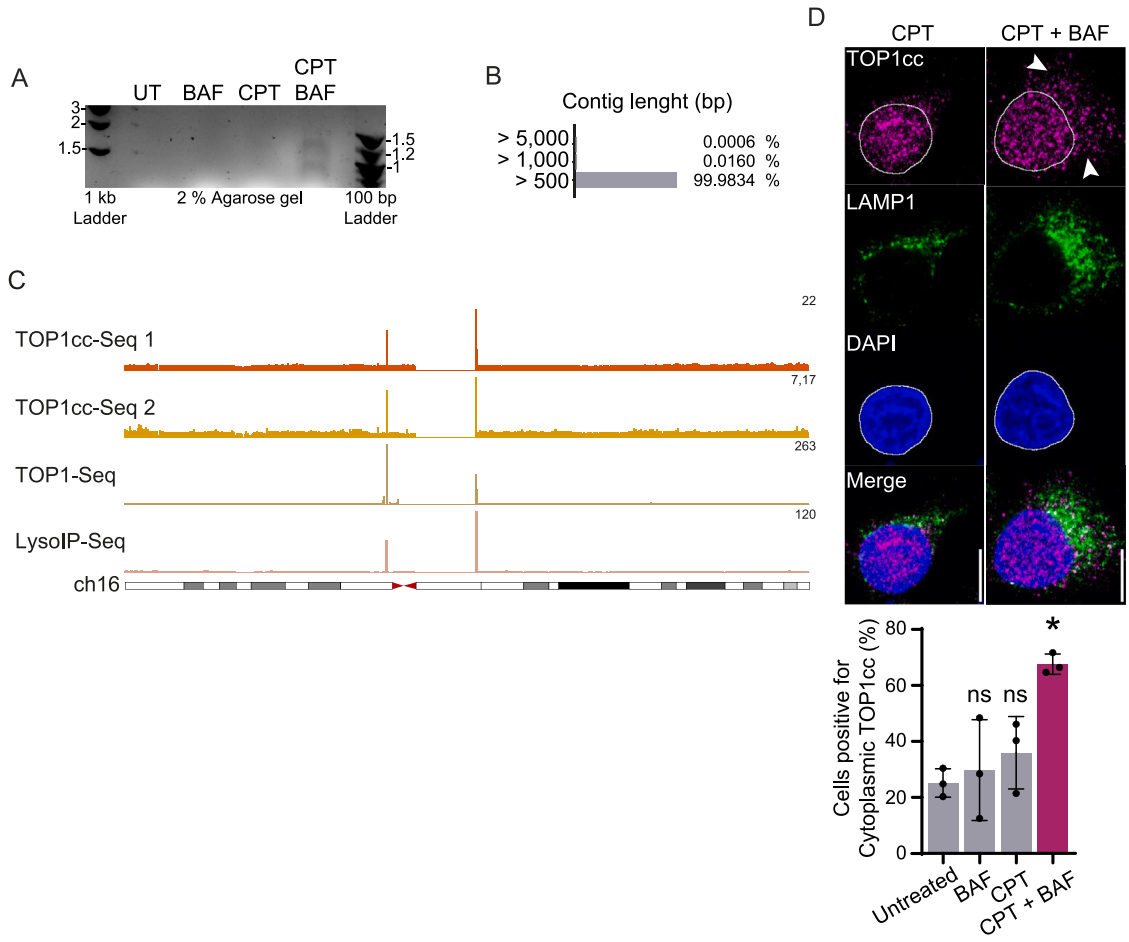

Figure S4. TOP1cc (TOP1 and its bound DNA fragment) are translocated in the cytoplasm and degraded by lysosomes, related to Figure 4

(A) DNA fragments purified by LysoIP after 6 h of treatment with 50 nM CPT and/or 50 nM BAF and run on a 2% agarose gel. UT, untreated.

(B) Contigs length distribution was obtained by NGS sequencing of the DNA fragments purified by LysoIP after 6 h of treatment with CPT and 50 nM BAF.

(C) Genomic browser images showing ChIP-seq of TOP1cc obtained in MCF7 (1) and LNCAP (2) (GEO: GSE135808),[87] ChIP-seq of catalytically engaged TOP1 obtained in HCT116 (GEO: GSE57628),[88] and LysoIP-seq signals obtained from sequencing lysosomal DNA after 50 nM CPT in HeLa. ChIP-seq and LysoIP profiles are presented at chromosome 16. All conditions were treated with CPT. Data aligned on genome hg38 and represented as sequence tags per million (TPM).

(D) Immunofluorescence of TOP1cc foci and LAMP1 after 4 h of treatment with 50 nM CPT, with or without 50 nM BAF. Quantification of cells positive for cytoplasmic TOP1cc foci ($n = 3$). Scale bar, 10 μm. Two-way ANOVA. Error bar, SD. *$p < 0.05$; ns, not significant.

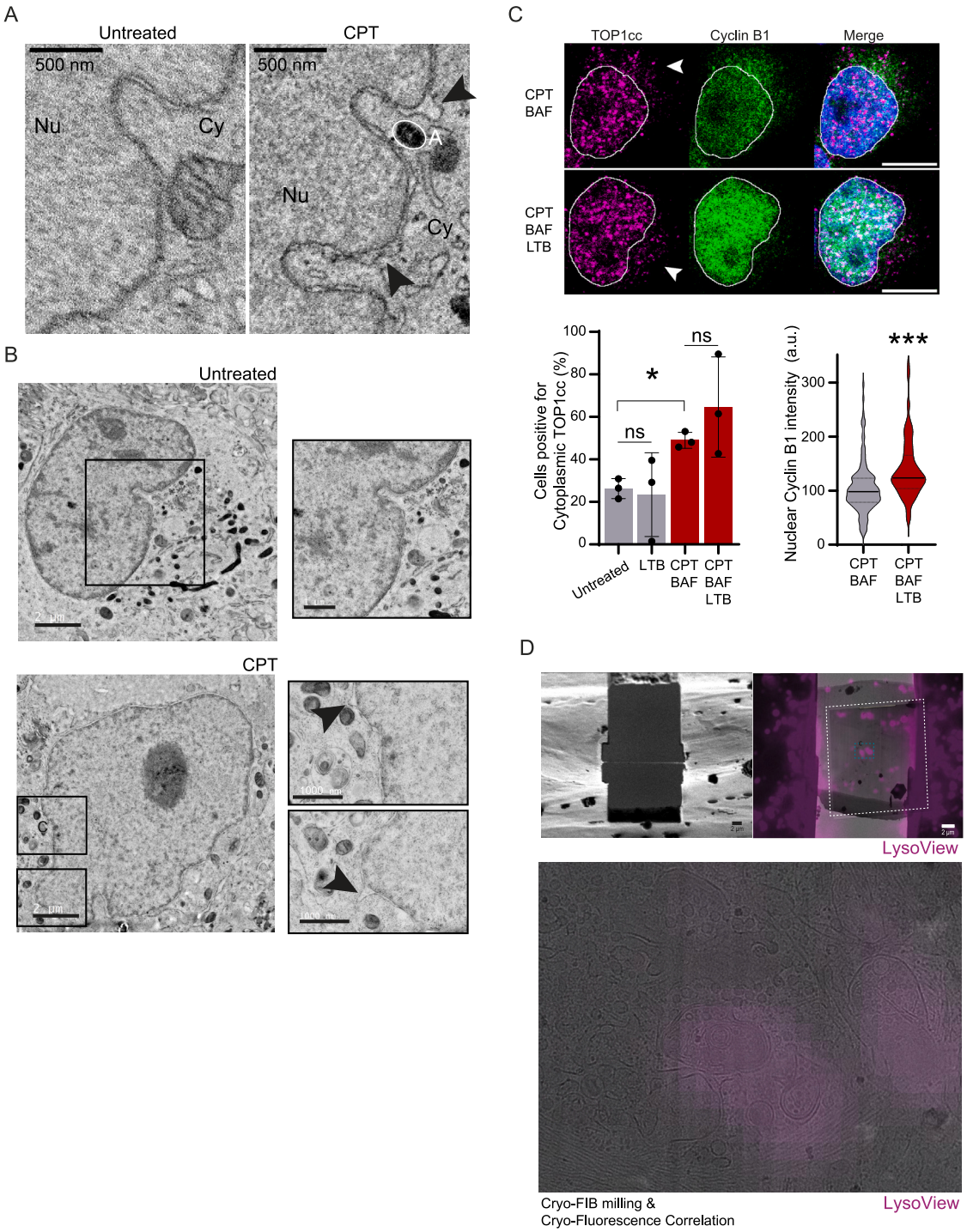

Figure S5. CPT induces nuclear envelope blistering and TOP1cc exit to the cytoplasm, related to Figure 5

(A) Representative electron microscopy images for a distinct set of cells. Treatment was conducted for 30 min with 50 nM CPT. Scale bar, 500 nm. Arrows pointing at blister structures. Nu, nucleoplasm; Cy, cytoplasm; A, autophagosome.

(B) Representative electron tomographic slices fixed by high-pressure freezing showing nuclear envelope blister in HeLa. Treatment was conducted for 30 min with 50 nM CPT. Scale bar, 2 μm (left); scale bar, 1 μm (zoom, right). Arrows pointing at blister structures.

(C) Immunofluorescence of TOP1cc foci and cyclin B1 after 3 h of treatment with 50 nM CPT ($n = 3$). Cyclin B1 is used as a control for the inhibition of exportin by leptomycin B (LTB). Scale bar, 10 μm. (Left) Quantification of positive cells for cytoplasmic TOP1cc foci. One-way ANOVA. (Right) Cyclin B1 intensity per nuclei (quantification for a representative experiment). t test. Error bar, SD. $^{*}p < 0.05$; $^{***}p < 0.0005$; ns, not significant.

(legend continued on next page)

(D) Cryo-focused ion beam (FIB) milling and cryo-fluorescence correlation images of cells after 30 min of 50 nM CPT treatment. Lysosomes are stained with LysoTracker. (Top) Ion beam image of a final lamellae after targeted milling and correlation between the SEM image of a lamellae, the transmission electron microscopy (TEM) medium magnification montage of the same lamellae acquired at 15,000× (white dashed lines) and the fluorescent molecularly imprinted polymer (MIP) acquired post milling. (Bottom) Close-up view on the TEM medium magnification correlated with LysoTracker fluorescence used for targeted acquisition of the tilt series. Scale bar, 2 μm.

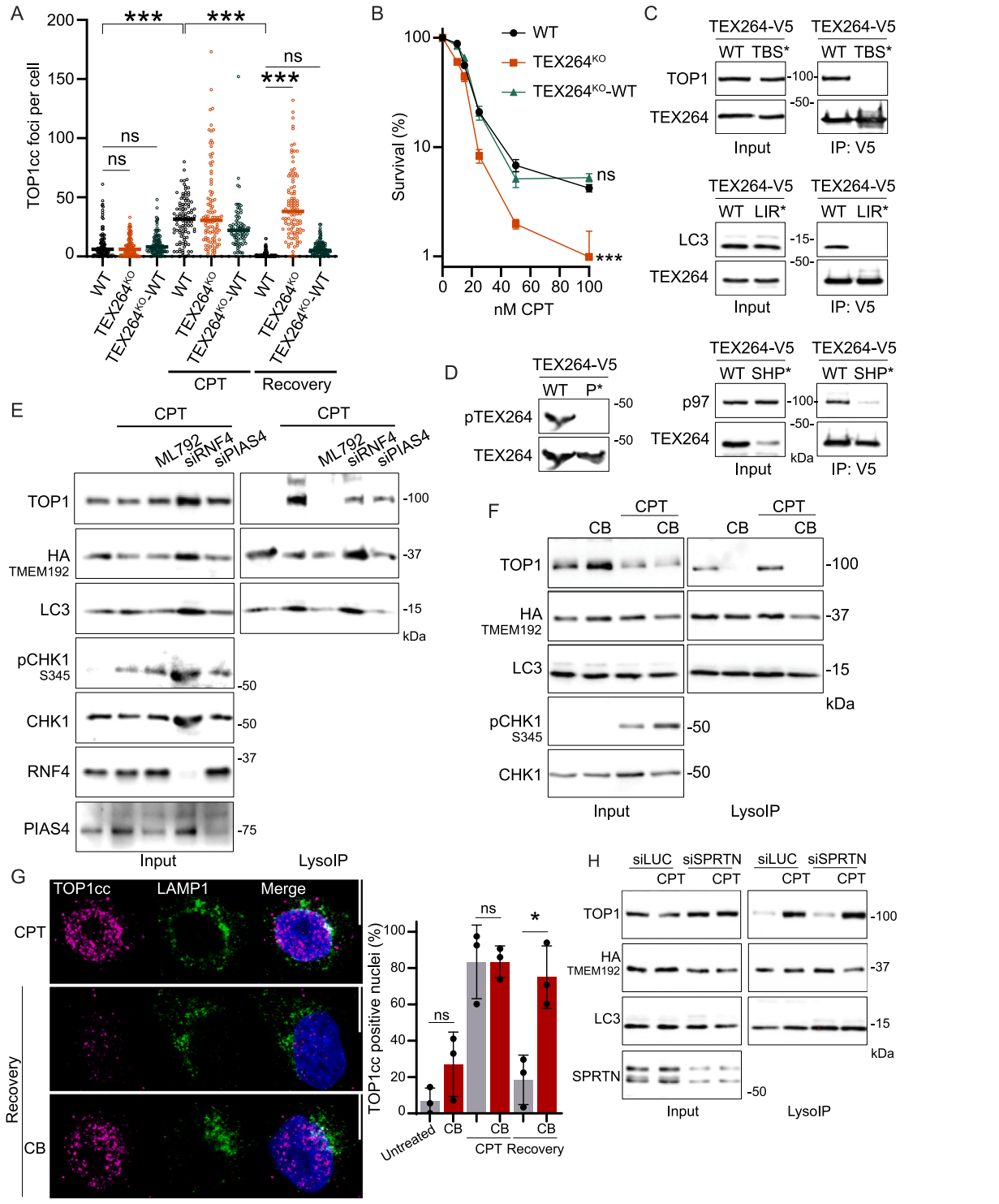

Figure S6. TEX264 with p97 and SUMO acts as the receptor for TOP1cc degradation by autophagy, related to Figure 6

(A) Immunofluorescence of TOP1cc foci in WT cells, TEX264^{KO}, or TEX264^{KO} complemented with TEX264^{WT} after 2 h of 50 nM CPT, followed by 2 h of recovery. Quantification TOP1cc foci per nuclei, one experiment shown (n = 3). Two-way ANOVA. Error bar, SD.

(B) Quantification of a representative clonogenic assay in WT, TEX264^{KO} or TEX264^{KO} complemented with TEX264^{WT} after 8 h of CPT treatment (n = 3). Error bar represents mean ± SEM. Two-way ANOVA.

(C) Co-immunoprecipitation of TEX264-V5 either WT or TBS*, LIR* or SHP* mutants to confirm the loss of interaction with respective TEX264-binding partners.

(legend continued on next page)

(D) Lysate of cells expressing TEX264 WT or P* mutant. The antibody used to detect phosphorylation specifically recognizes TEX264 phosphorylated on serines 271 and 272.
(E) LysoIP was performed after 5 h of treatment with 50 nM CPT and the inhibitor of SUMO E1 activating enzyme ML792. siRNA targeting RNF4 and PIAS4. All conditions were treated with 50 nM BAF ($n = 3$).
(F) LysoIP performed after 5 h of treatment with 50 nM CPT and 10 μM of p97 inhibitor CB-5083 (CB). All conditions were treated with 50 nM BAF ($n = 3$).
(G) Immunofluorescence of TOP1cc foci after 2 h of 50 nM CPT. Recovery was performed for 2 h in media or with the p97 inhibitor CB-5083 (CB). Scale bar, 10 μm. Quantification of positive nuclei for TOP1cc foci ($n = 3$). Two-way ANOVA. Error bar, SD.
(H) LysoIP performed after 3 h of treatment with 50 nM CPT, depletion of SPRTN achieved using siRNA against SPRTN; control siLUC ($n = 3$). All conditions were treated with 50 nM BAF.
*$p < 0.05$; ***$p < 0.0005$; ns, not significant.

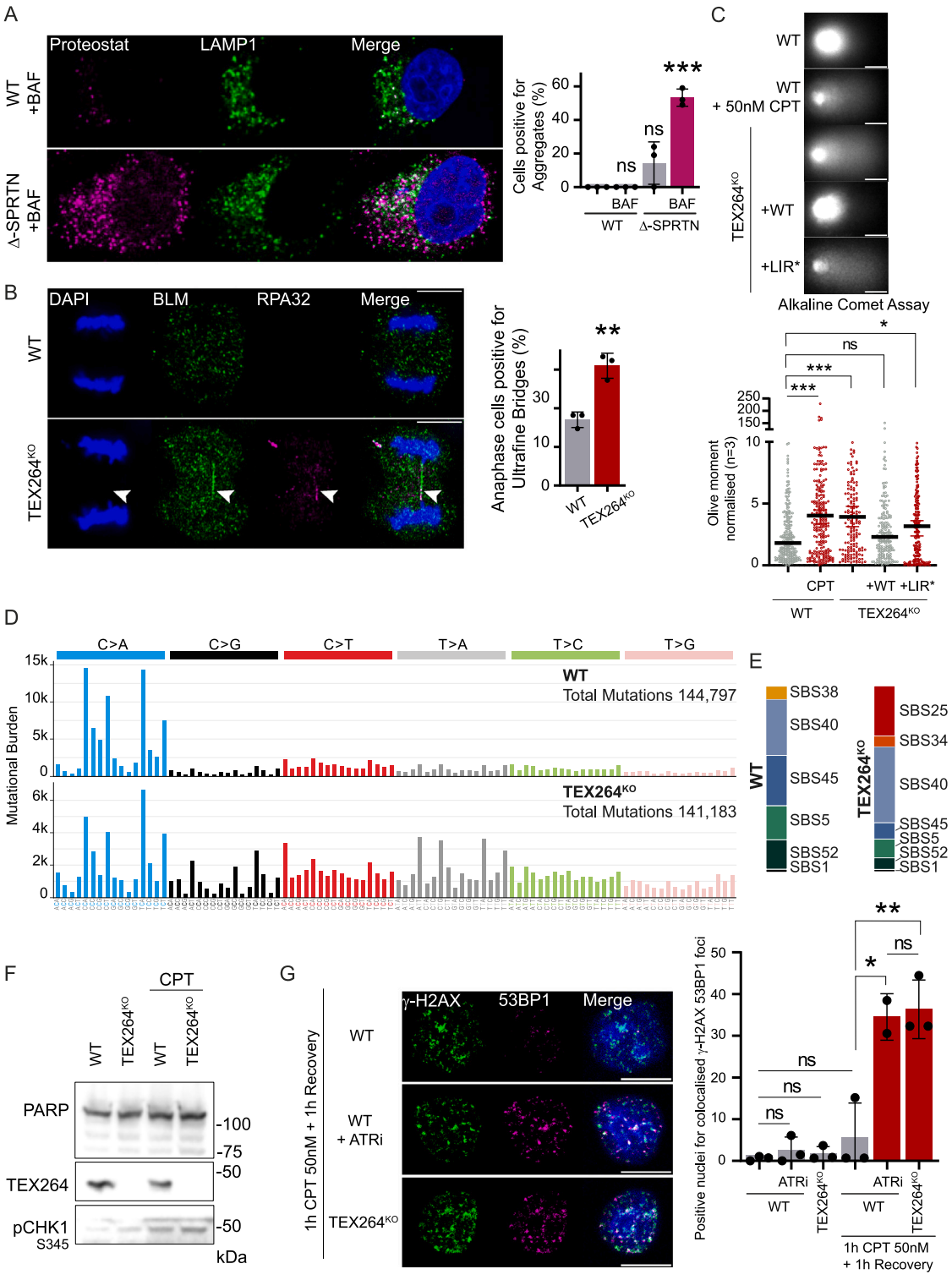

Figure S7. Autophagy of TOP1cc is independent of SPRTN, and TEX264 inactivation promotes genomic instability, related to Figure 7

(A) Immunofluorescence of protein aggregates using the Proteostat dye and the late endosome and lysosome marker LAMP1 after 16 h of treatment with 50 nM CPT in WT or Δ-SPRTN (partial knockout [KO]). Quantification of cells positive for aggregates (n = 3). Scale bar, 10 μm. Two-way ANOVA. Error bar, SD.

(B) Anaphase ultrafine bridge detection in cells treated for 2 h with 50 nM CPT and allowed to recover for 24 h (n = 3). Positive BLM and RPA32 anaphase bridges are labeled with arrows. Scale bar, 10 μm. Quantification of anaphase cell presenting ultrafine bridge. t test. Error bar, SD.

(legend continued on next page)

(C) Alkaline comet assay performed on untreated cells and compared with 50 nM CPT for 1 h treatment ($n = 3$). WT HeLa cells were compared with TEX264^{KO} cells or indicated TEX264 complementation in TEX264^{KO} background. The quantification of Olive moment normalized against WT untreated; the median is represented. Scale bar, 20 μm. One-way ANOVA.
(D) Mutational profiles of WT and TEX264^{KO} comparing untreated to treated cell population assessed by whole-genome sequencing. Treatment was performed with 10 nM CPT for 7 days continuously. Single base substitutions (SBSs) are represented as counts in each trinucleotide context.
(E) Proportion of SBS mutational signatures found in the mutational profiles of WT and TEX264^{KO} cells. SigProfilerAssignments used to assign mutations to the nearest SBS mutational signatures present in the COSMIC v.3.3 signature set.[145]
(F) Immunoblot showing the poly (ADP-ribose) polymerase (PARP) full length as a loading control and to monitor potential apoptotic effect in WT and TEX264^{KO} cells used for whole-genome sequencing after treatment with 10 nM CPT performed for 7 days continuously.
(G) Immunofluorescence of γ-H2AX and 53BP1 foci after 1 h of 50 nM CPT and 1 h recovery ($n = 4$). ATR inhibition was performed using 1 μM ATR inhibitor VE-822 (ATRi) during 1 h with 50 nM CPT and 1 h recovery. Scale bar, 10 μm. Quantification of nuclei positive for colocalized foci of both γ-H2AX and 53BP1. Two-way ANOVA. Error bar, SD.
*$p < 0.05$; **$p < 0.005$; ***$p < 0.0005$; ns, not significant.